# UNIVERSIDAD DE BUENOS AIRES

Facultad de Ciencias Exactas y Naturales

Departamento de Física


# Formación de Galaxias, Evolución Química y Vientos Galácticos


Cecilia Scannapieco

Directora de Tesis: Dra. Patricia B. Tissera

Lugar de Trabajo: Instituto de Astronomía y Física del Espacio


Trabajo de Tesis para optar por el título de
Doctor de la Universidad de Buenos Aires en el área de Ciencias Físicas

Junio de 2006

# Resumen

El estudio de la formación de galaxias constituye un tema de gran importancia y actualidad. Si bien los principales procesos físicos que determinan el ensamblaje de la estructura en gran escala están entendidos, diferentes aspectos relacionados a los mecanismos que actúan en escalas galácticas todavía se encuentran bajo estudio. En particular, se cree que las explosiones de Supernova (SN) juegan un rol fundamental en la evolución de las galaxias, eyectando de metales y energía al medio interestelar. Estos procesos afectan importantes propiedades galácticas como la morfología, la dinámica, la actividad de formación estelar, el enriquecimiento químico. Las supernovas, a través del calentamiento y disrupción de nubes de gas frías, generarían un mecanismo auto-regulado para la formación estelar. Más aún, se cree que serían capaces de producir violentos vientos galácticos como los observados en galaxias con fuerte actividad de formación estelar, así como de enriquecer químicamente el medio intergaláctico. En este trabajo se presenta un nuevo modelo para describir la eyección de metales y energía por supernovas de tipo II y tipo Ia, en el contexto de simulaciones cosmológicas hidrodinámicas basadas en la técnica *Smoothed Particle Hydrodynamics*. A su vez, se ha desarrollado un modelo para describir a la componente gaseosa como un medio multifase, permitiendo un modelado más realista del medio interestelar. Este nuevo desarrollo numérico permite modelar consistemente la eyección de energía y elementos químicos al medio interestelar, sin introducir parámetros dependientes de la resolución o de la masa de las galaxias. Este modelo es capaz de generar un mecanismo de formación estelar auto-regulado y de producir importantes vientos galácticos. Dichos vientos pueden transportar eficientemente material fuera de los halos galácticos, enriqueciendo químicamente al medio intergaláctico. El éxito de nuestro modelo se concreta al poder describir, dentro de un marco cosmológico, la formación de sistemas discoidales con propiedades dinámicas y químicas comparables a resultados obervacionales de galaxias espirales.

Palabras clave: galaxias: formación - evolución - abundancias - cosmología: teoría - métodos: numéricos

# Galaxy Formation, Chemical Evolution and Galactic Winds

Abstract. The study of galaxy formation is nowadays a subject of primary importance in astrophysics. Although the main mechanisms involved in the assembly of the structure are understood, several processes acting at galactic scale are still under study. In particular, Supernova (SN) explosions are thought to play a fundamental role in the evolution of galaxies, ejecting heavy elements and energy into the interstellar medium. These mechanisms significantly affect important galaxy properties such as morphology, dynamics, star formation activity, chemical enrichment. SN explosions, through the heating and disruption of cold gas clouds, are believed to set a self-regulated star formation cycle in galaxies. Moreover, they are thought to be responsible of the galactic winds observed in starbursting galaxies, as well as of the chemical contamination of the intergalactic medium. In this work we present a new model to describe chemical and energy feedback by SNe within hydrodynamical numerical simulations of cosmological structure formation based on the Smoothed Particle Hydrodynamics technique. This new numerical development consistently models the ejection of energy and chemical elements into the interstellar medium, without introducing scale or resolution dependent parameters. We also present a new scheme to describe a multiphase gas medium, developed to more realistically model the nature of the interstellar medium. Our model succeeds in setting a self-regultated cycle for star formation, and in producing important galactic winds. These winds can effectively transport material out of the haloes, enriching with metals the intergalactic medium. The success of our model is accomplished by being able to describe, in the context of a cosmological model, the formation of spiral galaxies with dynamical and chemical properties with observational counterparts.

Key words: galaxies: formation - evolution - abundances - cosmology: theory - methods: numerical

# Contents

# Agradecimientos

Mucha gente me acompañó en estos cuatro años de distinta manera y en distintos momentos. A todos ellos estoy agradecida por haberme enseñado una infinidad de cosas en aspectos tanto científicos como humanos. Aunque seguramente ahora no pueda recordar a todos, me gustaría destacar a algunas de ellos.

Patricia, gracias por las innumerables cosas que me enseñaste, por la estimulación constante, por tu dedicación y paciencia en mi formación, y por haberme ayudado y acompañado en mi búsqueda de nuevas oportunidades y desafíos.

I would like to thank Simon White for giving me the opportunity to work with him and to learn every day from our discussions. A special thank to Volker Springel, for his dedication and patience in my first steps with the code. Also, Simon and Volker, thanks for the nice atmosphere of work in my stays at MPA.

A mis viejos, por ser los primeros y más especiales compañeros de mi vida, por toda la ayuda, la contención, el apoyo infinitos en cada momento. Gracias por haberme enseñado a vivir siempre en un equilibrio entre el esfuerzo y el trabajo, y la locura y diversión de cada día.

A mis hermanas, Minu, Ale y Ener, por compartir conmigo tantas cosas, por ser mis compañeras de viaje, por cuidarme, protegerme y enseñarme a compartir las cosas de la vida. Gracias por hacer de cada momento algo inolvidable y divertido. A Juanchi, Pablino y Lisi por participar de todo esto y seguirnos en nuestras locuras.

A Jose y a Sebas, por estar siempre cerca mío, escuchando, aconsejando, compartiendo...

Al Chino, por estar siempre rondando por ahí, por los consejos y puntos de vista.

A todos aquellos que me acompañaron y ayudaron durante estos años: a Sil, a Leo, a Sergio, a Matías. A los que compartieron (y aguantaron) mi locura del último tiempo en el IAFE: Mari, Abi y Tomás. A mis amigas de siempre, Vero, Vani, Lau, Pauli, Borre, Emi. A Alberto, gracias.

A Sofía, por haberme ayudado y acompañado en mis primeras estadías en Alemania. To the people from MPA, for helping me to enojoy my stay there.

To my friends in Germany: Marco, Pao and Rasmus, thanks for your company and support, specially at the end of 2004. To Almu, Jens, Aybüke, Jorge, Patricia, Marcelo, Nico, Dani, Carlos. Thanks for making me feel a bit at home in Munich.

Quisiera también agradecer a toda la gente del IAFE, en especial a Francisco por su ayuda durante el último tiempo.

And to the people of MPA who helped me during the last years. Specially, to Cornelia, Maria and Gabi.

# Chapter 1

# Introduction

A primary goal in modern cosmology is to understand how galaxies form. Currently, the most popular scenario for structure formation in the universe is known as the *Hierarchical Clustering Model*. According to this scenario, cosmic structures arise from small Gaussian fluctuations in the density field generated in the early universe. As gravity amplifies these small initial perturbations, they collapse and separate from the general expansion, giving rise to the first individual, bounded structures. In this context, small clumps are formed first, and progressively larger clumps are generated by merger and accretion of smaller substructures, in a hierarchical way (Peebles 1969). Structure formation is, thus, a quite violent process in which interactions and mergers are ubiquitous, affecting significantly the properties of galaxies along their formation process.

According to the current cosmological *concordance* model, only $\sim 30\%$ of the universe is formed by matter. In particular, $\sim 90\%$ of this matter is constituted by *dark matter*. Dark matter is not observable by emission or absorption, but only by its gravitational effects; it is thought to be mostly constituted by exotic particles whose nature is not yet understood. Several models have been proposed to explain the properties of the dark matter component. In particular, the *Cold Dark Matter* (CDM) model assumes that dark matter is formed by particles of low thermal velocity. The CDM model is, nowadays, the one that better matches a variety of available observations, being consistent with a hierarchical process for structure formation. The rest of the matter content is constituted by *baryons* which comprise the observable objects. Baryons are dissipative by nature, undergoing processes such as photoionization, cooling, star formation and chemical enrichment.

As a result of the dominant role of dark matter in the mass content of the universe, it is dark matter which determines the general gravitational collapse of the structure, the rate of mergers and interactions, the masses and location of the primeval fluctuations, seeds of future galaxies. In a hierarchical scenario, as the

universe evolves, the dark matter aggregates into larger and larger clumps, the gas cools down and condenses within these dark matter haloes, eventually triggering star formation. These mechanisms would give rise to the complex structure of galaxies and clusters of galaxies that we observe today (White 1996).

Along the assembly of the structure in the universe, gravity and dissipative mechanisms act together in a complex interplay, each of them introducing its own typical scales which can be very different from the ones of a galaxy as a whole. Moreover, in hierarchical clustering models, mergers and interactions affect the evolution of galaxies in a non trivial manner, making the detailed study of the formation and evolution of galaxies an extremely complex task. Theory, observations and simulations are devoted to disentangle the effects of the different physical processes involved in the formation of the structure, and their relative impact on galaxy properties. In particular, numerical simulations in which gravity solvers are coupled to hydrodynamical schemes for the gas have become a powerful tool to study galaxy formation on physical basis in the context of a cosmological model. However, several challenges have been posed mainly by the need to describe, at the same time, the large-scale dynamical mechanisms required for the study of galaxy formation and the small-scale processes related with the formation and evolution of stars.

Currently, hydrodynamical cosmological simulations including radiative cooling and star formation, at best, coarsely reproduce the observed properties of galaxies, but they fail when scrutinised in detail. Among the most prominent problems are the 'catastrophic angular momentum loss' (e.g. Navarro & Benz 1991; Navarro & White 1994), and the difficulty in finding a consistent modelling of supernova feedback (e.g. Navarro & White 1993; Metzler & Evrard 1994; Yepes et al. 1997; Marri & White 2003; Springel & Hernquist 2003). The first issue mainly affects galaxy morphology, size and kinematics, while the latter primarily influences the efficiency of star formation. Both are the subject of intense research. Reproducing the chemical properties of observed galaxies in detail may be viewed as an intertwined third problem.

Supernova (SN) explosions are thought to play a fundamental role in the evolution of galaxies since they are considered the most efficient and ubiquitous mechanism for the ejection of metals and energy into the interstellar medium (ISM). These *chemical and energy feedback* processes affect the formation of galaxies by influencing the cooling rates, the star formation efficiency, and the gas dynamics. On one side, the presence of metals in the ISM driven by SN chemical feedback affects the gas cooling times since the radiative cooling rates depend sensitively on metallicity (Sutherland & Dopita 1993). On the other hand, the release of energy by SNe is a key process for regulating star formation through the heating and disruption of cold gas clouds, and for producing outflows which can transport enriched material into the intergalactic medium (e.g. Lehnert & Heckman 1996; Dahlem, Weaver & Heckman 1998; Rupke, Veilleux & Sanders 2002; Shapley et al. 2001; Frye, Broad-

hurst & Benítez 2002; Martin 2004). As suggested by observations and theory, the largest outflows should be able to develop in small systems because of their shallower potential wells (e.g. Larson 1974; White & Rees 1978; Dekel & Silk 1986; White & Frenk 1991). Since in hierarchical galaxy formation scenarios large systems are formed by the aggregation of smaller ones, energy feedback from SNe is expected to have important effects for nearly all systems in different stages of galaxy formation.

The modelling of SN chemical feedback within numerical simulations has demonstrated to be an important tool for studying the effects of metals on the ISM and the metallicity properties of galaxies. Since the presence of metals accelerates the gas cooling process and can thus influence the collapse of baryons within the dark matter haloes, it is clearly important to develop cooling treatments which consistently consider the gas metallicity. In particular, several models of chemical enrichment have been developed so far, mainly with the aim at reproducing the chemical properties of certain types of galaxies, or of galaxy clusters (e.g. Larson 1976; Tinsley & Larson 1979; Burkert & Hensler 1988; White & Frenk 1991; Burkert, Truran & Hensler 1992; Ferrini et al. 1992; Theis, Burkert & Hensler 1992; Steinmetz & Müller 1994; Kauffmann 1996; Chiappini, Matteucci & Gratton 1997; Kauffmann & Charlot 1998; Boisser & Prantzos 2000). However, more recent simulations have demonstrated the importance of following the full cosmological growing up of galaxies in which mergers and interactions can significantly affect the star formation rates and the chemical mixing process, leading to different chemical patterns (e.g., Mosconi et al. 2001; Kawata & Gibson 2003; Tornatore et al. 2004).

On the other hand, the modelling of SN energy feedback within simulations has shown to be a complex task. For this reason, only recently have numerical models started to develop energy feedback implementations which appear capable of reproducing the large-scale and energetic processes observed in real strongly star-forming galaxies (e.g. Marri & White 2003). An important complication arises because the physical mechanisms for the injection of energy into the ISM act at sub-resolution scales and, consequently, models need to implement strategies to allow the mimic of their effects on the numerical resolved scales. Several works have tried to consistently implement SN energy feedback in numerical simulations (e.g. Katz & Gunn 1991; Cen & Ostriker 1992,1999; Navarro & White 1993; Metzler & Evrard 1994; Yepes et al. 1997; Kay et al. 2002; Lia, Portinari & Carraro 2002; Semelin & Combes 2002; Marri & White 2003; Springel & Hernquist 2003). Although each of these approaches has partially succeeded, none of them has converged in a fully satisfactory scheme yet.

In addition, an important complication which arises in numerical simulations based on the popular Smoothed Particle Hydrodynamics technique (SPH; Gingold & Monaghan 1977; Lucy 1977) is that multiphase, multiscale mixtures like the interstellar medium in star-forming galaxies is not properly represented. In the SPH formalism, the density associated with a given particle is estimated by averaging

over all neighbours within an adaptively defined smoothing region. As a result, diffuse particles which lie near dense and cold clouds overestimate their densities by including dense particles within the smoothing region. This translates into enhancement of the cooling rate, excessive accretion of gas into the cold phase, and too high efficiency of star formation (Thacker et al. 2000; Pearce et al. 2001). This behaviour makes even more difficult the modelling of SN energy feedback in which, ideally, the heating up and expansion of cold gas near star forming sites would give rise to a diffuse component in coexistence with high density gas. Because of the problem mentioned above, in standard SPH implementations such a diffuse phase would not survive as a result of numerical artifacts. During the last years, several *ad hoc multiphase gas* models of differing complexity have been suggested for this problem (e.g. Pearce et al. 1999, 2001; Thacker & Couchman 2001; Springel & Hernquist 2003; Marri & White 2003), which have helped to diminish the impact of numerical artifacts in simulations.

One of the main consequences of the poor capability of properly describing the nature of the ISM and the SN energy feedback process in galaxy formation simulations is translated in the difficulty in reproducing disk systems with properties similar to those of observed spiral galaxies. The formation and evolution of spiral galaxies is an extremely difficult problem which is yet under intense research. Spiral galaxies are complex entities easily recognized observationally by the presence of important disk-like structures supported by rotation. They also might host other dynamically different components such as bulges and stellar haloes. Some spirals can also develop instabilities which lead to the formation of bars in their centres. In order to understand in detail the formation of spiral galaxies, it is then necessary to explain the origin of these components consistently. Observationally, several important results have allowed to trace their main physical properties such as kinematics, metallicities and stellar ages. These results (mostly restricted to our own galaxy) have demonstrated the complicated nature of spiral galaxies, and explaining their formation has become an ever growing topic in current cosmology.

In particular, observations in the Milky Way have revealed that our galaxy has four distinct components which are thought to have been formed at different stages of the evolutionary process. These are the *thin disk*, the *thick disk*, the *bulge* and the *stellar halo* (Freeman & Bland-Hawthorn 2002 and references therein), and they have been found to have different dynamical, chemical and structural properties. The *stellar halo* is the oldest structure (probably older than 12 Gyr), it is spheroidal in shape, its mass is only 1% of the total stellar mass, and it extends approximately in the radial range $8-25$ kpc (e.g. Morrison 1993; Chiba & Beers 2000). The angular momentum content of this component is found to be close to zero (e.g. Freeman 1987) and stars are dominated by velocity dispersion. Its mean metallicity is low, with a mean in [Fe/H]$\sim -1.5$ dex (Chiba & Beers 2000). One possible explanation for the origin of the galactic stellar halo is the accretion of small satellite galaxies

(Searle & Zinn 1978). The *bulge* is the innermost structure of 2 kpc height and has a spheroidal shape. It is formed by stars which are mostly old ($\sim$ 10 Gyr), and its metallicity distribution has a peak at [Fe/H]$\sim -0.3$ dex with a long lower metallicity tail up to $\sim -1$ dex (Mc William & Rich 1994). The bulge contributes to a 20% of the total surface luminosity of the galaxy. The *thin disk* has an exponential surface density profile with a scalelength of $2-2.5$ kpc. It is supported by rotation, with very low velocity dispersions. Its specific angular momentum is found to be close to that of the dark matter halo, which is consistent with the main hypothesis of the disk formation theory. The characteristic vertical scale is $\sim 0.8$ kpc. This component has a relatively high metallicity, which peaks at [Fe/H]$\sim -0.2$. Different authours have found that the oldest stars have ages $\sim 10-12$ Gyr but the bulk of stars in the thin disk is younger ($< t >\sim 7$ Gyr). It is thought that the thin disk component has its origin in a period of quiescent dissipation of baryons. Finally, the Milky Way galaxy has a significant *thick disk* (Gilmore & Reid 1983), which is fainter than the thin disk, with radial scalelength of 3 kpc and a vertical length of 2 kpc. The mean age of the thick disk is not known, although it seems to be old, with a mean stellar age of 12.5 Gyr (Liu & Chaboyer 2000). Although the rotation is not as tight as in the thin disk, the thick disk is mainly supported by rotation. Stars are more metal-poor than thin disk stars, with [Fe/H] from $\sim -2.2$ to $-0.5$ dex (Chiba & Beers 2000). The galactic thick disk is believed to arise from heating of the early stellar disk by minor mergers or accretion of smaller satellites.

These chemical properties can be used as fossil records of the state of galaxies at different epochs and, together with the dynamical properties, may give us clues to understand the formation and evolution of the Milky Way, and of spiral galaxies, in general. In the last years, sophisticated numerical codes have been developed with the aim at describing the formation of the different components of spiral galaxies in a consistent way. Among the main problems found in these studies, the angular momentum content of the different mass components seems to play a crucial role (e.g. Fall & Efstathiou 1980; Mo, Mao & White 1998). As it has been discussed by several authors (e.g. Navarro & Steinmetz 1997), the baryonic components in numerical simulations tend to transfer most of their angular momentum to the dark matter halos during close encounters, producing disks that are too small and too dense in comparison to their observed counterparts (e.g. Fall & Efstathiou 1980; Mo, Mao & White 1998). This is known as the 'catastrophic angular momentum loss' problem. Some recent numerical studies have shown that Supernova explosions, in which a large amount of energy is dumped into the interstellar medium, together with a more realistic representation of the multiphase character of the ISM would help to remedy this problem (e.g. Marri & White 2003).

In this work, we present a new model for describing energy and chemical feedback by SNe in numerical simulations, which allows us to revisit galaxy formation on more physical basis. The model accounts for the chemical enrichment and energy

release driven by Type Ia and Type II SN explosions, self-consistently implemented within a model for a multiphase interstellar medium. This multiphase scheme for the gas component allows a more realistic description of the nature of the interstellar medium. Metal-dependent cooling is also modelled. The main goal of this work is to develop a model with no scale-dependent, ad-hoc parameters. We have implemented our schemes within the cosmological code GADGET-2 (Springel & Hernquist 2002; Springel 2005), which we describe briefly in Appendix A. The implementation of our model has been divided into two stages. First, we implemented chemical enrichment and metal-dependent cooling. This is explained in Chapter 2, where we also analyse the performance of the model and the effects of chemical feedback on simulations of isolated galaxies. Chapter 3 uses more realistic initial conditions in order to show the current main problems of simulations which intend to describe the formation of spiral galaxies. In Chapter 4 we present the second main stage of our work, the implementation of multiphase gas and SN energy feedback, and make first tests of the numerical techniques. In Chapter 5 we show the ability of the model to self-regulate the star formation process and to trigger mass-loaded winds of enriched material, which constitutes the main success of this work. As a last application, in Chapter 6 we analyse the formation of a spiral-like galaxy in a cosmological context by using our code with SN energy and chemical feedback, and compare the results with observations of the Milky Way Galaxy. Finally, in Chapter 7 we present our conclusions.

# Chapter 2

# Chemical enrichment

Over the last decades, our knowledge of the chemical properties of the Universe and, in particular, of galaxies, has improved dramatically. Observations of the Local Universe (e.g. Garnett & Shields 1987; Skillman, Kennicutt & Hodge 1989; Brodie & Huchra 1991; Zaritsky, Kennicutt & Huchra 1994; Mushotzky et al. 1996; Ettori et al. 2002; Tremonti et al. 2004; Lamareille et al. 2004) as well as at intermediate and high redshifts (e.g. Prochaska & Wolfe 2002; Adelberger et al. 2003; Kobulnicky et al. 2003; Lilly et al. 2003; Shapley et al. 2004) have resulted in a quite detailed picture of the chemical history of the stellar populations and of the interstellar and intergalactic media. It is an important challenge for theories of galaxy formation to explain these observational results in the context of the current cosmological paradigm. Hydrodynamical numerical simulations are an important tool to make specific predictions on galaxy formation theories and to confront them with observations, because they can track the growth of structure in the dark matter and baryonic components. It is hence natural to ask what such simulations predict for the chemical properties of the universe.

Modelling of chemical feedback has been already addressed in numerous studies, mostly with the aim to reproduce the chemical properties of certain types of galaxies or of clusters of galaxies (e.g. Larson 1976; Tinsley & Larson 1979; Burkert & Hensler 1988; White & Frenk 1991; Burkert, Truran & Hensler 1992; Ferrini et al. 1992; Theis, Burkert & Hensler 1992; Steinmetz & Müller 1994; Kauffmann 1996; Chiappini, Matteucci & Gratton 1997; Kauffmann & Charlot 1998; Boisser & Prantzos 2000). However, more recent simulations have demonstrated the importance of following the full cosmological growing up of galaxies in which mergers and interactions can significantly affect the star formation rates and the chemical mixing process, leading to different chemical patterns (e.g., Mosconi et al. 2001; Kawata & Gibson 2003; Tornatore et al. 2004).

One of the motivations to evaluate the relevance of metal enrichment for galaxy formation is based on the fact that the cooling rate of baryons depends sensitively on metallicity (Sutherland & Dopita 1993). Radiative cooling in turn allows the

condensation of gas into dense and cold clouds, which form the reservoir of material available for the formation of stars. As chemical enrichment is a result of star formation, a chemical feedback cycle emerges, in which metals can in principle significantly accelerate the transformation of baryons into stars by increasing the cooling rate and the clumping of cold gaseous knots. In hierarchical scenarios these processes depend significantly on the chemical prescription adopted (Kaellander & Hultman 1998; Kay et al. 2000). These affect galaxy properties such as the luminosity function (White & Frenk 1991). For these reasons, a detailed analysis of the effects of metal-dependent cooling is clearly important for galaxy formation studies.

In this Chapter, we present a new model for describing chemical feedback in numerical simulations, which includes a treatment of the chemical enrichment by SNII and SNIa explosions, and it is coupled to a metal-consistent treatment of radiative cooling. While a treatment of chemical enrichment without energy feedback is an incomplete picture, the complexity of the problem merits a step-wise discussion of our model such that the primary physical effects can be better understood.

This Chapter is organised as follows. In Section 2.1, we describe the numerical implementation of star formation, chemical enrichment and metal-dependent cooling. In Section 2.2, we use idealized initial conditions of the formation of a disk-like galaxy in order to investigate the dependence of the results on numerical resolution and input parameters of the code, We also and assess the impact of metals on galactic properties.

## 2.1 NUMERICAL IMPLEMENTATION

Our model for the production and ejection of chemical elements by Supernova is based in part on the approach in Mosconi et al. (2001). We have implemented our scheme in the TreePM/SPH code GADGET-2, an improved version of the public code GADGET (Springel, Yoshida & White 2001) which manifestly conserves energy and entropy where appropriate (Springel & Hernquist 2002). In Appendix A, we give a summary of the main characteristics of GADGET-2 and we refer the interested reader to Springel & Hernquist (2002) and Springel (2005) for further information. For our work, we do not use the multi-phase treatment and the feedback model developed by Springel & Hernquist (2003), but we do include their treatment of UV background[1] in cosmological simulations (see Section 2.1.3). Also, we use a different parameterization for star formation, as described in detail below.

[1]The Ultraviolet (UV) flux comes from QSOs (quasi-stellar objects) and/or hot, massive stars in metal-producing young galaxies. It is believed that the UV background is responsible for maintaining the intergalactic diffuse gas and the Ly$\alpha$ forest in a highly ionized state. Observations indicate that the hydrogen component of the UV background must have been highly ionized by redshift $z \sim 5$, and it is near this redshift that the UV background is relevant (see Haardt & Madau 1996 for details).

### 2.1.1 STAR FORMATION

The treatment of star formation is a fundamental and critic aspect in simulations of galaxy formation. Currently, the physical mechanisms involved in the star formation process are not yet understood in detail (Kennicutt 1998). However, the general physical conditions that a gas cloud should satisfy in order to be able to form stars can be introduced in simulations through an algorithm which takes into account these physical constrains. One of the main processes involved in the formation of stars is related to the Jeans instability. The Jeans instability occurs when the pressure support of a gas cloud can not prevent its gravitational-driven collapse. In particular, gas clouds which are cold and dense enough can suffer from the Jeans instability, provided the gas stays cold during the collapse. These physical properties are introduced in the simulations by making gas particles to fulfill certain conditions for forming star particles. In our model, we assume that gas particles are eligible for star formation if they are denser than a critical value ($\rho > \rho_* = 7.0 \times 10^{-26}$g cm$^{-3}$, where $\rho$ denotes gas density) and if they lie in a convergent flow ($\nabla \mathbf{v} < 0$). In practice, the first condition is sufficient to assess that the gas particle will stay cold during collapse. The second condition is introduced in order to constrain star formation to collapsing gas clouds.

Observationally, it is found that the star formation rate per unit volume is remarkably tightly correlated with the total gas surface density (Kennicutt 1998). Motivated by this result, in our simulations we introduce this relation as an input to model the star formation rate. In particular, for gas particles eligible for star formation, we assume a star formation rate per unit volume equal to

$$\dot{\rho}_\star = c \frac{\rho}{\tau_{\rm dyn}}, \tag{2.1}$$

where $c$ is a star formation efficiency (we usually adopt $c = 0.1$), and base the creation of new stellar particles on the stochastic approach of Springel & Hernquist (2003, see also Lia et al. 2002). To this end, each gas particle eligible for star formation in a given time-step is assigned a probability $p_*$ of forming a star particle given by

$$p_* = \frac{m}{m_*}\Big[1 - \exp(-\frac{c\,\Delta t}{\tau_{\rm dyn}})\Big], \tag{2.2}$$

where $\Delta t$ is the integration time-step of the code, $m$ is the mass of the gas particle, and $m_*$ is defined as $m_* = m_0/N_g$ with $m_0$ being the original mass of gas particles at the beginning of the simulation and $N_g$ a parameter which determines the number of 'generations' of stars formed from a given gas particle (we assume $N_g = 2$). If a random number drawn from a uniform distribution in the unit interval is smaller than $p_*$, we form a new stellar particle of mass $m_*$ and reduce the mass of the gas particle accordingly. Once the gas particle mass has become smaller than $m_0/N_g$,

we instead turn it into a star particle. Newly born stars are assumed to have the same chemical abundances as the gas mass from which they form.

The main advantage of this stochastic approach is that all particles are either purely stellar or purely gaseous, conversely to Mosconi et al. (2001), which prevent us from the use of 'hybrid' particles, with both gaseous and stellar components. The latter would artificially force the stellar component to evolve dissipately like the gas. Note that, as a consequence of the star formation scheme, the number of baryonic particles in the simulation does not remain constant. Unlike Springel & Hernquist (2003), we also exchange the masses of heavy elements explicitly between gas and star particles (see next Section). As a result, the mass spectrum of stellar and gas particles is slightly washed out around otherwise sharp discrete values.

### 2.1.2 CHEMICAL PRODUCTION AND DISTRIBUTION

Chemical elements are synthesized in stellar interiors and ejected into the ISM by supernova explosions. Depending on the mass of the progenitor star, different chemical elements and in different relative fractions are produced by stellar evolution and spread over the surrounding interstellar medium at the end of the life of the stars. In order to model the production and distribution of metals in the context of the simulations, there are three basic ingredients we have to consider: the *supernova rate* (i.e. the number of exploding stars per time unit), the *chemical yields* of each element (i.e. chemical material ejected in explosions), and the *typical life-times* of progenitor stars, which determine the characteristic time of the metal release.

In our model, we include a separate treatment of Type II (SNII) and Type Ia (SNIa) SNe. These two types of SNe originate from different stellar populations, and have different rates, yields and typical time-scales. We use different yields for SNII and SNIa which, in the case of SNII, are metal-dependent. Hence, we will treat SNeII and SNeIa separately, owing to the need to model their different characteristics. For example, SNII produce most of the chemical elements, except for iron, which is mainly produced by SNIa. Another difference between these two types of SN is that SNeII are the endpoint of the evolution of massive stars with short life-times, in contrast to SNeIa, which result from the evolution of binary systems with life-times of $\sim 1$ Gyr.

We assume that initially gas particles have primordial abundances (i.e. the ones resulting from Big-Bang nucleosynthesis): $X_H = 0.76$ and $Y_{He} = 0.24$, and we consider the enrichment by the following elements, assuming production only by SNII and SNIa: H, $^4$He, $^{12}$C, $^{16}$O, $^{24}$Mg, $^{28}$Si, $^{56}$Fe, $^{14}$N, $^{20}$Ne, $^{32}$S, $^{40}$Ca and $^{62}$Zn. Note that we do not consider nucleosynthesis by intermediate mass stars. Consequently, we will concentrate our analysis on elements such as O or Fe where restricting to SN production may be a good approximation. Our numerical implementation of the enrichment model has been divided into three stages: SNII element production,

SNIa element production and metal distribution.

### SNII ELEMENT PRODUCTION

In order to estimate the SNII rate we use a Salpeter Initial Mass Function(IMF) with lower and upper mass cut-offs of 0.1 and 40 $M_\odot$, respectively, and assume that stars more massive than $8M_\odot$ end their lives as SNII[2]. For the chemical production, we adopt the yields of Woosley & Weaver (1995). These are metal-dependent yields and vary differently for different elements. We use half of the iron yield of Woosley & Weaver (1995), as it is often adopted (e.g. Timmes et al. 1995). For the sake of simplicity, in most of our simulations we assume that SNeII explode (i.e. produce and eject the chemical elements) within an integration time-step of the code (which is typically $\leq 10^6$ yr), because SNeII originate in massive stars which have very short characteristic life-times of the order of $10^7$ yr. However, we have also analysed the effect of relaxing this instantaneous recycling approximation for SNII (see Section 2.2.2).

### SNIA ELEMENT PRODUCTION

As a progenitor model, we adopt the W7 model of Thielemann et al. (1993), which assumes that SNIa explosions originate from CO white dwarf systems in which mass is transferred from the secondary to the primary star until the Chandrasekhar mass is exceeded and an explosion is triggered. It is generally assumed that the life-time of such a binary system is in the range $\tau_{\rm SNIa} = [0.1, 1]$ Gyr, depending on the age of the secondary star (Greggio 1996). In our model, the material produced by a SNIa event is ejected when a time $\tau_{\rm SNIa}$ after the formation of the exploding star has elapsed. We choose this time randomly within a given range (in most of our experiments we assume $\tau_{\rm SNIa} = [0.1, 1]$ Gyr). In order to estimate the number of SNIa, we adopt an observationally motivated range for the relative ratio of SNII and SNIa rates (e.g. van den Bergh 1991). We use the chemical yields of Thielemann et al. (1993) for the metal production.

### METAL DISTRIBUTION

We distribute chemical elements ejected in SN explosions within the gaseous neighbours of exploding star particles, using the usual SPH kernel interpolation technique (Mosconi et al. 2001). Each neighbouring gas particle receives a fraction of the

[2]The IMF gives the number of stars of each mass which are formed from a given amount of stellar mass. In other words, we can use the IMF to estimate the number of stars of each mass in our star particles, allowing the counting of stars which will explode as SNII or SNIa.

ejected metals according to its kernel weight. For this purpose, gas particle neighbours of stellar particles are identified whenever metal distribution has to take place, and smoothing lengths for these stars are calculated by setting a desired number of gas neighbours that should be enclosed in the smoothing length (we have assumed the same criterium used for the smoothing lengths of gas particles). This is particularly important for the enrichment by SNIa because of the time-delay between the formation of the stars and the ejection of metals. Note that after a star particle is created, it is only subject to gravitational forces, unlike the gas particles, which continue to be subject to hydrodynamical forces as well. Consequently, as the system evolves, star particles can release metals associated with SNIa explosions in a different environment from where they were born. This, together with the different lifetimes and yields of SNII explosions, can then produce non-trivial variations in abundance ratios.

### 2.1.3 GAS COOLING

It is well known that the cooling rate of thin astrophysical plasmas depends sensitively on metallicity, in such a way that at a given density, the cooling rate is higher for a higher metallicity. In Fig. 2.1 we show the cooling functions computed by Sutherland & Dopita (1993) from primordial (i.e. no heavy elements) to supra-solar abundance ([Fe/H]=+0.5). As one can see from this figure, the cooling function can show very large variations with the metal abundance of the gas, depending on the temperature range considered. For example, the usual estimates of the cooling time ($\tau_{\rm cool}$) for a gas particle at the critical density ($\rho_*$) and at a temperature of $T_* = 4 \times 10^4$ K yields that $\tau_{\rm cool}$ is 50 times larger for primordial gas than for a mildly supra-solar medium ([Fe/H]= 0.5), 18 times larger than that of a solar abundance one, and still twice as large as the corresponding time for gas with [Fe/H]= $-1.5$. The temperature range of $[10^5 - 10^6]$ K shows the largest differences, right in the temperature range relevant to the abundant population of dwarf galaxies.

Including effects owing to metal line cooling is therefore crucial for realistic modelling of galaxy formation because it affects directly the relation between cooling time and dynamical time of forming galaxies. We therefore include a treatment of radiative cooling consistent with the metal content of the gas component produced by the enrichment model. We use the tables computed by Sutherland & Dopita (1993) for the metal-dependent cooling functions, and interpolate from them for other metallicities as needed. For particles with iron abundance larger than 0.5, we adopt the supra-solar cooling rate (i.e. the one for [Fe/H]$>$ +0.5). In cosmological simulations, we also include a redshift dependent photo-heating UV background, with an intensity evolution that follows the model of Haardt & Madau (1996).

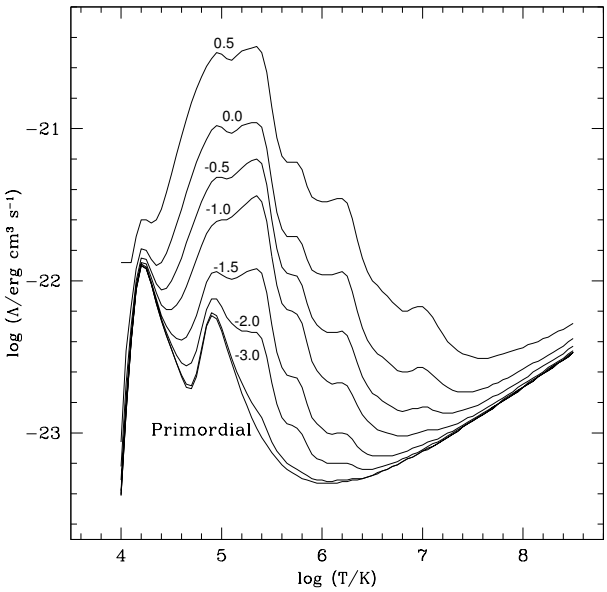


Figure 2.1: Cooling rates for gas of different metallicities, as given by the [Fe/H] abundance, from supra-solar ([Fe/H]=0.5) to primordial. The plot is based on data adapted from Sutherland & Dopita (1993).

## 2.2 RESULTS FOR ISOLATED GALAXY MODELS

As first tests of our model, we consider simulations of isolated haloes set up to form disk galaxies at their centre. This allows us to examine the dependence of the results on resolution and on different parameters of the chemical enrichment model. The initial conditions consist of a static dark matter potential corresponding to a Navarro, Frenk & White profile (1996, 1997; see Appendix B) of concentration $c_{\rm NFW} = 20$, and a baryonic gas phase initially in hydrostatic equilibrium in this potential. Our typical system has virial mass $M_{\rm vir} = 10^{12}\,h^{-1}M_\odot$ ($h = 0.7$), 10% of which is in the form of baryons ($M_{\rm bar} = 10^{11}h^{-1}\ M_\odot$). The initial radius of the system is $r_{\rm vir} = 160\,h^{-1}$kpc and the gas has an initial angular momentum characterized by a spin parameter $\lambda = 0.1$[3]. We have followed the evolution of our test system for $1.5\,\tau_{\rm dyn}$, where $\tau_{\rm dyn} = 7$ Gyr is the dynamical time of the galaxy at $r_{\rm vir}$.

These idealized initial conditions yield a simple model for disk formation which is

[3]This spin parameter is defined as $\lambda = (JE^{1/2})/(GM^{5/2})$, where $J$ and $M$ are the angular momentum and mass of the system, respectively, $E$ its binding energy and $G$ the gravitational constant. For systems entirely supported by rotation, $\lambda = 1$. For a better explanation of the spin parameter, see Appendix C.

an ideal test bench for the performance and validity of the code, and the dependence of the results on the free parameters. We stress however that these models are not meant to provide a realistic scenario for the whole galaxy formation process.

### 2.2.1 NUMERICAL RESOLUTION

Both the star formation process and the distribution of metals can be affected by numerical resolution. Particularly important for our model is the fact that the smoothing length of the particles (i.e. the radius which encloses $\approx$ 32 gaseous neighbours) determines the region where the newly released chemical elements are injected. Mosconi et al. (2001) found that chemical abundances could be oversmoothed in low resolution simulations because metals are distributed over a comparatively large volume and, consequently, are more efficiently mixed with surrounding gas. On the other hand, high numerical resolution could also produce spurious results if the metal mixing mechanism becomes too inefficient. Provided other physical mixing mechanisms are not operating, the simulation results might show an artificially large dispersion in gas metallicities.

In order to test the effects of numerical resolution, we carried out simulations of the isolated disk system described above using three different initial numbers of gas particles: 2500 (R1), 10000 (R2) and 40000 (R3), with mass resolutions of $4 \times 10^7\, h^{-1} M_\odot$, $10^7\, h^{-1} M_\odot$ and $0.25 \times 10^7\, h^{-1} M_\odot$ for R1, R2 and R3, respectively. We have set the gravitational softening to 0.4 $h^{-1}$ kpc. In these three runs we use metal-dependent cooling functions for the gas particles according to the tables by Sutherland & Dopita (1993). In Table 2.1 we summarize the main characteristics of these simulations.

In Fig. 2.2, we show the evolution of the star formation rates obtained for R1 (dotted line), R2 (solid line) and R3 (dashed line). Most of the stellar mass (92%, 88% and 86% in R1, R2 and R3 respectively) is formed at times $t < 3$ Gyr (43% of the dynamical time) in the three runs. Only at later times, we find that the lowest resolution test simulation (R1) yields a significantly lower result for the SFR, indicating that the number of gas particles has dropped so much by the conversion into stars that discrete effects become appreciable. However, the final stellar mass fraction (i.e. stellar mass formed divided by the total baryonic mass) are very similar in R1, R2 and R3.

This can be also appreciated from Fig. 2.3, where we show the mass-weighted metallicity profiles for R1 (dotted line), R2 (solid line) and R3 (dashed line), in the inner region and for the stellar (left column) and gaseous (right column) components, for three different times, $t = 0.13$ Gyr (upper panels), $t = 2.5$ Gyr (middle panels) and $t = 7$ Gyr (lower panels). We can see from this figure that the stellar abundance profiles are insensitive to resolution. The mean iron abundance differs by less than 0.03 dex between the different simulations. Recall that the stellar metallicity of

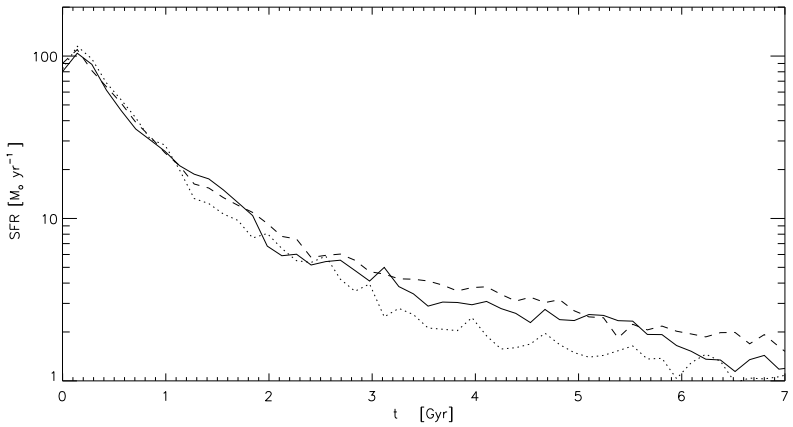


Figure 2.2: Evolution of the star formation rate for our test simulations of isolated disk galaxies, as a function of different numerical resolution. R1 (dotted line) has 2500 particles, R2 (solid line) 10000 particles, and R3 (dashed line) 40000 particles.

Table 2.1: Chemical model parameters for the different tests of the idealized isolated galaxy: initial number of gas particles $N_{\rm gas}$, typical life-times associated to SNII ($\tau_{\rm SNII}$) and SNIa ($\tau_{\rm SNIa}$) in Gyr, rate of SNIa and cooling functions adopted.

| Test | $N_{\rm gas}$ | $\tau_{\rm SNII}$ | $\tau_{\rm SNIa}$ | Rate$_{\rm SNIa}$ | Cooling Function |
|---|---|---|---|---|---|
| R1 | 2500 | 0 | $0.1-1$ | 0.0015 | Metal-dependent |
| R2 | 10000 | 0 | $0.1-1$ | 0.0015 | Metal-dependent |
| R3 | 40000 | 0 | $0.1-1$ | 0.0015 | Metal-dependent |
| P1 | 10000 | 0 | $0.1-1$ | 0.0033 | Metal-dependent |
| P2 | 10000 | 0 | 0 | 0.0015 | Metal-dependent |
| P3 | 10000 | see Section 2.2.2 | $0.1-1$ | 0.0015 | Metal-dependent |
| PC | 10000 | 0 | $0.1-1$ | 0.0015 | Primordial |
| SC | 10000 | 0 | $0.1-1$ | 0.0015 | Super-solar |

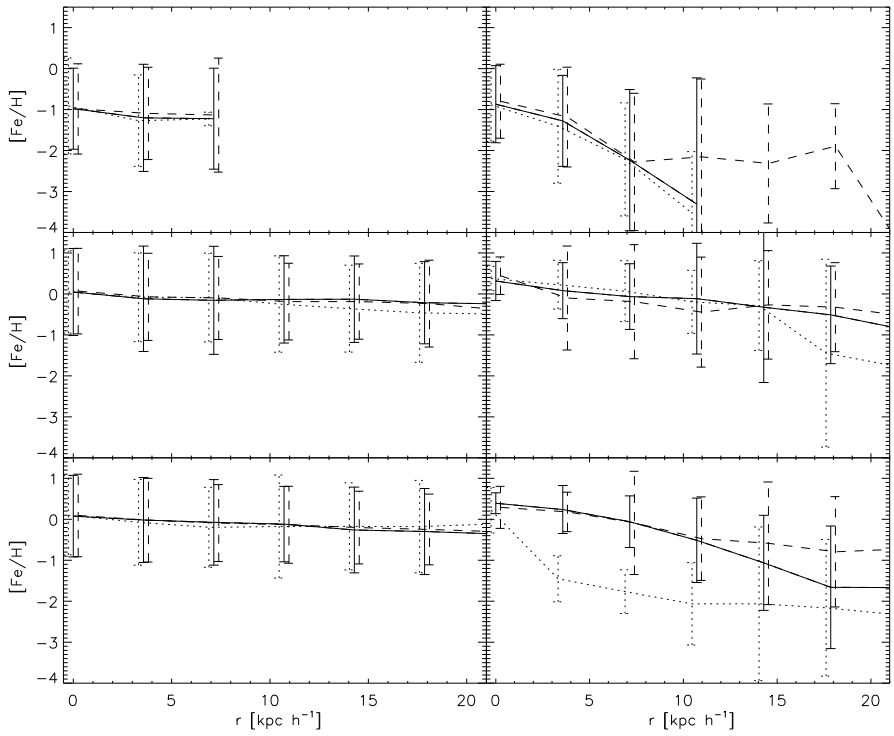


Figure 2.3: Metallicity profiles for the stellar (left panels) and gaseous (right panels) components of the idealized disk tests performed with different resolution: R1 (dotted line, 2500 particles), R2 (solid line, 10000 particles) and R3 (dashed line, 40000 particles). The different rows show different times of the evolution: $t = 0.13$ Gyr (upper panels), $t = 2.5$ Gyr (middle panels) and $t = 7$ Gyr (lower panels). The error bars correspond to the rms scatter of [Fe/H] around the mean in each radial bin.

newly forming stars is given by the local gas metallicity. This is directly visible at the beginning of the simulation where the gaseous and stellar components show a similar level of enrichment in star forming regions (upper panels in Fig. 2.3), while at later stages of the evolution (middle and lower panels) this constraint becomes hidden as a result of the superposition of stars of different ages.

However, as it can be seen from the right panels of Fig. 2.3, the mass-weighted metallicity profiles for the gas components show stronger differences with resolution than their stellar counterparts. At the beginning of the evolution the profiles of the three test simulations are still very similar, although the enriched gas is more spread in the highest resolution test. However, the gas profiles differ more at later times when factors such as variations in the consumption time of the gas and differences in the spatial distribution of stars begin to affect the radial distribution of metals. At the end of the simulations (lower right panel), the mean gaseous iron abundance for R1 is significantly lower than those for the other two simulations. This decrease in the metallicity is produced by the infall of less enriched gas. This gas is not dense enough to trigger star formation activity at the level of R2 and R3, and the infall tends to dilute the metal content in the interstellar medium. Hence the fact that the gas component in R1 shows a lower iron abundance is driven by its poorer gas resolution. Note that as a result of the consumption of most of the gas, the final number of gas particles in R1 is very low ($\sim 60$ in the inner 30 kpc), and as a consequence, the distribution of metals in the gas component is strongly affected by numerical noise. On the other hand, the results for the tests with 10000 and 40000 particles converge quite well both in their stellar and gaseous chemical properties. Note that the rms scatter of particles within each radial bin is similar for the different tests indicating that, on average, the metal mixing is not significantly affected by resolution if we consider at least an initial number of particles of 2500 or more.

### 2.2.2 DEPENDENCE ON ASSUMED SN CHARACTERISTICS

In this Section we analyse the dependence of our results on important input parameters of the chemical model, namely the instantaneous recycling approximation (IRA) for SNII, and the rate and life-times associated with SNIa. For this purpose we run three additional test simulations. In runs P1 and P2, we change the SNIa parameters compared with the simulation R2, which we take as a fiducial reference model, while in run P3 we release the IRA condition for SNII. The main characteristics of these simulations are listed in Table 2.1.

In Fig. 2.4, we compare the evolution of the star formation rate of the standard R2 run (solid line) with P1 (dotted line), in which the SNIa rate was increased. We find no significant differences between the SFRs of these tests. However, we find a larger difference in their stellar age-metallicity relations (AMR), as seen in Fig. 2.5, although the results appear consistent within the standard deviation based

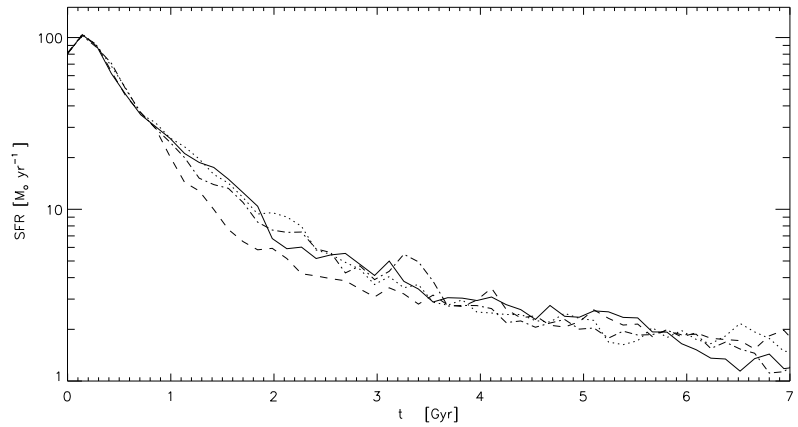


Figure 2.4: Star formation rate for the experiments of the idealized disk galaxy run with different SN parameters: R2 (solid line, standard test), P1 (dotted line, higher SNIa rate), P2 (dashed line, instantaneous recycling approximation for SNIa), and P3 (dashed-dotted line, relaxing the instantaneous recycling approximation for SNII).

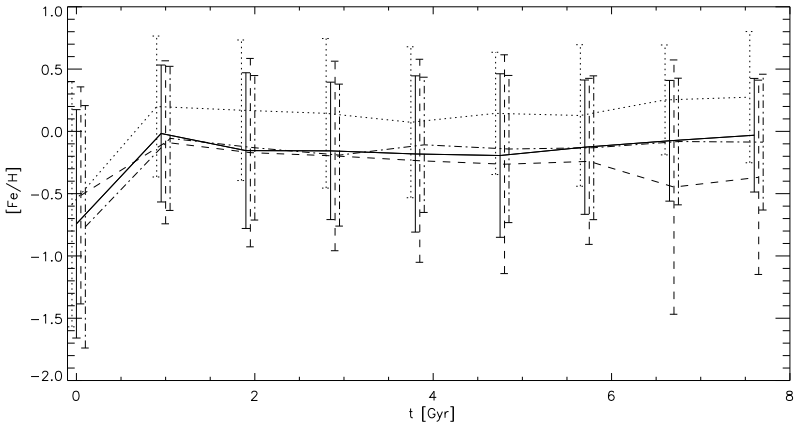


Figure 2.5: Age-metallicity relation for the stellar component in the tests of the idealized disk galaxy run with different SN parameters: R2 (solid line, standard test), P1 (dotted line, higher SNIa rate), P2 (dashed line, instantaneous recycling approximation for SNIa), and P3 (dashed-dotted line, relaxing the instantaneous recycling approximation for SNII). The error bars correspond to the rms scatter of [Fe/H] around the mean.

on counting statistics. In this plot, an increase in the SNIa rate translates into a shift towards larger values of stellar metallicities, since the interstellar medium is more strongly enriched by heavy elements. A change of the SNIa rate also impacts other chemical properties of the systems. For example, in Fig. 2.6 we show the [O/Fe] abundance as a function of [Fe/H] for stars in R2 and P1 at $\tau_{\rm dyn}$. The main difference is found for the high metallicity material ([Fe/H] > -0.5) which shows in P1 a lower $\alpha$-enhancement[4] compared to the one in R2, as expected.

We have also tested the sensitivity of the results on the life-time of binary systems associated with SNIa. The importance of including SNIa has been previously pointed out by Greggio & Renzini (1983) and Mosconi et al. (2001), among others. Motivated by these previous results, we carried out a simulation P2 where we assumed an instantaneous recycling approximation for SNIa explosions (see Table 2.1). The main effect of instantaneously releasing the chemical production of SNIa can be appreciated from Fig. 2.6 which shows the mean $\alpha$-enhancement of the simulated stellar population. These abundance ratios exhibit a behaviour which is in open disagreement with observations (Pagel 1997). Note, however, that these observational results correspond to solar neighbour stars, while the simulated ones include information from the whole stellar component.

Finally, in order to analyse the effects of the instantaneous recycling approximation for SNII, we tested a more detailed calculation of the life-time of massive stars. To this end, we convolved the IMF with the life-time of massive stars at different intervals of metallicity (Raiteri, Villata & Navarro 1996). In this way, we obtained a range of mean life-times varying with stellar metallicity from $6.3\times10^6$yr for $Z = 5\times10^{-4}Z_\odot$ to $1.6\times10^7$yr for $Z = Z_\odot$, where $Z$ denotes mean stellar metallicity and $Z_\odot$ is the solar metallicity. We run a test of our idealized initial condition with the same chemical parameters used in R2 but including these metallicity-dependent life-times for SNII (P3, see Table 2.1). We found no significant differences between the two tests, either in the SFR or in the iron abundance, as can be seen from Figs. 2.4 and 2.5. The similar behaviour of these two runs is also found in other chemical properties of the systems, such as the relation shown in Fig. 2.6. Recall that a drawback of a detailed description of chemical enrichment can be its high computational cost, so an important practical goal is to keep the model sufficiently simple to allow its use in large-scale cosmological simulations. While in this context the IRA for SNIa can in general not reproduce certain observed trends, for SNII it appears to be a simple and sufficiently accurate simplification, at least for these simple tests that do not include energy feedback.

[4]The so-called $\alpha$ elements are those produced by synthesis of $\alpha-$particles: O, Ne, Mg, Si, S, Ca and Ti (elements heavier than $^{12}$C).

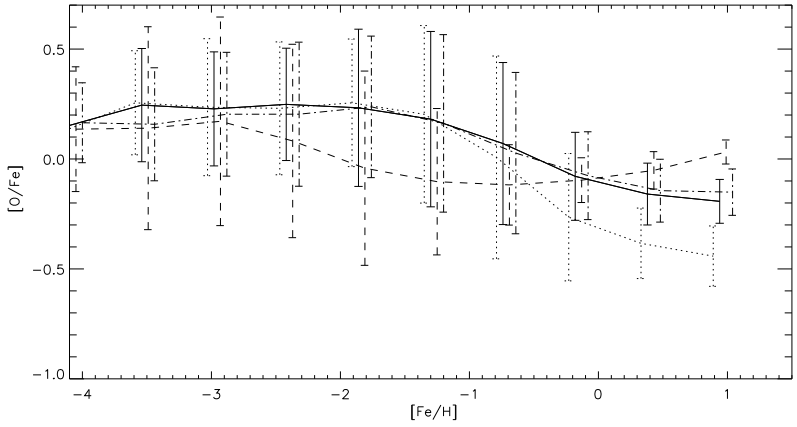


Figure 2.6: [O/Fe] abundance as a function of [Fe/H] for the stellar component in experiments of the idealized disk galaxy run with different SN parameters: R2 (solid line, standard test), P1 (dotted line, higher SNIa rate), P2 (dashed line, instantaneous recycling approximation for SNIa), and P3 (dashed-dotted line, relaxing the instantaneous recycling approximation for SNII). The error bars correspond to the rms scatter of [O/Fe] around the mean.

### 2.2.3 THE EFFECTS OF METAL-DEPENDENT COOLING

Finally, we performed two more runs of our idealized isolated galaxy in order to highlight effects owing to a metal-dependent cooling function. In these fiducial tests, we assumed a constant metallicity, either primordial (PC) or supra-solar (SC, [Fe/H]$= +0.5$) for the cooling function. The parameters for star formation and SN rates were the same as in the standard simulation R2 discussed earlier (see Table 2.1).

In Fig. 2.7, we compare the evolution of the star formation rate for R2 (solid line), PC (dotted line) and SC (dashed line). In the early stages ($t \leq 4$ Gyr), the test run with supra-solar abundance cooling function (SC) results in a star formation rate higher by up to a factor of 3 compared with the simulation R2 with self-consistent cooling function, while the run PC with primordial cooling lies lower by up to a factor 1.5. After the first 4 Gyr, the SFR in the SC run decreases significantly, indicating that most of the gas has already been consumed and transformed into stars. Likewise, after this period, simulation PC has the highest residual level of SFR as a result of the larger amount of gas left over and available for star formation.

As a result of the differences in the level of star formation activity among the runs with different cooling functions, the metallicity distribution is also affected. In Fig. 2.8 we show metallicity maps for the stellar components corresponding to

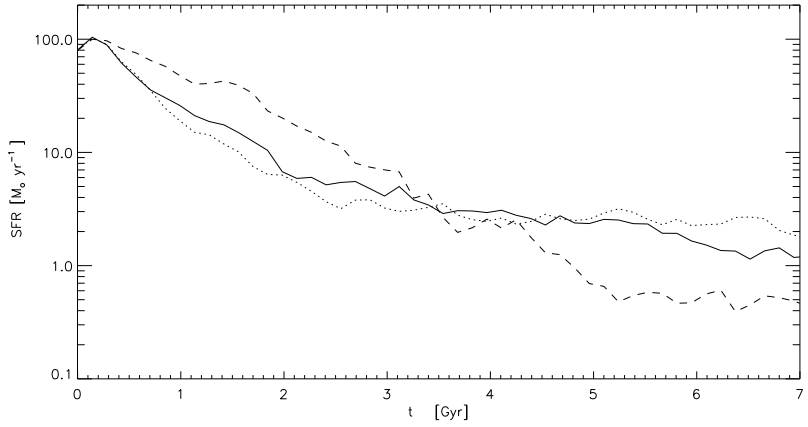


Figure 2.7: Star formation rate for the idealized disk test run with supra-solar (SC, dashed line), primordial (PC, dotted line) and metal-dependent (R2, solid line) cooling functions.

face-on (left panels) and edge-on (right panels) projections of the disks, for the PC (upper panel), R2 (middle panel) and SC (lower panel) simulations. Comparing the upper to the lower panels, the distribution of stars is more extended and the level of enrichment is higher in the SC run. In fact, the increase in the cooling efficiency produces an increase in the star formation activity at larger radius, increasing the amount of metals and affecting their relative distribution. This can also be appreciated from Fig. 2.9 which shows the fraction of baryons in stellar form $f(r)$ as a function of radius for tests R2 (solid line), PC (dotted line) and SC (dashed line) at $\tau_{\rm dyn}$. These fractions were calculated by summing up the stellar mass in radial bins, normalized to the total baryonic mass within the corresponding bin. In particular, at 20 $h^{-1}$ kpc the distribution functions for R2 and SC are 25% and 35% higher than the one for the PC run, respectively. Note that the impact of using different cooling functions becomes more important as we go to outer regions where, in the limiting case of SC, the high cooling efficiency leads to a substantial star formation activity even outside 30 $h^{-1}$ kpc. The behaviour found in this figure is present already in early stages of the evolution. The efficient transformation of gas into stars at larger radius also limits the supply of baryons to inner regions. Hence, the whole mass distribution is affected by the use of different cooling functions. This is clear from Fig. 2.10, where we show the density profiles of the stellar (upper panel) and gaseous (lower panel) components for these tests.

Finally, in Fig. 2.11 we show the mass-weighted oxygen profiles for the stellar (left panels) and gaseous (right panels) components for the tests PC (dotted line), R2 (solid line) and SC (dashed line), at three different times: $t = 0.13$ Gyr (up-

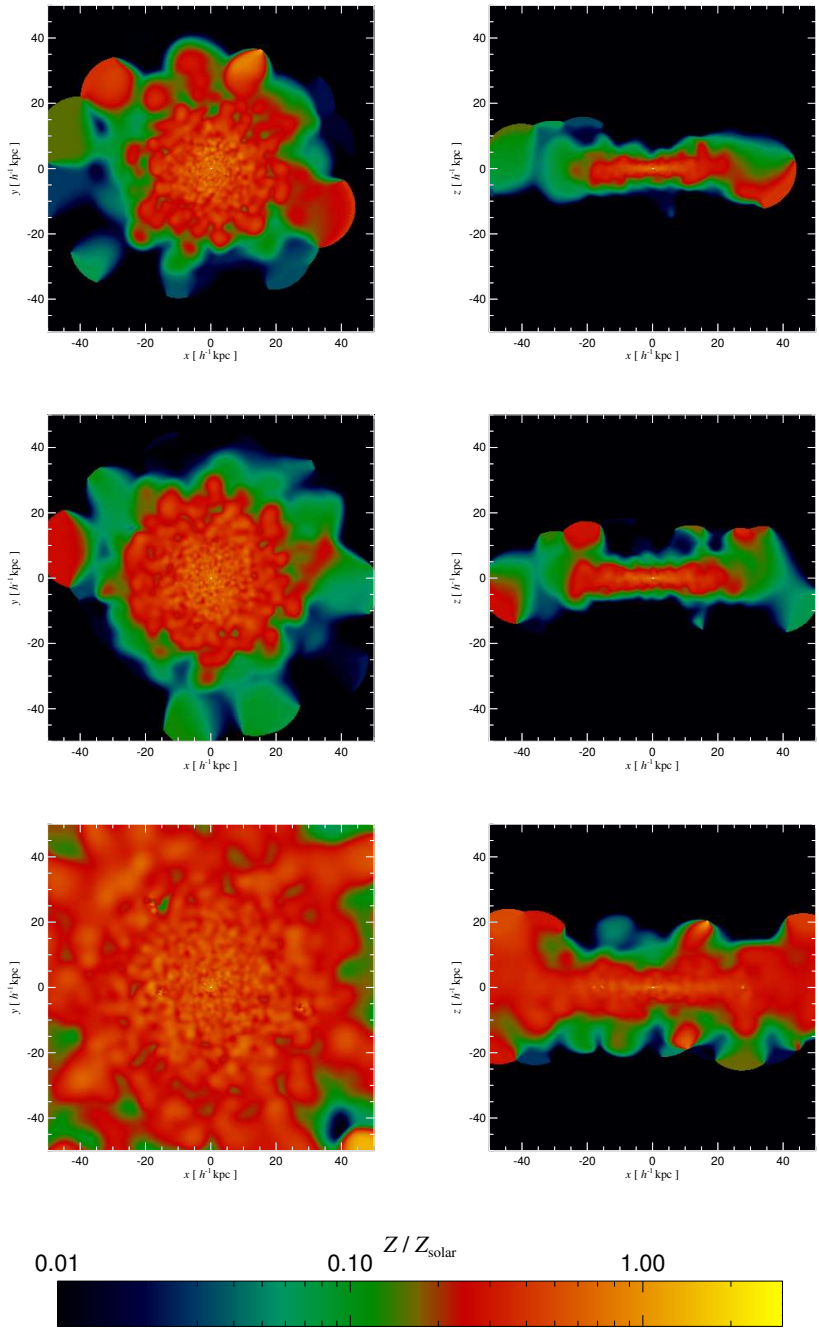


Figure 2.8: Face-on (left-hand panels) and edge-on (right-hand panels) surface metallicity distribution for the stellar component of the isolated disk galaxy tests run with primordial (PC, upper row), metal-dependent (R2, middle row) and supra-solar (SC, lower row) cooling rate functions. The metallicity scale is also shown.

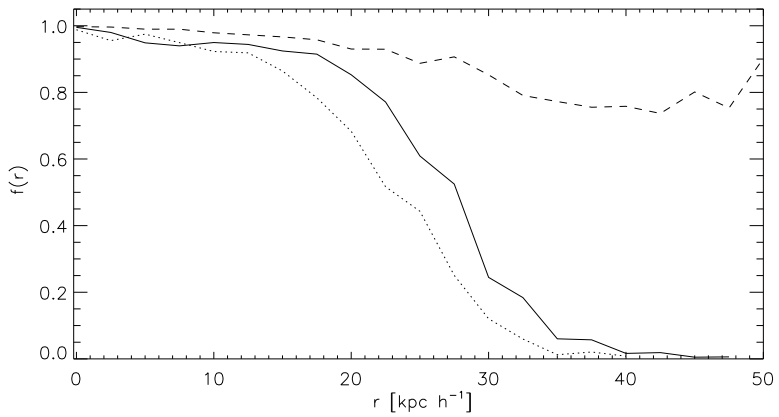


Figure 2.9: Fraction of baryons in stellar form $f(r)$ for the idealized disk tests run with supra-solar (SC, dashed line), primordial (PC, dotted line) and metal-dependent (R2, solid line) cooling functions.

per panels), $t = 2.5$ Gyr (middle panels), $t = 7$ Gyr (lower panels). We find no significant differences in the abundance distributions for the stars in these tests at any time. However, the metallicity of the gaseous component is more sensitive to the adopted cooling functions. At the beginning of the simulations, the results for the three runs are similar but after the initial collapse (middle panel) the level of enrichment increases from PC to R2 and SC, even though the differences remain quite small overall. At $\tau_{\rm dyn}$ (lower panel), both the PC and R2 simulations show decreasing metallicity profiles, conversely to the case of SC which shows a flat relation. Here metals are more uniformly distributed and the ISM is enriched out to larger radii. Recall that the gas metallicities reflect an instantaneous state of the chemical properties of the system, while the stellar population gives an integrated account of the history of the chemical properties of the galaxy.

In summary, the results of this Section have shown that a detailed study of the metallicity properties of galaxies requires a self-consistent treatment of radiative cooling that accounts for metal line cooling. The resulting effects will, however, depend strongly on how heavy elements are spread into diffuse unenriched gas. In the next Chapter, we will investigate a more realistic initial condition to simulate the formation of a spiral-like galaxy by using our chemical enrichment code. We will analyse a high resolution simulation consistent with a cosmological framework in order to make a detailed comparison of the predictions of our model with observations of the Milky Way. We will use this test to show the main shortcomings found so far in simulations which intend to describe spiral-like galaxies such as our own without introducing the effects of SN energy feedback.

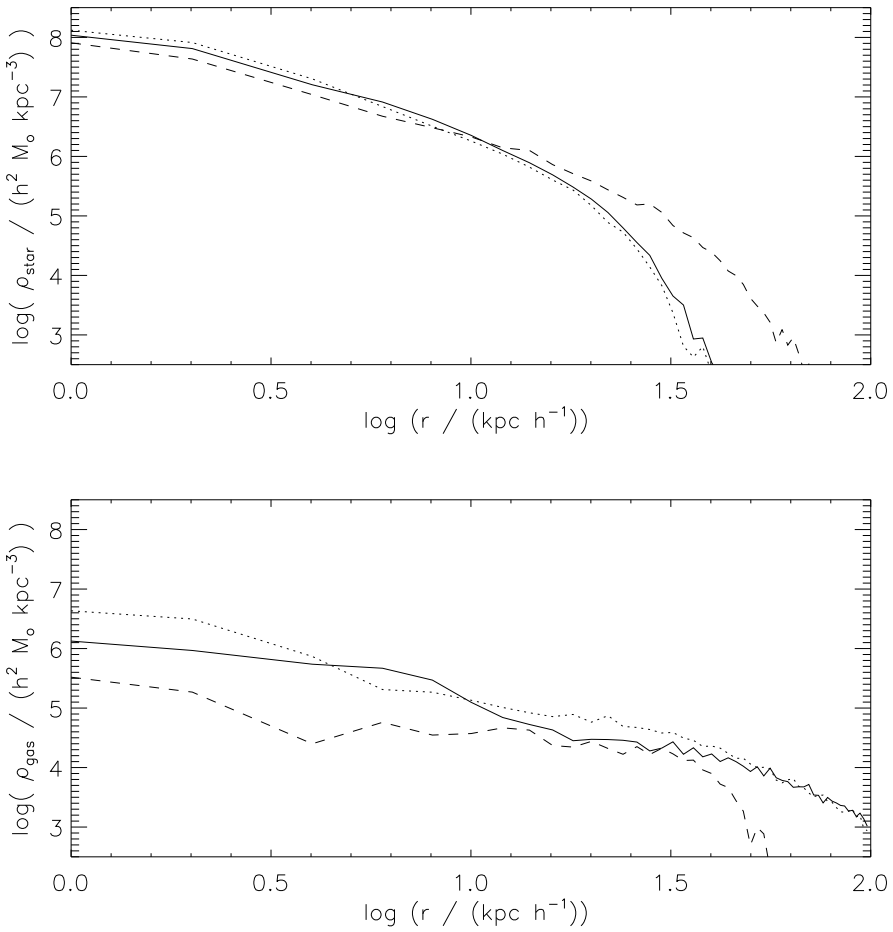


Figure 2.10: Density profiles for the stellar (upper panel) and gaseous (lower panel) components for the idealized disk tests run with supra-solar (SC, dashed line), primordial (PC, dotted line) and metal-dependent (R2, solid line) cooling functions.

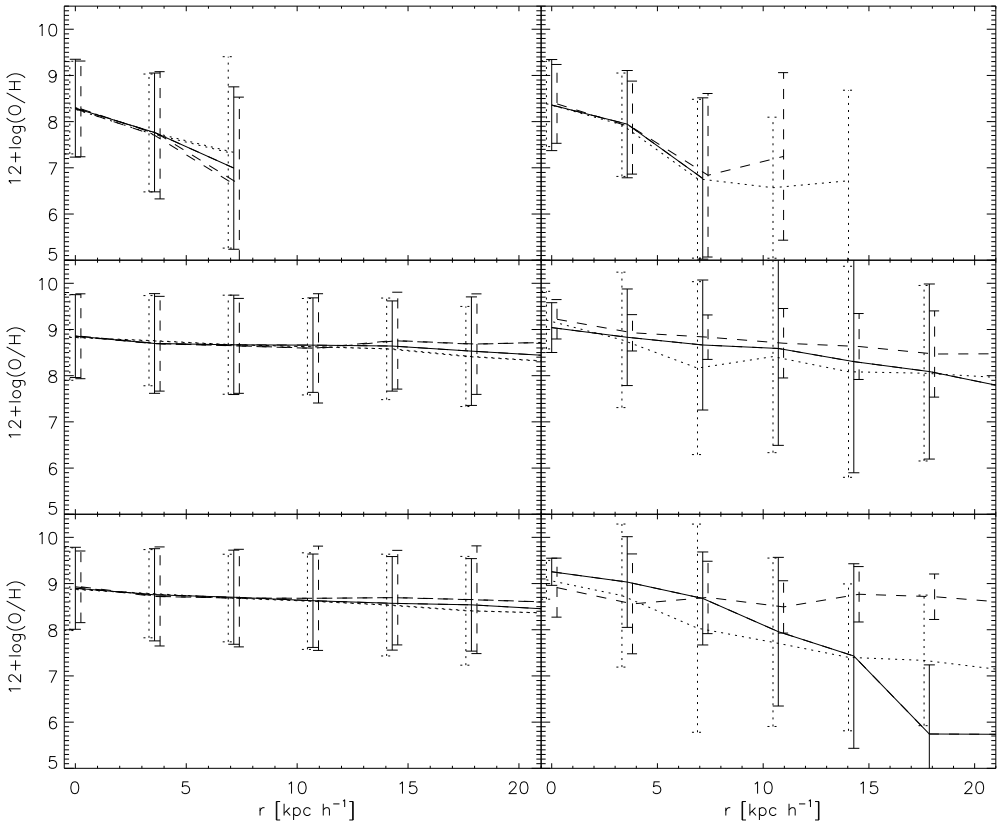


Figure 2.11: Oxygen profiles for the stellar (left panel) and gaseous (right panel) components in experiments of the idealized disk galaxy run with different cooling functions: R2 (solid line, metal-dependent cooling), PC (dotted line, cooling function for primordial abundance) and SC (dashed line, cooling function for supra-solar abundance). The error bars correspond to the rms scatter of 12 +log (O/H) around the mean.

# Chapter 3

# Disk Formation

The formation of spiral galaxies is nowadays a subject of utmost importance in cosmology. Spiral galaxies have several recognizable baryonic components which probably appeared at different stages during the formation process. These are disks, stellar bulges, stellar haloes, eventually bars. Recent observations have shown that the different components of disk galaxies have distinct properties such as kinematics, metallicities and formation ages. Understanding the origin of these characteristic properties has become one of the most widely investigated problems in current astrophysics, since they can store fossil records of the formation epoch.

From a theoretical point of view, the formation of disk configurations is well posed on the basis of specific angular momentum conservation of the baryons during the collapse and relaxation of gas into the dark matter potential wells (Fall & Efstathiou 1980; see Appendix C). Within this context, dark matter and baryons get the same specific angular momentum before collapse (Peebles 1969) and provided baryons conserve this momentum, their collapse leads to a disk-like configuration of the gas into the dark matter potential wells. If stars can form from this rotationally supported gas, then spiral patterns such as those observed can develop.

The formation of the bulge component is a more controversial issue. Several processes have been proposed for the formation of bulges, such as monolithic collapse (Gilmore & Wyse 1998), mergers (Kauffmann, Guiderdoni & White 1994) and secular evolution (Pfenniger & Norman 1990). Currently, it is believed that they may act together as part of the process of bulge formation. The origin of the other components of spirals is also still far from understood. In particular, the stellar halo in our Milky Way is believed to arise as a result of accretion of satellites (Searle & Zinn 1978). The great variety of physical processes involved in the formation of the different components of spiral galaxies make their study a difficult task.

During the last decades, intense research has been carried out in order to try to understand the formation of disk galaxies and the origin of their different components. Numerical simulations have shown to be an important tool owing to their ability to describe the non linear, coupled evolution of the dark matter and baryons,

and to test different working hypothesis. However, numerical simulations have found severe complications, mainly related with the formation of the disk component. The main problem is known as the *catastrophic angular momentum loss*, and arises because the gas components tend to transfer most of their angular momentum to the dark matter haloes. As a consequence, the resulting disks are too small and compact in comparison with observational results (e.g. Navarro & Benz 1991; Navarro & White 1994). The catastrophic angular momentum loss is a severe problem in the framework of hierarchical clustering, since centrifugally supported disks are unstable to rapid fluctuations in the gravitational potential such as those produced by mergers and accretion of satellites (Toth & Ostriker 1992; Quinn, Hernquist & Fullagar 1993; Velazquez & White 1999). Hence, the survival of extended disks observed in present galaxies points to a mass accretion history in which major mergers did not play a fundamental role, at least in the recent past history. This is difficult to reconcile with a hierarchical universe unless angular momentum loss is prevented under certain circumstances.

Regarding the angular momentum problem, recent simulations have shown some promising advances. Domínguez-Tenreiro, Tissera & Sáiz (1998) found that the formation of compact stellar bulges can stabilize the disks and thereby prevent the angular momentum loss during violent minor merger events, such that disk systems that resemble observed galaxies are obtained. Abadi et al. (2003) have also demonstrated the importance of a dense, slowly rotating spheroidal component, and pointed out its relevance for comparing simulated and observed galaxies consistently. More recently, Robertson et al. (2004) were able to produce large, stable disk systems in their cosmological simulations which are comparable in size to spiral galaxies. In their approach, they introduced a subresolution model for star formation and feedback which pressurizes the star-forming gas and stabilizes disks against fragmentation. We note that all these studies agree on the need for a self-consistent treatment of SN feedback as a crucial mechanism to regulate star formation and to reproduce disks similar to observational counterparts.

In this Chapter we analyse the formation of a disk-like galaxy in a cosmological context by using the simulation code described in the previous Chapter which only includes chemical enrichment. In particular, we focus on the basic shortcomings of current simulations and the main limitations they pose. This Chapter is organized as follows. In Section 3.1 we summarize the main characteristics of our test simulation of a disk-like galaxy in a cosmological context. We use this test to analyse the properties of the galaxy at redshift $z = 0$ and investigate the formation process (Section 3.2.1). We then study several important galaxy properties such as morphology (Section 3.2.3), dynamics (Section 3.2.2), star formation history (Section 3.2.5), angular momentum (Section 3.2.4) and chemical abundances (Section 3.2.6). We refer the interested reader to Appendix C for a summary of the main pillars in the standard disk formation theory, and to Appendix D for a description of the so-called

"bulge-disk decomposition" method, which we use as a diagnostics to quantify the structural properties of our simulated galaxies.

## 3.1 A SIMULATION OF THE FORMATION OF A DISK SYSTEM

As it was mentioned above, current simulations which tend to describe the formation of spiral galaxies generally fail, mainly because of the difficulty in generating extended disk components. In order to describe the main complications that numerical simulations have found so far, we present in this section a simulation of a single galaxy specifically chosen to evolve into a disk-like galaxy at redshift $z = 0$. This is achieved by selecting from a full cosmological simulation a galaxy with no major mergers since redshift $z = 1$. This gives the correct environmental condition to form a disk galaxy. We have used a resimulation technique which allows to simulate a single galaxy with very high resolution, in its correct cosmological setting. For that purpose, a single galaxy is first selected from a full cosmological simulation at redshift $z = 0$. The resimulation technique consists on building a power mass spectrum with the mass resolution determined by the relative distance to the selected galaxy. Particles lying far away from the target galaxy are clumped to form a series of superparticle groups, with decreasing resolution as they lie further away from the selected region. On its turn, this allow to increase the resolution of particles which form the selected galaxy and nearby material. Cosmological, large-scale effects acting on the selected galaxy are then mapped through these superparticles. This allows the description of the history of evolution of a selected galaxy with high resolution, without loosing information on large-scale effects such as mergers, interactions, accretion of sattelites, tidal stripping, etc., which are known to significantly affect galaxy properties.

Our simulation is consistent with a ΛCDM Universe with the following cosmological parameters[1]: $\Omega_\Lambda = 0.7$ (cosmological constant parameter), $\Omega_\mathrm{m} = 0.3$ (mass density), $\Omega_\mathrm{b} = 0.04$ (baryonic mass density), a normalization of the power spectrum of $\sigma_8 = 0.9$ and $H_0 = 100\ h$ km s$^{-1}$ Mpc$^{-1}$ with $h = 0.7$ (Stoehr et al. 2002). The simulation follows the evolution of $\sim 6.5 \times 10^5$ dark matter particles and $\sim 1$ million gas particles initially. This translates into a mass resolution of $1.6 \times 10^7$ and $2.4 \times 10^6$ $h^{-1}$ M$_\odot$ for dark matter and gas, respectively. At redshift $z = 0$, the central galaxy is sampled with $\sim$ 120000, 30000 and 60000 dark matter, gas and star particles, respectively. The selected galaxy and its close surroundings are simulated from redshift $z = 38$ to the current time, $z = 0$. The simulation has been run including our

[1]The dynamics of the expansion of the universe in a cosmological model is governed by the mass density of the univesrse and the energy density associated with the so-called cosmological constant. These are usually parametrized as dimensionless parameters defined as: $\Omega_\mathrm{m} = \rho_\mathrm{m}/\rho\mathrm{crit}$ and $\Omega_\Lambda = \Lambda/3H_0$ where $\rho$ denotes density and $\rho_\mathrm{crit}$ is the critical density of the universe. The baryon density is parametrized as $\Omega_\mathrm{b} = \rho_\mathrm{b}/\rho\mathrm{crit}$.

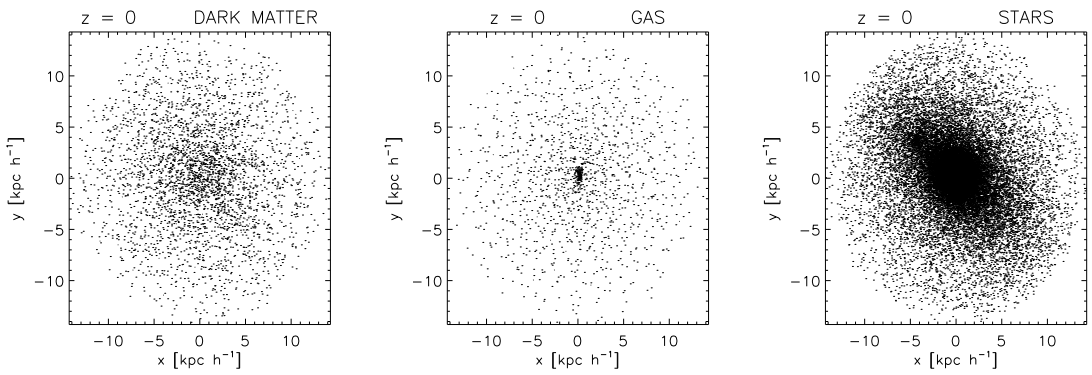


Figure 3.1: Comoving distribution of dark matter, gas and star particles within $1.5 \times r_{\rm opt},$, at redshift $z = 0$, in our simulation of a disk-like galaxy run with our chemical model.

algorithms for star formation, chemical enrichment and metal-dependent cooling, as described in detail in Section 2.2.3. We have assumed a star formation efficiency of $c = 0.1$. As input parameters for the chemical enrichment model we have used a SNIa rate of 0.3 relative to SNII and a SNIa lifetime in the range $[0.1, 1]$ Gyr, we have adopted the instantaneous recycling approximation for SNII, and assumed a Salpeter Initial Mass Function. We have used a maximum gravitational softening of 0.8 $h^{-1}$ kpc for gas, dark matter and star particles.

## 3.2 Results and Analysis

### 3.2.1 The Simulated Galaxy at $z = 0$ and the formation process

In order to analyse the main characteristics of the simulated galaxy at redshift $z = 0$, we plot in Fig. 3.1 the spatial distribution of dark matter, gas and stars. The axis have been chosen in such a way that the angular momentum of the system is aligned with the $z-$axis. From this figure we can appreciate that the simulated galaxy, at redshift $z = 0$, has consumed most of the gas content into stars, leading to a dominant stellar component. The final gas mass fraction for the simulated galaxy, defined as gasesous mass over baryonic mass, within $1.5 \times {r_{\rm opt}}^2$, is $f_{\rm gas} = 0.026$. Note that a disk-like configuration did not develop. The consumption of most of the gas found in this simulation is related to the fact that we have not included here a treatment for SN energy feedback. This process would help to self-regulate the star

[2]The optical radius of a galaxy is defined as the one which encloses 83% of its baryonic mass.

formation activity, producing larger fractions of leftover gas at redshift $z = 0$.

In order to show how the hierarchical formation process took place for the simulated galaxy, we show in Figs. 3.2, 3.3 and 3.4 the spatial comoving distribution of the dark matter, gas and star particles for a series of redshifts. In order to make this plot, we seleced those particles which ended up within $1.5 \times r_{\rm opt}$ of the central galaxy at redshift $z = 0$. These particles were followed back in time in order to construct the formation history of the galaxy. From these figures we can see that, at redshift $z \sim 20$, dark matter has not yet collapsed and the gas component is diffuse. At this redshift, we find that there are no stars formed. However, note that this result can be affected by resolution. In fact, an early population of stars (known as Population-III) is thought to exist even at this high redshift, but the main physical processes related to their formation are not modelled in this code (i.e. molecular hydrogen cooling), since this is out of the scope of this work. As time evolves, dark matter aggregates into larger and larger clumps, where gas cools down and collapses, triggering star formation. In this particular simulation, since energy feedback by SNe is not being considered, most of the gas is transformed into stars once it cools down. As a result, at $z \sim 0$ we find a system whose baryonic component is dominated by stars. The formation process schematized in these plots clearly reflects the hierarchical evolution, in which several distinct structures have been accreted to contribute to the final galaxy. Another interesting aspect of this hierarchical clustering scenario for galaxy formation is that the gas flows to the galaxies through filamentary-like structures.

### 3.2.2 DYNAMICS

In order to test if the baryons in the simulated galaxy at redshift $z = 0$ form a disk-like configuration in rotational support, we study the angular momentum distribution of gas and stars in the galaxy. Assuming circular orbits in a disk-like configuration and a system in solid body rotation, then the angular momentum component ($j_i$) parallel to the total angular momentum ($\mathbf{J}$) of a test particle at a radius $r_i$ from the centre should be correlated according to $j_i \simeq v_{\rm circ} \times r_i$ where $v_{\rm circ} = (GM(r)/r)^{1/2}$ is the circular velocity at radius $r_i$. Note that the $v_{\rm circ}$ value is determined by the total potential well of the galaxy.

In Fig. 3.5 we show the distribution of angular momentum in the direction of $\mathbf{J}$ as a function of projected distance onto the disk plane ($xy$). We plot separately co-rotating and counter-rotating stars and gas particles. We also show the expected theoretical relation, $j_i \simeq v_{\rm circ} \times r_i$. As it can be seen from this figure, a fraction of the gas in our galaxy follows a good correlation between angular momentum and radius, indicating that the gas determines an ordered configuration, as expected from theoretical considerations. However, the angular momentum level is too low in comparison with the expected theoretical value, indicating that the gas has lost

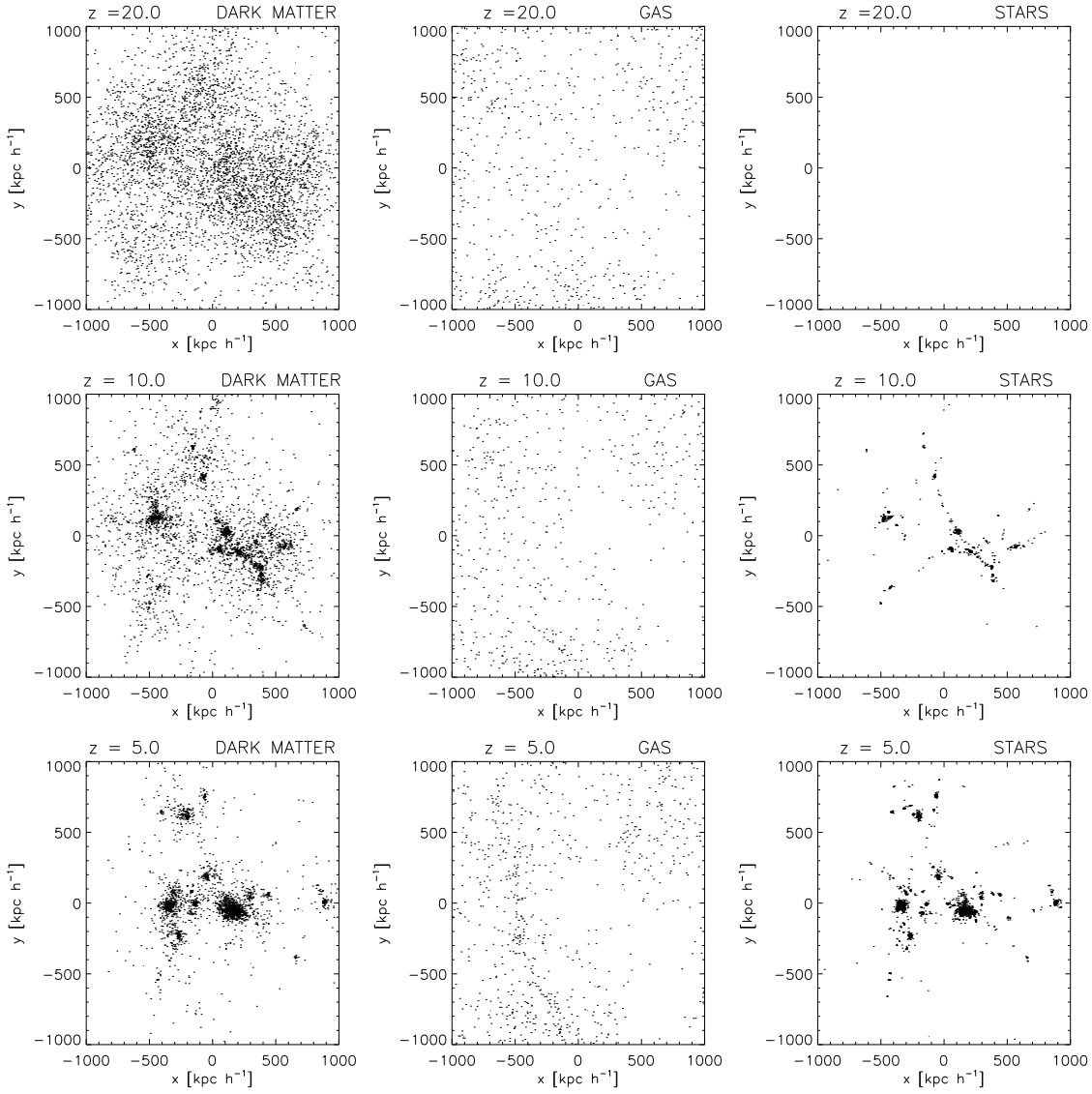


Figure 3.2: Comoving distribution of dark matter, gas and star particles in our simulation of a disk-like galaxy run with our chemical model. The different rows correspond to the indicated redshifts.

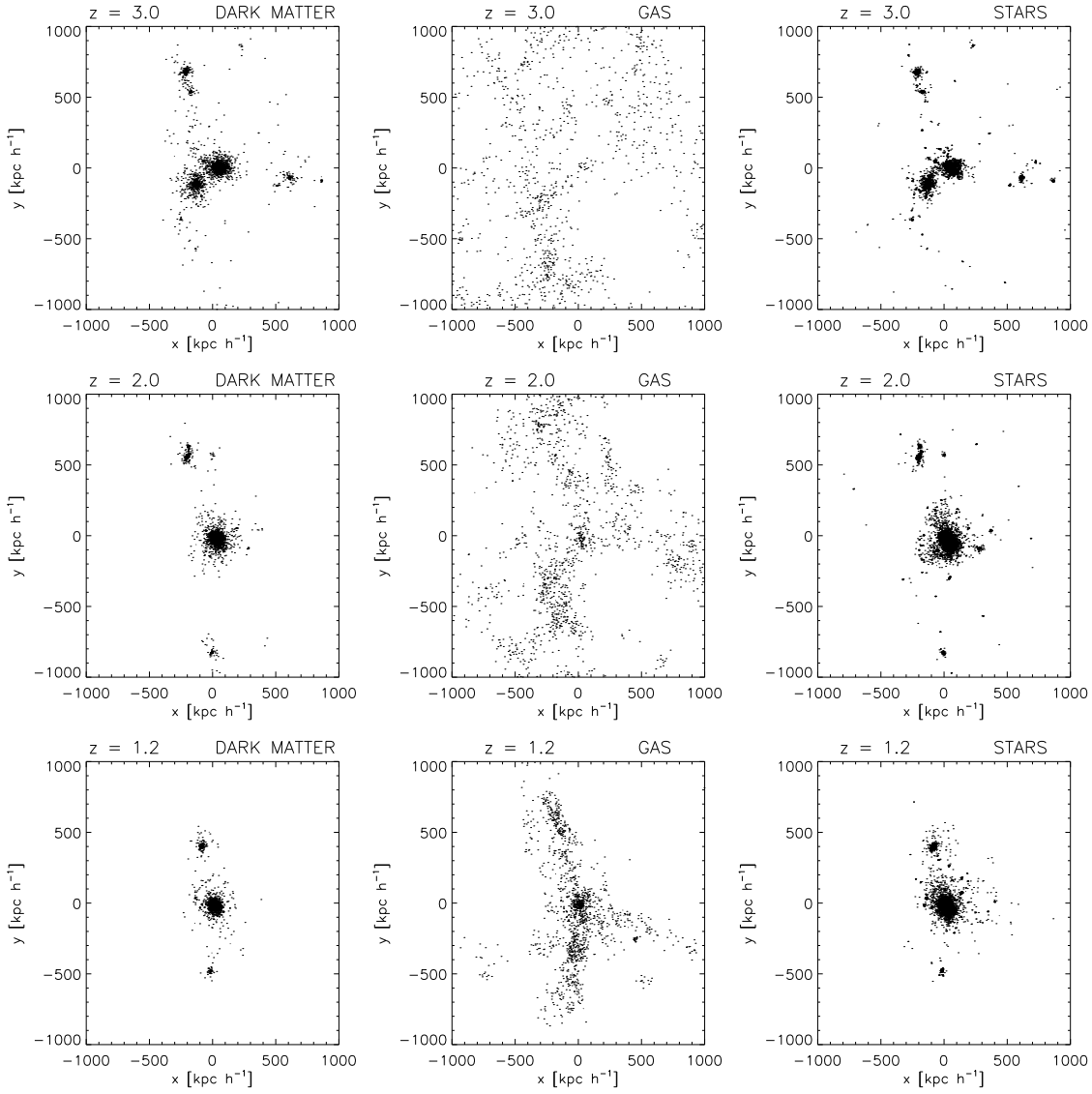


Figure 3.3: Comoving distribution of dark matter, gas and star particles in our simulation of a disk-like galaxy run with our chemical model. The different rows correspond to the indicated redshifts.

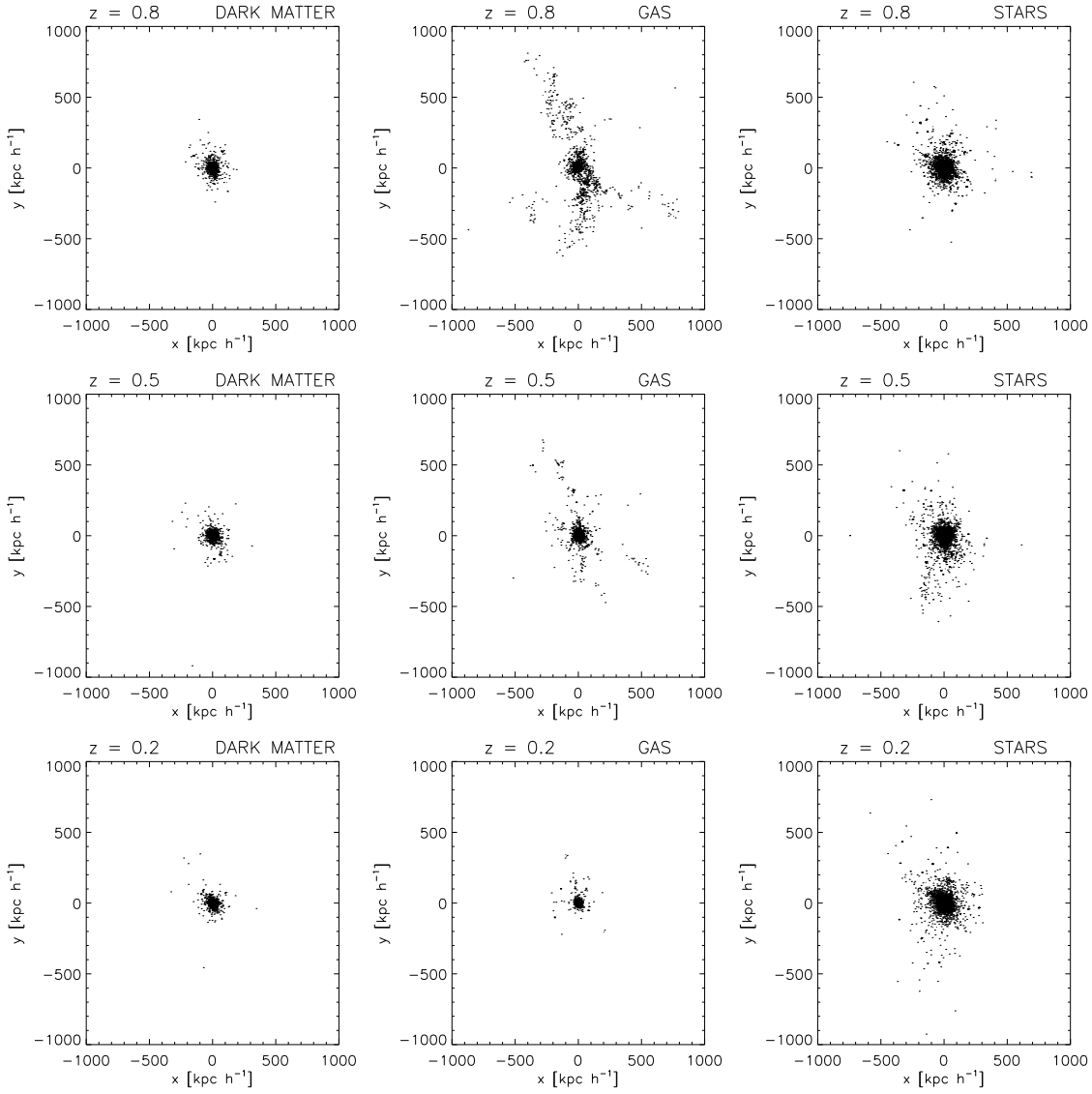


Figure 3.4: Comoving distribution of dark matter, gas and star particles in our simulation of a disk-like galaxy run with our chemical model. The different rows correspond to the indicated redshifts.

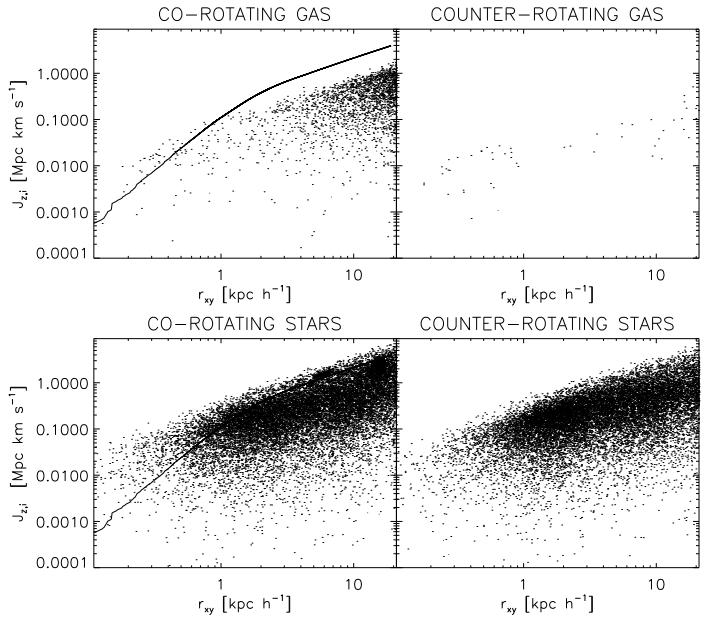


Figure 3.5: Angular momentum for star and gas particles in co- and counter-rotation as a function of projected distance onto the disk plane in our simulation of a disk-like galaxy run with our chemical model. The solid line shows the expected theoretical relation assuming circular orbits in a disk-like configuration, in the corresponding gravitational potential well.

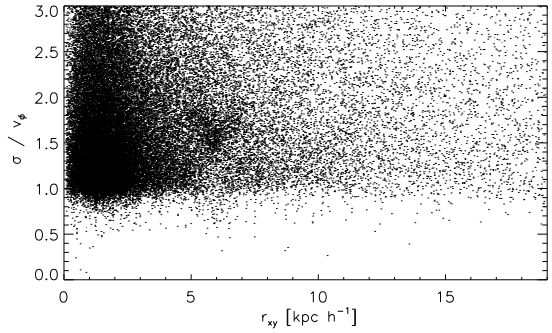


Figure 3.6: Distribution of velocity dispersion over azimuthal velocity, $\sigma/v_\phi$, as a function of projected radius for the stars in our simulation of a disk-like galaxy run with our chemical model.

part of its angular momentum. Note that there are only few gas particles in counter-rotation.

On the contrary, from the lower panels of Fig. 3.5 we can appreciate that the relation between angular momentum and radius for the stellar component is not as tight as in the case of the gas. In fact, an important fraction of the stellar component is in counter-rotation orbits, and although some stars have $j_i$ values in agreement with the theoretical expectation, the spread in angular momentum is large. These figures clearly show that some fraction of the stellar content could be contributing to a disk component. However, most stars have angular momentum distributions which are more consistent with a spheroidal distribution where all possible orbits are taken. It would be expected that such a spheroidal component rotates, although not as fast as a disk-like component. However, observed bulges are always of sizes of a few kiloparsecs and they are not expected to expand up to the optical radius of a galaxy, as we find in this simulation which resembles an elliptical galaxy.

The fact that some stars have angular momentum content in agreement with the expected circular motion laws while the gas has a lower level indicates that the gas might have had a higher angular momentum content in the past, when the high angular momentum stars were formed. Later on, the gas lost part of its angular momentum leading to the detected deficit in relation to the theoretical value.

The dynamical behaviour of the simulated galaxy can be also appreciated from the distribution of velocity dispersion ($\sigma$) over x azimuthal velocity ($v_\phi$) that a test particle should have at the corresponding radius to follow the law for circular motion. Working in cylindrical coordinates, the velocity dispersion for each particle in the galaxy is estimated as:

$$\sigma = [(v_r - < v_r >)^2 + (v_\phi - < v_\phi >)^2 + (v_z - < v_z >)^2]^{\frac{1}{2}} \tag{3.1}$$

where $v_r$, $v_\phi$ and $v_z$ correspond to the radial, azimuthal and vertical velocities, respectively, and $< v_r >$, $< v_\phi >$ and $< v_z >$ are the corresponding mean velocities estimated within cylindrical shells of $\Delta r \simeq 0.1 - 1\ h^{-1}$ kpc defined to have 80 particles per shell. This has been done so that all particles have mean velocities calculated with the same statistical noise. If a particle follows a nearly circular orbit on the plane perpendicular to the angular momentum, then we expect that $v_r = v_z =< v_r >=< v_z >\approx 0$ and $v_\phi \approx< v_\phi >$, so $\sigma/v_\phi \leq 1$. On the contrary, if velocity dispersion dominates, then $\sigma/v_\phi > 1$. Hence, the ratio $\sigma/v_\phi$ measures the departure of orbits from purely circular orbits. In Fig. 3.6 we show the distribution of $\sigma/v_\phi$, at redshift $z = 0$, as a function of projected radius for the stars in our simulated galaxy, which dominate the baryonic component. As it can be seen from this figure, and in agreement with the other analysed quantities, most stars are dominated by velocity dispersion in this simulation.

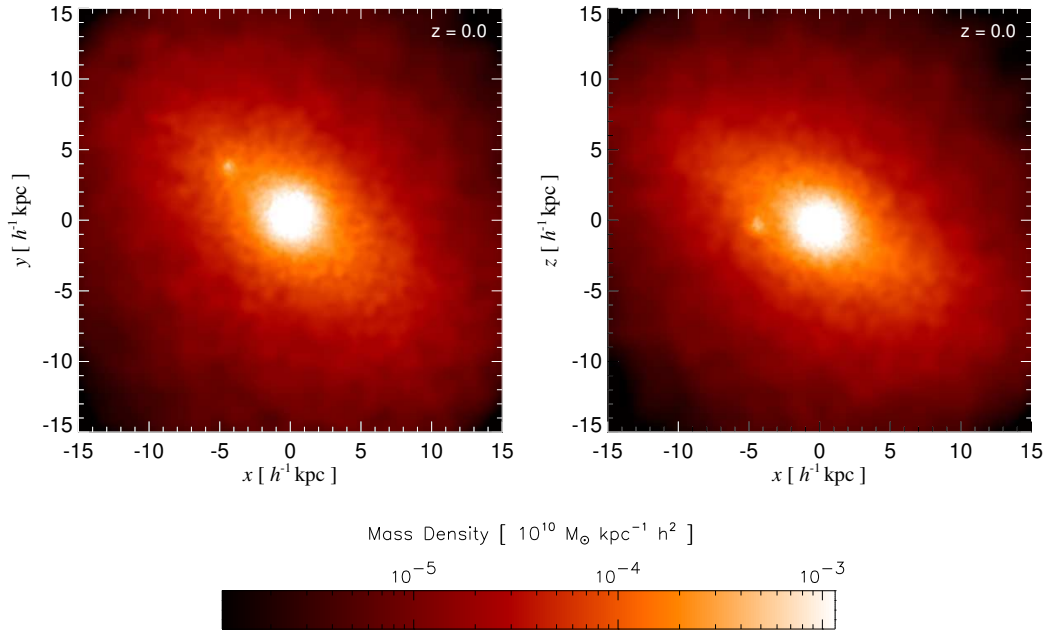


Figure 3.7: Face-on and edge-on projections of the stellar mass density of the disk-like galaxy simulation run with our chemical model. The colour reference is also shown.

### 3.2.3 MORPHOLOGY

In order to better visualize the morphology of the simulated galaxy, we have projected the mass distribution onto planes perpendicular and parallel to the total angular momentum of the system **J**. Hence, these projections correspond to face-on and edge-on views, respectively. In Fig. 3.7 we show these distributions for the stellar mass density at redshift $z = 0$. From these plots we can see that there is no well defined, disk-like configuration which should be present as a flattened structure in the $xz$ plane.

We have also performed a bulge-disk decomposition to the projected surface density onto the disk plane following Eqs. D.1 and D.2 (Appendix D). To this end, we have selected particles within a vertical distance of 4 $h^{-1}$ kpc and with a projected distance of $r_{xy} < 1.5 \times r_{\rm opt}$ in order to avoid contamination by satellites which appear near $r_{xy} \approx 2 \times r_{\rm opt}$. The selection according to optical radius and vertical distance over the disk plane was also done in order to prevent the inclusion of stars of the stellar halo. From the bulge-disk decomposition of our galaxy at redshift $z = 0$ we have obtained the following parameters:

| | |
|---|---|
| Disk scalelength | $r_{\rm d} = 2.31\ h^{-1}$ kpc |
| Bulge scalelength | $r_{\rm b} = 1.00\ h^{-1}$ kpc |
| Bulge Sérsic parameter | $n = 1.01$ |
| Disk central mass surface density | $\Sigma_{\rm d}^0 = 0.183\ {\rm M}_\odot\ {\rm kpc}^{-2}\ h^{-1}$ |
| Bulge central mass surface density | $\Sigma_{\rm b}^0 = 1.31\ {\rm M}_\odot\ {\rm kpc}^{-2}\ h^{-1}$ |
| | |
| Disk mass | $M_{\rm d} = 6.14 \times 10^{10} h^{-1}\ {\rm M}_\odot$ |
| Bulge mass | $M_{\rm b} = 8.31 \times 10^{10} h^{-1}\ {\rm M}_\odot$ |
| Bulge-disk mass ratio | $M_{\rm b}/M_{\rm d} = 1.35$ |
| | |
| Bulge effective radius | $r_{\rm eff} = 1.70\ h^{-1}$ kpc |

These values reflect the absence of an extended disk. Note that although the disk scalelength is 2.31 $h^{-1}$ kpc, the $M_{\rm b}/M_{\rm d} \leq 0.5$ value is more than a factor of 4 larger than that expected for the Milky Way (for spiral galaxies dominated by disks, $M_{\rm b}/M_{\rm d} \leq 0.5$ (e.g. MacArthur et al. 2003)). The disk-like structure is diffuse and does not resemble that of spiral galaxies. Note that the estimation of disk and bulge masses that we have done here assumes that the distributions extend to infinity.

### 3.2.4 ANGULAR MOMENTUM

As it was explained in Appendix C, the specific angular momentum of the different components of a disk galaxy plays a fundamental role in the determination of galaxy properties. In this Section, we analyse the specific angular momentum of bulge-like and disk-like structures in our simulated galaxy in order to show the main shortcomings that standard simulations have found so far in this respect. In order to perform this analysis, we have calculated the specific angular momentum content of the baryons in our simulation. With the aim at comparing our results with available observations of both spiral and elliptical galaxies which can be directly linked to disks and bulges, respectively, we have used baryons within a vertical distance of $|z| < 4\ h^{-1}$ kpc over the disk plane and segregated disk and bulge particles according to projected distance, as we have done in the previous section.

In Fig. 3.8 we show the specific angular momentum of the disk and bulge components of the simulated galaxy, as well as the observed regions occupied by spiral and elliptical galaxies (Fall 1983). From this figure we can appreciate that both the bulge and the disk in our simulation have lower specific angular momentum that that expected from observations. This reveals, once more, the problem of numerical models to match observational expectations. We will show in Chapter 6 that the inclusion of SN energy feedback helps to remedy this problem and produces galaxies with extended, well-defined disks with specific angular momentum comparable to

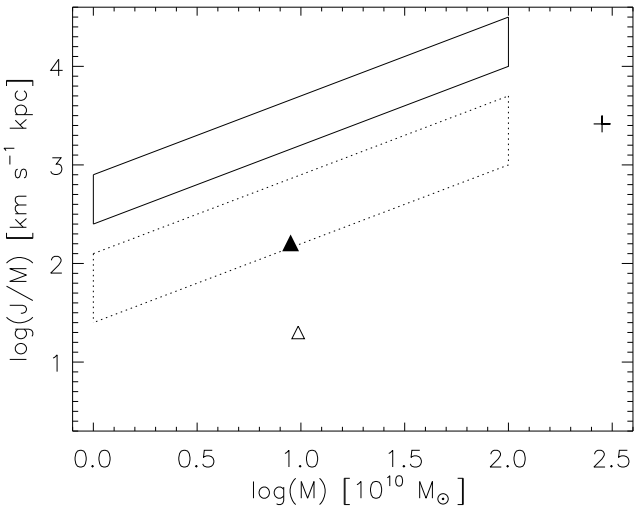


Figure 3.8: Specific angular momentum for the disk (filled triangle) and bulge (open triangle) components in our simulation of a disk-like galaxy run with our chemical model. We have used gas and star particles within $1.5 \times r_{\rm opt}$ and a vertical distance of $|z| < 4\ h^{-1}$ kpc to define the disk and bulge components. The disk was assumed to be formed by particles with $r_{xy} > 2r_{\rm eff}$ and the bulge by particles with $r_{xy} < 2r_{\rm eff}$. The trend does not change if a different condition is used to segregate these components. We also show the result for the dark matter halo (cross). The solid (dotted) area represents the observed values for for spirals (ellipticals).

the observed values.

### 3.2.5 Star Formation History

As it was already mentioned, in this simulation most of the gas is transformed into stars. In fact, this transformation occured during the early stages of evolution. This can be appreciated from Fig. 3.9, where we show the star formation rate for the simulated galaxy. In order to analyse in more detail the star formation process, we have constructed a histogram of the stellar mass fraction as a function of stellar age for the stars in our simulation. We have segregated them into three components in order to compare with observations. In Fig. 3.10 we plot separately disk-like (upper panel) and spheroid-like (bulge and stellar halo, lower panel) components, defined according to the following criteria: the disk is assumed to be formed by stars with $1.5r_{\rm eff} < r < 3.2r_{\rm d}$ and $|z| < 6\ h^{-1}$, where $r$ denotes radial distance and $|z|$ height over the disk plane, the bulge by stars with $r < 1.5r_{\rm eff}$, and the stellar halo stars

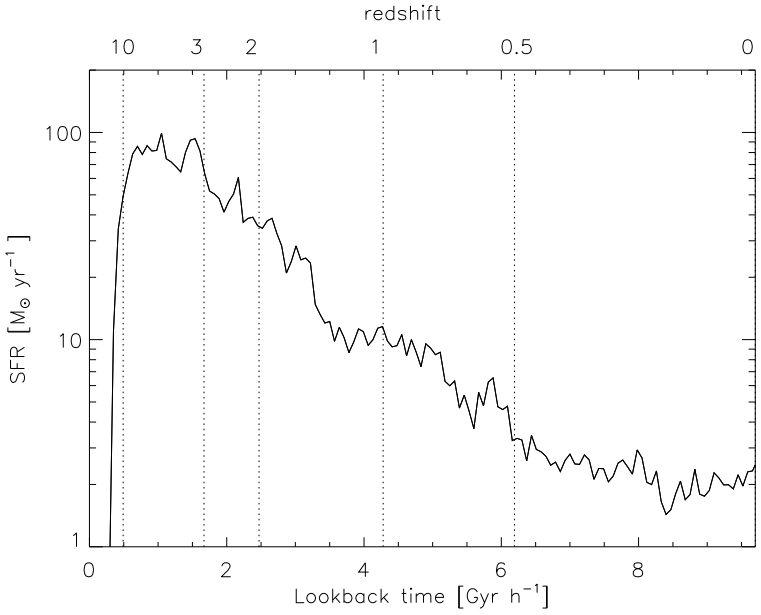


Figure 3.9: Star formation rate as a function of time and redshift for our simulation of a disk-like galaxy run with our chemical model. The plot corresponds to all stars located within $1.5 \times r_{\rm opt}$ at redshift $z = 0$.

with $|z| > 8\ h^{-1}$ kpc. Note that a decomposition into a thin and a thick disk can not be done for this galaxy. These definitions are done in order to analyse general trends of the different components, and our results do not change significantly if other criteria are adopted.

This figure reflects the early transformation of gas into stars. As it can be seen from this figure, most stars, regardless of position in the galaxy, are old with stellar ages $t > 7\ h^{-1}$ Gyr. Note also that new born stars (with $t < 4\ h^{-1}$ Gyr) are only present in the bulge component in open disagreement with observations. This result motivates the inclusion of SN energy feedback which is expected to regulate star formation activity preventing the early gas consumption, through the heating of gas and its transportation outwards. On its turn, these processes would contribute to decrease the gas density and consequently the star formation activity. The availability of gas at later times could then give rise to young disk components and to distinct stellar ages for bulges, disks and stellar haloes (see Chapter 6).

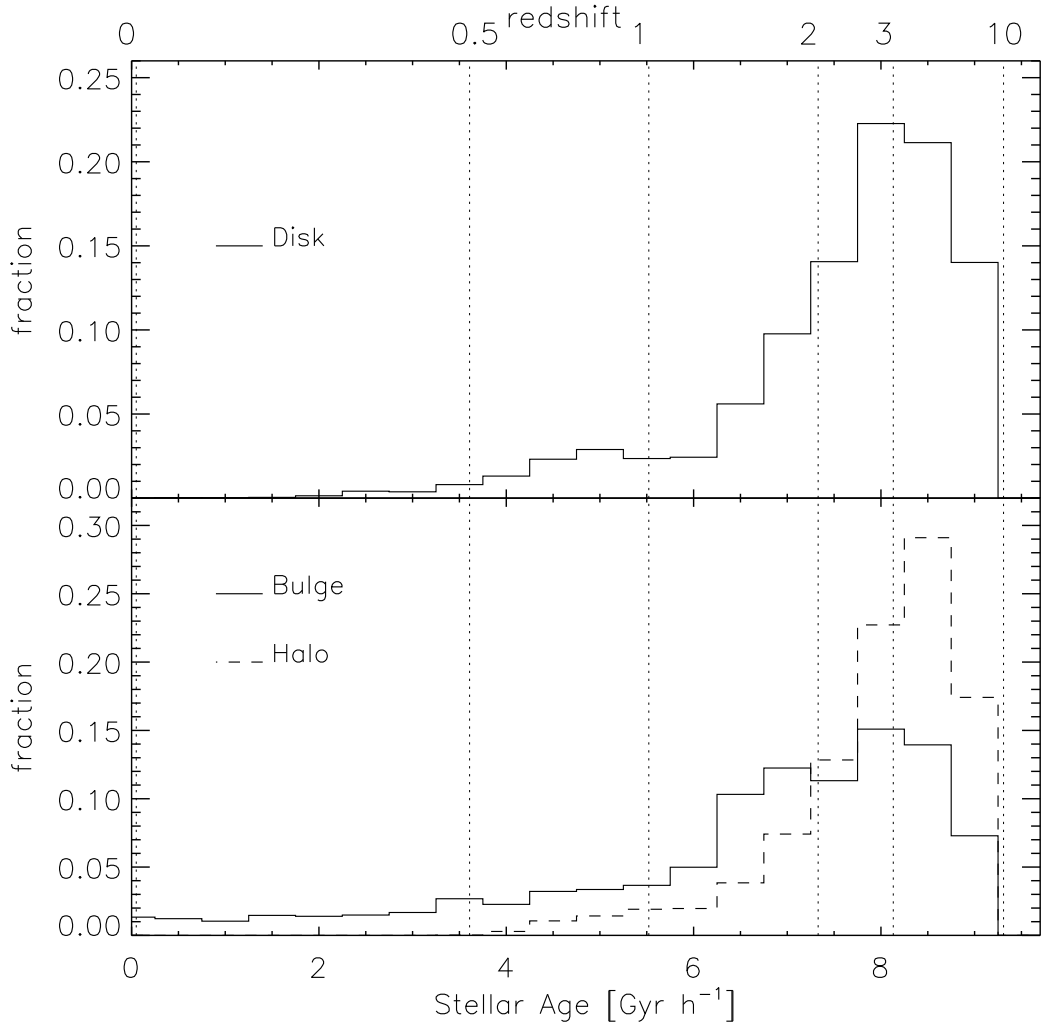


Figure 3.10: Fraction of stellar mass as a function of stellar ages in our simulation of a disk-like galaxy run with our chemical model. Results are for all stars within $r < 1.5 \times r_{\rm opt}$ at redshift $z = 0$, segregated according to the following criteria: the disk is assumed to be formed by stars with $1.5 r_{\rm eff} < r < 3.2 r_{\rm d}$ and $|z| < 6\,h^{-1}$, where $r$ denotes radial distance and $|z|$ height over the disk plane, the bulge by stars with $r < 1.5 r_{\rm eff}$, and the stellar halo by stars with $|z| > 8\ h^{-1}$ kpc.

### 3.2.6 CHEMICAL PROPERTIES

The excess of stars detected in this simulation also leads to a higher metallicity content when it is compared to observational results. In Fig. 3.11 we show the fraction of stellar mass as a function of the iron abundance for stars in the simulated galaxy. We have segregated stars into three components in order to compare with observations. In the plot, we show separately disk-like (upper panel) and spheroid-like (bulge and stellar halo, lower panel) components, defined according to the following criteria: the disk is assumed to be formed by stars with $1.5r_{\rm eff} < r < 3.2r_{\rm d}$ and $|z| < 6\ h^{-1}$, where $r$ denotes radial distance and $|z|$ height over the disk plane, the bulge by stars with $r < 1.5r_{\rm eff}$, and the stellar halo stars with $|z| > 8\ h^{-1}$ kpc. From this figure we can appreciate that the distributions for all components exhibit supra-solar iron abundance peaks. These results disagree with observational results. For the Milky Way Galaxy, the observed mean iron abundances for the bulge, the thin disk, the thick disk and the halo are [Fe/H] $\sim -0.3$ dex (Zoccali et al. 2003), [Fe/H] $\sim -0.2$ dex (Nordström et al. 2004), [Fe/H] $\sim -0.6$ dex (Chiba & Beers 2000), and $-1.5$ (Ryan & Nories 1991), respectively.

The results of this section have shown that simulations in which SN energy feedback is not included can not properly represent the main components of spiral galaxies and their properties. The early transformation of gas into stars and the lack of an efficient mechanism to self-regulate the star formation rate lead to the formation of systems with large central stellar clumps with a roughly spheroidal shape. On its turn, this produces systems with a too high metallicity. The results discussed in this Chapter illustrate the problems found in numerical simulations which do not include heating mechanisms such as SN energy feedback, and point out the relevance of this mechanism in disk formation. In the next Chapter, we will describe a new implementation of SN energy feedback which we have developed in the context of our model for chemical enrichment. This new SN implementation has been designed to avoid the shortcomings presented in this Section and to consistently describe the formation of disk galaxies within hierarchical clustering scenarios (see Chapter 6).

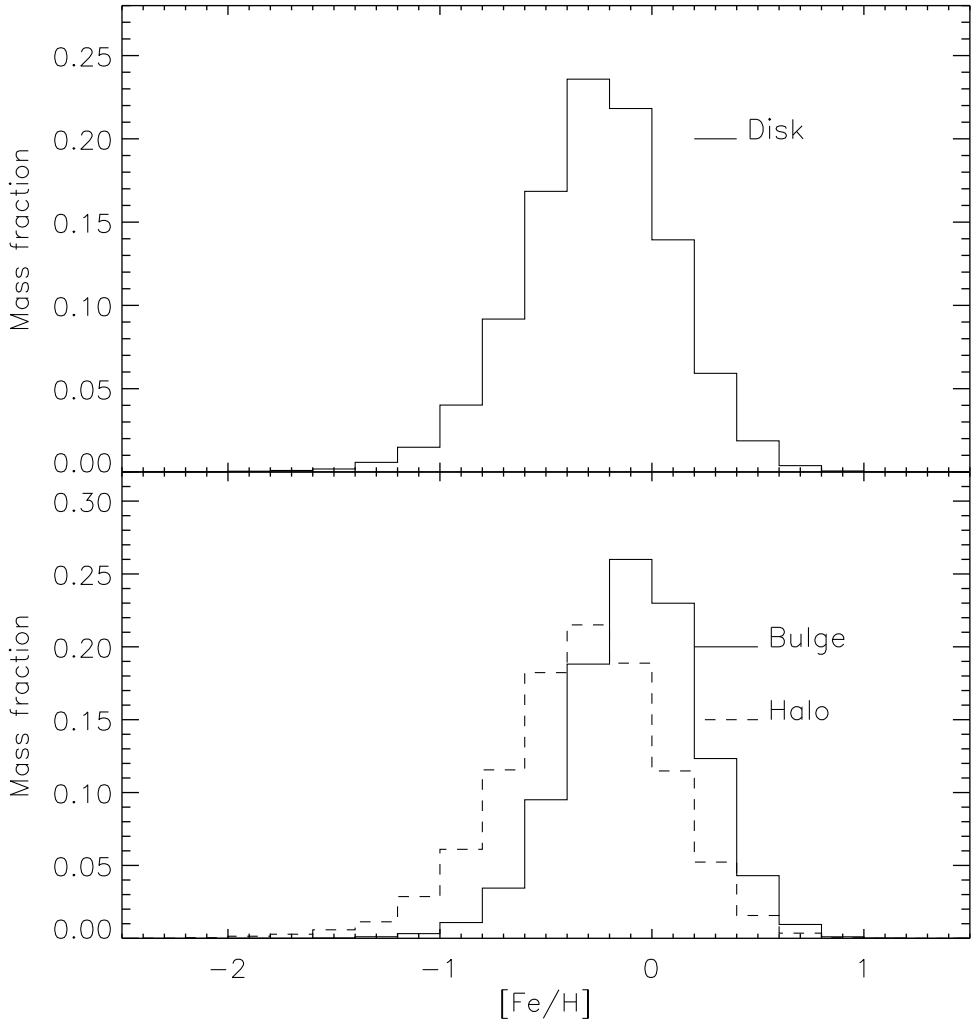


Figure 3.11: Fraction of stellar mass as a function of stellar metallicity for our simulation of a disk-like galaxy run with our chemical model. Results are for all stars within $r < 1.5 \times r_{\rm opt}$ at redshift $z = 0$, segregated according to the following criteria: the disk is assumed to be formed by stars with $1.5r_{\rm eff} < r < 3.2r_{\rm d}$ and $|z| < 6\ h^{-1}$, where $r$ denotes radial distance and $|z|$ height over the disk plane, the bulge by stars with $r < 1.5r_{\rm eff}$, and the stellar halo by stars with $|z| > 8\ h^{-1}$ kpc.

# Chapter 4

# Implementation of multiphase gas and SN energy feedback

The relevance of Supernova (SN) feedback for the evolution of galaxies has been emphasized by numerous observational and theoretical studies. SNe are the main source of heavy elements in the Universe and the presence of such elements substantially enhances the cooling of protogalactic gas (e.g. White & Frenk 1991). On the other hand, the release of energy by SNe heats up the surrounding material, leading to disruption of cold gas clouds and to reduced star formation. This energy can drive enriched material into the outer regions of galaxies or even transport it into the intergalactic medium (IGM, e.g. Lehnert & Heckman 1996; Dahlem, Weaver & Heckman 1998; Rupke, Veilleux & Sanders 2002; Shapley et al. 2004; Frye, Broadhurst & Benítez 2002; Martin 2004). Small systems are thought to be more strongly affected by SNe because of their shallower potential wells which are less efficient in retaining baryons (Larson 1974; White & Rees 1978; Dekel & Silk 1986; White & Frenk 1991). The joint action of chemical enrichment and hydrodynamic heating by SNe is often referred to as 'feedback'. Feedback structures the ISM, establishes a self-regulated cycle for star formation, and ultimately explains the detailed luminosities of galaxies as well as the origin of heavy elements in the IGM and elsewhere. Recent work has emphasized that feedback from AGN may also play a critical role in shaping galaxy evolution (e.g. Di Matteo, Springel & Hernquist 2005; Croton et al 2006). For simplicity, we do not consider such processes in this work.

The treatment of SN energy feedback in simulations of galaxy formation is complicated by the fact that the physical mechanisms which inject energy (and heavy elements) into the ISM act on unresolved scales. Consequently, recipes must be implemented that correctly mimic their combined effects on scales that are resolved. In recent years, a number of authors have developed star formation and feedback recipes for simulating galaxy formation with both mesh-based and SPH codes (e.g. Katz & Gunn 1991; Cen & Ostriker 1992, 1999; Navarro & White 1993; Metzler & Evrard 1994; Yepes et al. 1997; Sommer-Larsen, Gelato & Vedel 1999; Kay et

al. 2002; Lia, Portinari & Carraro 2002; Semelin & Combes 2002; Marri & White 2003; Springel & Hernquist 2003). These studies have shown that simply injecting the energy into the thermal reservoir of surrounding gas is ineffective, producing negligible effects on the hydrodynamics. This is because stars form (and explode) in high density regions where gas cooling times are short. The injected energy is thus radiated before it can drive significant motions (Katz 1992). Such thermal feedback is unable to regulate the star-formation activity or to drive the kind of winds observed in starbursting galaxies.

Several alternative schemes have been proposed to produce more effective SN energy feedback in simulations. For example, Navarro & White (1993) suggested investing the SN energy directly in outward motions imposed on surrounding gas. Gerritsen & Icke (1997) turned off cooling for a brief period after particles acquire feedback energy, allowing them to evolve only adiabatically over this time (see also Mori et al. 1997). Thacker & Couchman (2000) implemented a similar recipe, adjusting the density of heated particles in order to prevent immediate energy losses. More recently, Springel & Hernquist (2003) added galactic winds to their multiphase model by explicitly creating wind particles at a rate proportional to the star-formation rate and assigning them a predefined outward "wind" velocity. While each of these approaches has had some success, it is clear that all have arbitrary *ad hoc* elements and none is fully satisfactory. In particular, all of them introduce characteristic values for wind speeds, mass injection rates, flow times or other parameters which should, in principle, be set by the dynamics of the system and which are likely to vary substantially between systems of different scale, metallicity, etc. Given the central importance of SN feedback in galaxy formation, it remains an important task to improve the numerical treatment of this process in our simulations.

A major limitation of the popular SPH technique (Gingold & Monaghan 1977; Lucy 1977) is its inability to represent multiphase, multiscale mixtures like the interstellar medium in star-forming galaxies. In the SPH formalism, the density associated with a given particle is estimated by averaging over all neighbours within an adaptively defined smoothing region. In a multiphase ISM most of the volume is filled with hot, diffuse gas while most of the mass lies in cold, dense clouds with sizes and masses which cannot be resolved in a galaxy-scale simulation. The density associated with "hot" particles is then overestimated because some "cold" particles lie within the smoothing kernel. This results in overestimation of the associated cooling rate, excessive condensation of cold gas, and too high a star formation rate (Thacker et al. 2000; Pearce et al. 2001). Several *ad hoc* "solutions" of differing complexity have been suggested for this problem. Hultman & Pharasyn (1999) used a two-phase interstellar medium which comprises a hot gas component and cold clouds. These two phases interact with each other through radiative cooling and evaporation of the cold clouds. Pearce et al. (1999, 2001) explicitly decoupled cold and hot phases defined by pre-set characteristic temperature boundaries. Thacker

& Couchman (2001) reduced overcooling by allowing no radiative losses for 30 Myr from particles which had just been heated by supernovae, thereby allowing a wind to develop. Springel & Hernquist (2003) developed an analytic sub-resolution model for the regulation of star-formation in a multiphase ISM, and inserted galactic winds of given velocity and mass-loss rate "by hand". More recently, Harfst et al. (2006) also used a two-phase interstellar medium and assumed a variable star formation efficiency depending on the ISM properties. In this Chapter, we present a new multiphase SPH scheme, similar to that of Marri & White (2003), in which particles with very different thermodynamic variables do not see each other as neighbours. Our model decouples phases with very different specific entropies, based on a local comparison of particle pairs. This allows hot, diffuse gas to coexist with cold, dense gas without introducing *ad hoc* parameters.

In this Chapter, we supplement the model of chemical enrichment already discussed in Chapter 2 with a treatment of multiphase gas and SN energy feedback (Scannapieco et al. 2006). Our primary goal is to address some of the shortcomings of previous implementations within a comprehensive and consistent description of energy and chemical feedback which should then produce realistic galactic outflows. An important advantage of the new scheme is that it avoids *ad hoc* scale-dependent parameters of the kind present in most previous work. This makes our scheme well suited to cosmological structure formation simulations where galaxies with a wide range of properties form simultaneously. In this Chapter, we describe how we treat a multiphase ISM (Section 4.1.1), and implement energy feedback from SN explosions (Section 4.2.1). We also test the performance of these new numerical schemes (Sections 4.1.2 and 4.2.2), which are grafted onto the version of GADGET-2 discussed in Chapter 2, which includes metal enrichment by Type II (SNII) and Type Ia (SNIa) supernovae as well as metal-dependent cooling.

## 4.1 Multiphase gas model

### 4.1.1 Model description

The interstellar medium is known to have a complex, multiphase structure in which interpenetrating components of similar pressure but very different temperature and density span a wide range of spatial scales (e.g. McKee & Ostriker 1977; Efstathiou 2000). This multiphase character is difficult to represent appropriately in numerical simulations. In particular, standard implementations of SPH reproduce it poorly, because they have insufficient resolution to represent clouds of cool, dense gas embedded in a hotter diffuse medium. Numerical artifacts result from the SPH estimate

of gas density which, in a commonly used implementation, can be written as

$$\langle \rho_i \rangle = \sum_j^N m_j W_{ij} \,, \tag{4.1}$$

where $j$ runs through the $N$ neighbours of particle $i$, $m_j$ denotes the mass of particle $j$, and $W_{ij}$ is a symmetrized kernel function. Diffuse phase particles close to a dense cloud overestimate their densities by including cloud particles in the sum over neighbours. This leads to an underestimation of their cooling times and so to excessive accretion of gas onto the cloud (Pearce et al. 1999). This then artificially boosts the star formation rate. A second, more serious problem, also caused by the lack of resolution, is that SN feedback is not channeled into the hot phase but rather is dumped in the dense gas surrounding star-forming regions, resulting in the immediate radiative loss of the energy and the confinement of the metals. This prevents the launching of galactic winds, the ejection of heavy elements, and the self-regulation of star-formation activity.

In order to address these issues and to improve the treatment of the ISM in SPH, we have developed a multiphase scheme which allows a larger overlap of the diffuse and dense gaseous components and can be combined with a more effective scheme for injecting the energy and heavy elements from SNe. The innovation in our scheme relates to the selection of neighbours. If two gas particles have dissimilar thermodynamic properties, they are explicitly prevented from being neighbours in the SPH calculations. In detail, this works as follows. We *decouple* a given particle $j$ from particle $i$, meaning that $j$ is explicitly excluded from the neighbour list of $i$, if the following conditions are fulfilled:

$$A_i > \alpha A_j \,, \tag{4.2}$$

$$\mu_{ij} < c_{ij} \,, \tag{4.3}$$

where $\alpha$ is a constant, $A_i$ is the entropic function of particle $i$, and $\mu_{ij}$ and $c_{ij}$ measure the pair-averaged local velocity divergence and sound speed, respectively. The entropic function characterizes the specific entropy $s$ of gas particles through

$$P = A(s)\rho^\gamma, \tag{4.4}$$

where $P$ denotes pressure and $\gamma = 5/3$ is the adiabatic index for a monoatomic ideal gas. The second condition of Eqn. (4.3) is included to avoid decoupling in shock waves, which, as noted by Marri & White (2003), can lead to unphysical effects when particles on opposite sides of a shock do not "see" each other. Note that we use the artificial viscosity term as parametrized in Eq.(14) of Springel (2005).

As an illustrative example, in Fig. 4.1 we show a typical temperature-density distribution of gas particles in our simulation D12 of an isolated collapsing sphere

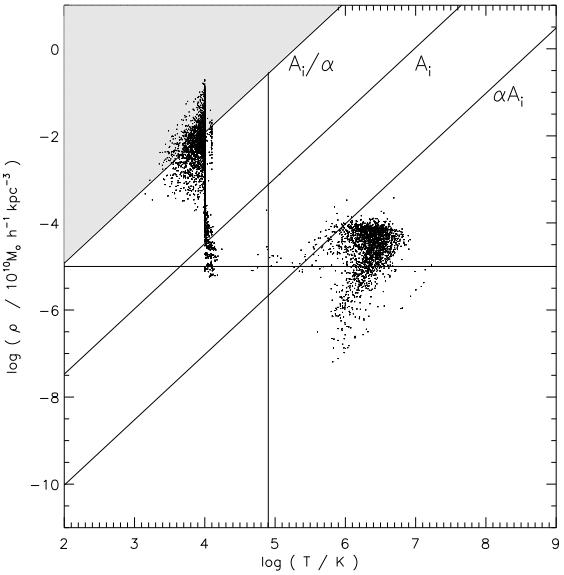


Figure 4.1: Temperature-density distribution of gas particles in D12, which corresponds to a collapsing $10^{12}\,h^{-1}\mathrm{M}_{\odot}$ mass system, run with our decoupling scheme, at $1\,h^{-1}$Gyr. The solid lines indicate curves of constant entropic function, as indicated. The shaded area corresponds to particles which are decoupled from a given particle with entropic function $A_i$.

run with our decoupling treatment (see next Section), after $1\,h^{-1}$Gyr of evolution. The solid lines indicate curves of constant entropic function. Note that there are two clear gaseous phases: a cold and dense one, and a diffuse, hot one. In this simulation which does not include SN energy feedback, the hot phase has been formed by the collapse and virialization of the system. This plot schematizes how our decoupling scheme works: a given particle $i$ with entropic function $A_i$ will decouple from all particles in the shaded area, which have entropic functions which are lower by a factor of $\alpha$.

In our code, we assume a fixed mass within the smoothing length, which is essentially equivalent to assume a fixed number of neighbours, except that the mass within the kernel volume is estimated based on the SPH density estimate itself. As discussed in Springel & Hernquist (2002), this allows an entropy conserving formulation of SPH. The mass we have typically chosen corresponds to 32 enclosed neighbours. The neighbour search always iterates until this desired number/mass of neighbours is reached. In practice, an iteration method based on a robust bisection scheme is used to determine the appropriate smoothing lengths and neighbour numbers. Should the number of neighbours suddenly change, the correct new smoothing

length is always found, regardless of how large the change is.

Conservation of energy and momentum requires symmetric force evaluations between all particle pairs to ensure the validity of Newton's third law. Hence, for the force calculation only we include the extra requirement that if particle $i$ excludes particle $j$ from its neighbour list, then particle $j$ does not consider particle $i$ as a neighbour either. In this way the symmetry of force calculations is preserved in our code.

An important advantage of the above scheme is that the decoupling criterion is checked on a pairwise basis. This allows a formulation which is independent of scale or resolution-dependent parameters. Only the dimensionless free parameter $\alpha$ needs to be set. A multiphase structure naturally appears in the gas component in this model once realistic cooling processes are included. This substantially improves the representation of the interstellar medium in star-forming galaxies.

### 4.1.2 TESTS OF THE MODEL

In order to test the performance of this decoupling scheme, we carried out a set of idealized simulations of the formation of isolated disk galaxies similar to those in the early work of Navarro & White (1993). The initial conditions are generated by radially perturbing a spherical grid of superposed dark matter and gas particles to produce a cloud with density profile $\rho(r) \sim r^{-1}$ and radius $100\,h^{-1}$kpc. This sphere is initially in solid body rotation with an angular momentum characterized by spin parameter $\lambda \simeq 0.1$. The initial thermal energy of the system is only 5% of its binding energy, i.e. the gas is cold. We have simulated a $10^{12}\,h^{-1}\mathrm{M}_{\odot}$ mass system, 10 per cent of which is in the form of baryons, and used $\sim 9000$ particles for the gas and $\sim 9000$ for the dark matter. This yields particle masses of $\sim 10^{8}\,h^{-1}\mathrm{M}_{\odot}$ for dark matter and $10^{7}\,h^{-1}\mathrm{M}_{\odot}$ for gas. We adopted gravitational softening lengths of 1.50 and 0.75 $h^{-1}$ kpc for dark matter and gas particles, respectively. In the tests presented in this section, we do not allow star formation, and the cooling assumed primordial element abundances.

We ran two simulations of the system described above, the only difference being the inclusion of our multiphase treatment. In the simulation including the multiphase model, we have adopted a decoupling parameter of $\alpha = 50$. In order to better highlight the effects of the multiphase model, we specify two reference phases, defined by $A \geq A_{\rm crit}$ for the "hot" component, and $A < A_{\rm crit}$ for the "cold" component, where $A_{\rm crit}$ is the entropic function corresponding to a temperature of $T = 2\,T_{*}$ K and a density of $\rho = 0.1\ \rho_{*}$. Here $T_{*} = 4 \times 10^{4}$ K and $\rho_{*} = 7 \times 10^{-26}$ g cm$^{-3}$ are the star formation thresholds introduced in Chapter 2. We stress that these definitions are not related to the decoupling model and are only introduced to facilitate presentation of our results. Note that our aim is to reliable separate 'cold and dense' and 'hot and diffuse' particles, for purposes of analysis. To accomplish

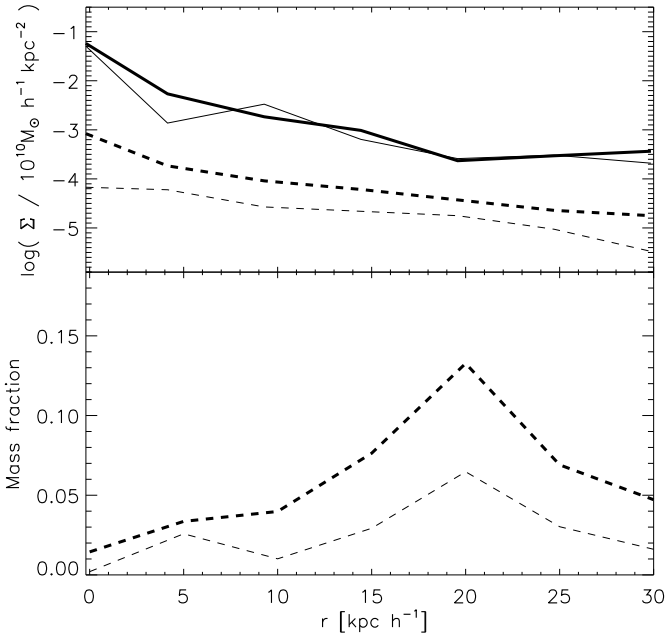


Figure 4.2: Top: Surface density profiles projected onto the disk plane after $0.9\,h^{-1}$Gyr for hot (dashed lines) and cold (solid lines) gas in our cooling-only simulations of isolated collapsing spheres carried out using a standard SPH implementation (thin lines) and using our decoupling scheme with $\alpha = 50$ (thick lines). Bottom: The fraction of baryonic mass belonging to the hot medium as a function of radius for the same two simulations. These plots are restricted to the disk plane with a vertical distance of $|z| < 2\,h^{-1}$kpc.

this, we have used the entropic function to better segregate gas phases in part of our analysis. As particles with similar entropies have similar cooling times, the entropic function is very useful to probe physical properties in the sense we are interested in this work (i.e. which particles will remain hot long enough to produce an impact on the dynamics of the systems).

In the upper panel of Fig. 4.2 we compare the surface gas density profiles, projected onto the disk plane, of the two simulations after $0.9\,h^{-1}$Gyr. Profiles for the "hot" and "cold" phases defined above are shown separately. In the lower panel we plot the fraction of baryonic mass which is "hot" as a function of radius. These plots have been made taking into account the gas within a vertical distance $|z| < 2\ h^{-1}$ kpc in order to restrict to the disk plane. The surface density profiles for the cold gas

(solid lines) are almost indistinguishable, but the amount of hot gas (dashed lines) is greater at all radii when phase decoupling is included. From the lower panel we can see that the hot medium has grown at the expense of the cold one. This is a result of the elimination by the decoupling algorithm of the excess cooling discussed above[1].

We have investigated the sensitivity of the decoupling scheme to the value of the free parameter $\alpha$ in Eqn. (4.2). Too small a value for $\alpha$ would lead to decoupling of gas particles with very similar properties, while too large a value would produce no effect at all. We ran tests varying the value of $\alpha$ over the range $\alpha = 5$ to $\alpha = 100$, and found that our results are insensitive to the actual value within this range. This reflects the large entropy difference between the various phases of a realistic ISM caused by the structure of the radiative cooling function. We will generally choose $\alpha = 50$ for later experiments in this paper.

## 4.2 ENERGY FEEDBACK BY SUPERNOVAE

### 4.2.1 MODEL DESCRIPTION

Our model for energy feedback by SNe resorts to an explicit segregation of the gas surrounding a star particle into a cold-dense phase and a diffuse phase, both for the release of SN energy and for the mixing of newly synthesized elements into the ISM. The separation into two phases, and the different treatment of them with respect to feedback, is motivated by previous attempts to model the release of SN energy, which have repeatedly found that this is ineffective if direct thermalization is invoked because the cold dense gas in which stars form has a very short cooling time (Katz 1992). In addition, the characteristic physical scales relevant to feedback in the real ISM are usually not resolved in galaxy formation simulations (Thacker & Couchman 2001).

Surrounding each star particle with exploding SNe we define two gaseous phases which we loosely denote *cold* and *hot*. The *cold* phase consists of gas with $T < 2\,T_*$ and $\rho > 0.1\rho_*$, while the rest of the gas is considered to be part of the *hot* phase, even though much of it may actually have $T < 2\,T_*$. These two phases are treated differently at the time of metal and energy distribution. The values of $\rho_*$ and $T_*$ ($7\times10^{-26}$ g cm$^{-3}$ and $4\times10^4$ K respectively) are typical of local star-forming regions and are assumed to be independent of the global properties of the systems. Note that these phases are not directly related to the decoupling scheme itself, or to the

[1]The entropy-conserving formulation of SPH (Springel & Hernquist 2002) implemented in GADGET-2 has solved the extreme problem of a near-absence of hot particles in the central regions found by Marri & White (2003) when carrying out a similar test using codes based on GADGET-1.

hot and cold gas components we used in the previous section to analyse some of our results.

Note that stars have two smoothing lengths. Both are adjusted to enclose the same mass (basically the mass corresponding to 32 neighbours). However, when calculating the smoothing length corresponding to the hot neighbours, it can happen that in order to enclose 32 neighbours we need an extremely large smoothing length (because there is no local hot environment, or only a very teneous one), so it becomes unphysical. In this case, we prefer to set a maximum length allowed to search for hot neighbours. We have used 10 times the smoothing length calculated for cold neighbours (note that stars are formed by definition in high density regions, and so there are always enough 'cold' neighbours). We have run simulations assuming different maximum lengths allowed ($\sim 10 - 100$ cold smoothing length), and we found that the results are not sensitive to this choice. Note that the neighbour searches for stars have no relation to the SPH treatment for the gas.

Conceptually, we can divide our discussion of the SN energy feedback model into two main stages: energy production and energy release. We shall discuss them in turn.

To describe energy production, we have included the energy contributions associated with SNII and SNIa explosions. Briefly, as described in Chapter 2, our scheme works as follows: at each integration time-step, we calculate the number of SNII by adopting an initial mass function (IMF) and by assuming that stars more massive than 8 $M_\odot$ end their lives as SNII after $\approx 10^6$ yr. For SNIa, we use the W7 model of Thielemann, Nomoto & Hashimoto (1993). In order to estimate the SNIa number, we adopt an observationally motivated relative rate with respect to SNII, and we assume a progenitor lifetime in the range $[0.1, 1]$ Gyr as described in Chapter 2. Finally, we assume that each SN injects $10^{51}$ ergs of energy into the surrounding gas.

In order to distribute the energy produced by a given star particle, we separately identify the gaseous neighbours that belong to the *hot* and to the *cold* phases. Smoothing lengths are calculated for the star particle so that the number of neighbours in each of these phases is similar to the number used in the SPH formalism to estimate hydrodynamical forces. Within each phase, gaseous neighbours then receive a fraction of the SN energy, weighted by the appropriate smoothing kernel.

We assume that a fraction $\epsilon_h$ of the SN energy is instantaneously thermalized and appears in the hot phase of the ISM around the star particle, while a fraction $\epsilon_r$ is directly radiated away by the cold phase. The remaining fraction of the energy, $\epsilon_c = 1 - \epsilon_h - \epsilon_r$, is injected into the cold gas causing some of it to join the hot phase. Because there is no consensus on the phenomenology of the ISM which could provide specific values for these fractions, we assume them to be independent of local conditions and we treat them as free parameters to be adjusted so as to reproduce the observations of star-forming systems. We vary their values widely

in order to analyse their impact on the dynamics of our model. Choosing $\epsilon_r = 1$ implies that all the SN energy is radiated away by the cold phase with no impact on the overall dynamics. Examples of the evolution in this extreme case are given by our multiphase-only runs (for example D12 in Table 1). For the sake of simplicity, we have chosen $\epsilon_r = 0$ in the rest of our tests, noting that a non-zero value could always be compensated by a different IMF or different assumed SN energies. In this case, the effects of feedback depend only on $\epsilon_h$ (or $\epsilon_c$). In practice, both $\epsilon_h$ and $\epsilon_r$ should be varied in order to get the best possible match to observation.

For each gas particle belonging to the cold phase, we define a *reservoir* in which the SN energy that the particle receives from successive SN explosions is accumulated. Once the accumulated energy ($E_{\rm res}$) is high enough to modify the thermodynamic properties of a cold gas particle in such a way that its new properties will resemble those of the hot phase, we *promote* the cold particle, dumping its reservoir energy into its internal energy. This *promotion scheme* has been developed in order to prevent artificial losses of the SN energy by the cold phase and to ensure that cold ISM gas can be entrained in outflows, producing *mass-loaded* galactic winds.

In order to decide whether the promotion of a given cold particle should take place, we consider the following physical conditions, (a) the final physical state we want the particle to reach, and (b) the energy needed for the process to take place, given its current physical state. Since we want to mimic the transformation of cold gas into gas that is in thermal equilibrium with the hot-gas surroundings, we require that the final state for a cold particle that is promoted should be similar to that of its local hot phase environment. Based on our decoupling scheme, the local hot phase of any given cold gas particle is naturally defined by those neighbours from which the cold particle is decoupled (see Section 4.1.1).

Assuming that the transformation from the cold to the hot phase takes place at constant pressure, we define a *promotion energy* for each particle. This promotion energy ($E_{\rm prom}$) takes into account the energy needed not only to raise the temperature of the particle to that of its hot neighbours, but also for it to expand against the ambient pressure to reach their mean density. Thus we require the promoted particle to have an entropic function at least as high as the mean of those of its hot neighbours ($A^{\rm hot}_{\rm Avg}$). The conditions for promotion are the following:

$$E_{\rm res} > E_{\rm prom} = \frac{\gamma}{\gamma - 1}\, m_i \Big[ A^{\rm hot}_{\rm Avg}\, (\rho^{\rm hot}_{\rm Avg})^{\gamma-1} - A_i\, \rho_i^{\gamma-1} \Big] \tag{4.5}$$

$$A_{\rm new} > A^{\rm hot}_{\rm Avg} \tag{4.6}$$

Here, $A_{\rm new}$ is an estimate of the new entropic function of the particle after promotion and $A^{\rm hot}_{\rm Avg}$ and $\rho^{\rm hot}_{\rm Avg}$ are the mean entropic function and mean density of the hot neighbours surrounding the cold gas particle, respectively. The value of $A_{\rm new}$ is calculated assuming that the energy of the particle after promotion will be its actual

energy plus the reservoir and that the new density will be the average density of the hot neighbours, $A^{\rm hot}_{\rm Avg}$.

Note that, in order to calculate the promotion energy, we consider a process at constant pressure. Hence, we need the energy to raise the particle's temperature but also we need to work against the background pressure. Expressed differently: $\mathrm{d}Q = \mathrm{d}U + p\mathrm{d}V$ with $p\mathrm{d}V = (\gamma - 1)dU$. In other words, we need the $c_P$ heat capacity for estimating the energy needed for our process to take place, which is $c_P = \gamma$ for an ideal monoatomic gas. This gives the relation in Eq. 4.5.

This scheme guarantees that once a gas particle is promoted, it will have thermodynamic properties matching those of its local hot environment. Consequently, it will remain hot at least as long as nearby hot material. The procedure also ensures that the smooth character of SPH is preserved and no 'flip-flop' instabilities are generated during promotion. Note that the promotion criterion is evaluated for each cold gas particle individually, and that it depends both on the particle's own thermodynamic properties and on those of its local hot environment. This scheme allows us to mimic the reheating of cold interstellar gas by SN explosions, providing a link between SN energy feedback and our multiphase treatment, and resulting in a self-regulated star-formation cycle.

We also include an extra requirement for promotion in order to treat cases where cold particles have few hot neighbours within the maximum smoothing length allowed, for example because all gas is cold. If this happens, we prefer to keep the particle in the cold phase until a well-defined hot environment has formed. This ensures numerical stability in cases where the hot phase does not exist or is very poorly sampled. We determine when a hot environment is well defined depending basically on the number of particles in the sample, and set a minimum number of hot particles. We have run simulations with different values and found that a minimum of 5 hot neighbours are needed to avoid instabilities and to get converged results. In the simulations analysed in this work, we have used a minimum of 5 hot neighbours.

In the case where a cold gas particle satisfies the conditions to be transformed into a star particle when still having a reservoir of energy, we distribute this energy to its cold-phase neighbours using the smoothing kernel. In the extreme case that there are no cold neighbours, the energy is assumed to be lost and the reservoir is reset to zero. Finally, a numerical artifact could also develop in our scheme when cold particles become "hot" by numerical noise (near the density and temperature thresholds segregating phases). In this case, some feedback energy could be lost since these particles would probably cool down again. This could happen because the new hot particle now behaves as any other hot particle, meaning that the reservoir energy will be immediately distributed to its neighbours, and the reservoir will be reset to zero. However, we have checked that the total reservoir energy for particles in this situation is a negligible fraction of the total energy produced by SN ($\sim 10^{-5}$) through the evolution of a galaxy.

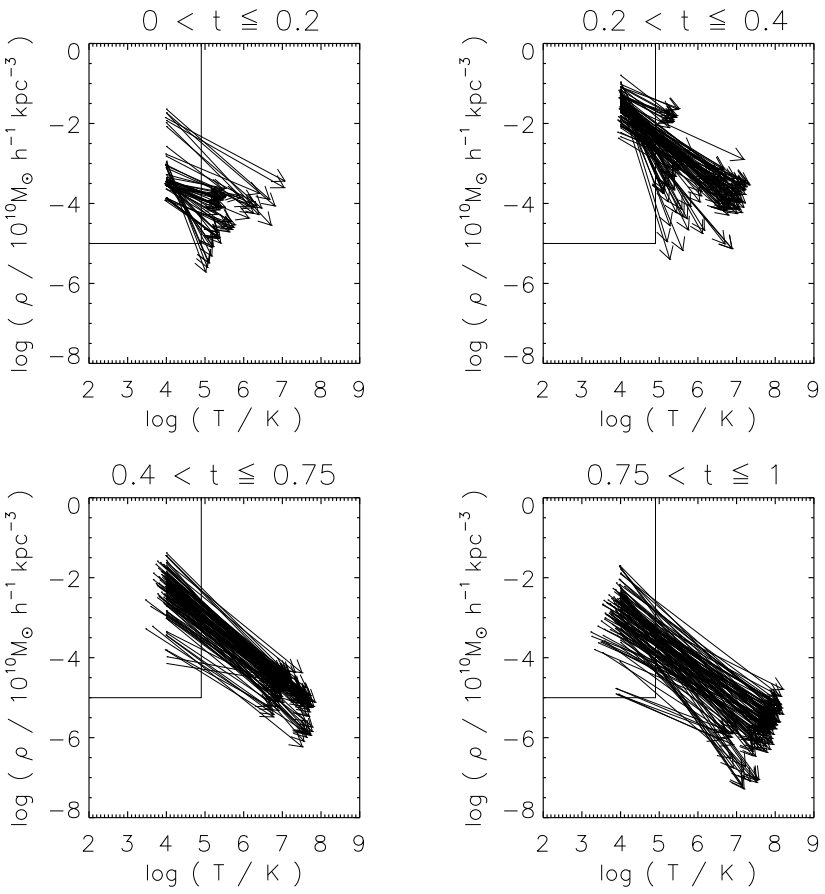


Figure 4.3: Temperature-density distribution of promoted particles in F12-0.5, which corresponds to a $10^{12}\,h^{-1}\mathrm{M}_{\odot}$ mass system, run with energy feedback and $\epsilon_c = 0.5$. The arrows point from the initial state before promotion to the final one after promotion. The solid lines separate the cold and hot phases of the feedback scheme. The different panels correspond to particles promoted in different time intervals, indicated in units of $h^{-1}$Gyr.

Note that the entropic function is the independent thermodynamic variable in our code which is integrated in time. One consequence of our implementations of decoupling and promotion is that the density of particles needs to be updated twice in our code, in each time step of integration. At both times, we need to perform neighbour searches where we compare the entropy of each particle with the entropy of its neighbours. And only the particles selected as neighbours according to our phase (de)coupling criteria are then used to estimate new densities. The first density update is done at the beginning of the time-step where we need to estimate the densities of particles, and hence the pressures, allowing the forces to be calculated, as usually implemented. The second density update is done after promotion takes place. When promotion occurs, the entropy of particles is changed, hence new density estimates are carried out which take the new entropies into account in the neighbour selection, letting the particles expand and change their densities consistently with the energy received by SNe.

Finally, we have also slightly modified the chemical enrichment model of Chapter 2 to work in a consistent fashion with our new treatment of the SN energy. To this end, we distribute the chemical elements into the hot and cold phases of a given star particle similarly to the energy distribution. For metal distribution we assume different fractions $\epsilon_c^m$ and $\epsilon_h^m$ so that $\epsilon_c^m + \epsilon_h^m = 1$. These fractions could, in principle, be tuned differently than the fractions for energy distribution in order to match observations. Our model assumes that the chemical distribution always occurs simultaneously with SN explosions, i.e. there is no metal reservoir corresponding to the promotion scheme described above. Clearly, it would be possible to choose different fractions for distributing heavy elements than for distributing energy but, at this stage, we prefer to avoid additional parameters by assuming the metal fractions to be equal to the energy fractions in all experiments analysed in this paper.

### 4.2.2 TESTS OF THE MODEL

As a first test of the dynamics of our numerical scheme, we have run a set of simulations of the evolution of the idealized initial conditions described in Section 4.1.1. These experiments include metal-dependent radiative cooling, star formation, chemical enrichment and energy feedback. They have all been run with the same star formation and chemical input parameters: a star formation efficiency $c = 0.1$, a Salpeter IMF with lower and upper mass cut-offs of 0.1 and 40 $M_\odot$ respectively, a SNIa rate of 0.3 relative to SNII which is a typical value coming from observations in Sa-Sb galaxies (as used in Chapter 2), and a life-time interval of $[0.1, 1]$ Gyr for SNIa (see Chapter 2 for details). We have assumed an instantaneous recycling approximation for SNII. We have used metal-dependent cooling functions adapted from Sutherland & Dopita (1993) as described in Chapter 2, and assume no cooling for gas particles with temperature lower than $10^4$ K. The decoupling scheme has

Table 4.1: Main properties of our simulations of idealized protogalaxy collapses. The columns give total mass, initial number of gas and dark matter particles, and the feedback input parameter ($\epsilon_c$).

| Test | $M_{\rm vir}$ $[h^{-1}{\rm M}_\odot]$ | $N_{\rm gas} = N_{\rm dark}$ | $\epsilon_c$ |
|---|---|---|---|
| D12 | $10^{12}$ | 9000 | - |
| F12-0.5 | $10^{12}$ | 9000 | 0.5 |
| F12-0.5-H | $10^{12}$ | 40000 | 0.5 |
| F10-0.5 | $10^{10}$ | 9000 | 0.5 |
| F10-0.5-H | $10^{10}$ | 40000 | 0.5 |
| F9-0.5 | $10^{9}$ | 9000 | 0.5 |
| F9-0.5-H | $10^{9}$ | 40000 | 0.5 |

been turned on for all the experiments with a decoupling parameter of $\alpha = 50$. We have used gravitational softening lengths of 1.50, 0.75 and $1.13\,h^{-1}$kpc for dark matter, gas and star particles, respectively.

We here analyse simulations of systems of different mass, run with feedback parameter $\epsilon_c = 0.5$. For comparison, we have computed corresponding reference simulations without SN feedback in all cases. Three higher resolution simulations have also been done to test numerical convergence. For the different total masses, the softening lengths as well as the initial radii have been scaled in proportion to $M^{1/3}$, relative to the parameters assumed for the $10^{12}\,h^{-1}{\rm M}_\odot$ system, leading to identical collapse times and characteristic densities for all systems. The main properties of these simulations are summarized in Table 4.1.

In order to assess how the energy feedback model and the promotion scheme work, we show in Fig. 4.3 the effects of promotion on individual particles. As explained earlier, each cold gas particle has been assigned a reservoir in which we keep track of the energy it receives from nearby SN explosions. This reservoir energy is accumulated until the particle is eventually promoted, dumping its reservoir into its internal energy. In Fig. 4.3, we plot the properties of promoted particles in a density-temperature plot for our test F12-0.5. The arrows point from the original location of each cold gas particle to its new position after promotion, and the different panels correspond to particles promoted in different time intervals. It is clear that our feedback model is successful in driving a gas flow from the cold, dense phase into the hot, diffuse medium where the promoted particles share the properties of their local hot environment. Note that the hot environment evolves with time, and consequently, the new location of promoted particles on the temperature-density plot

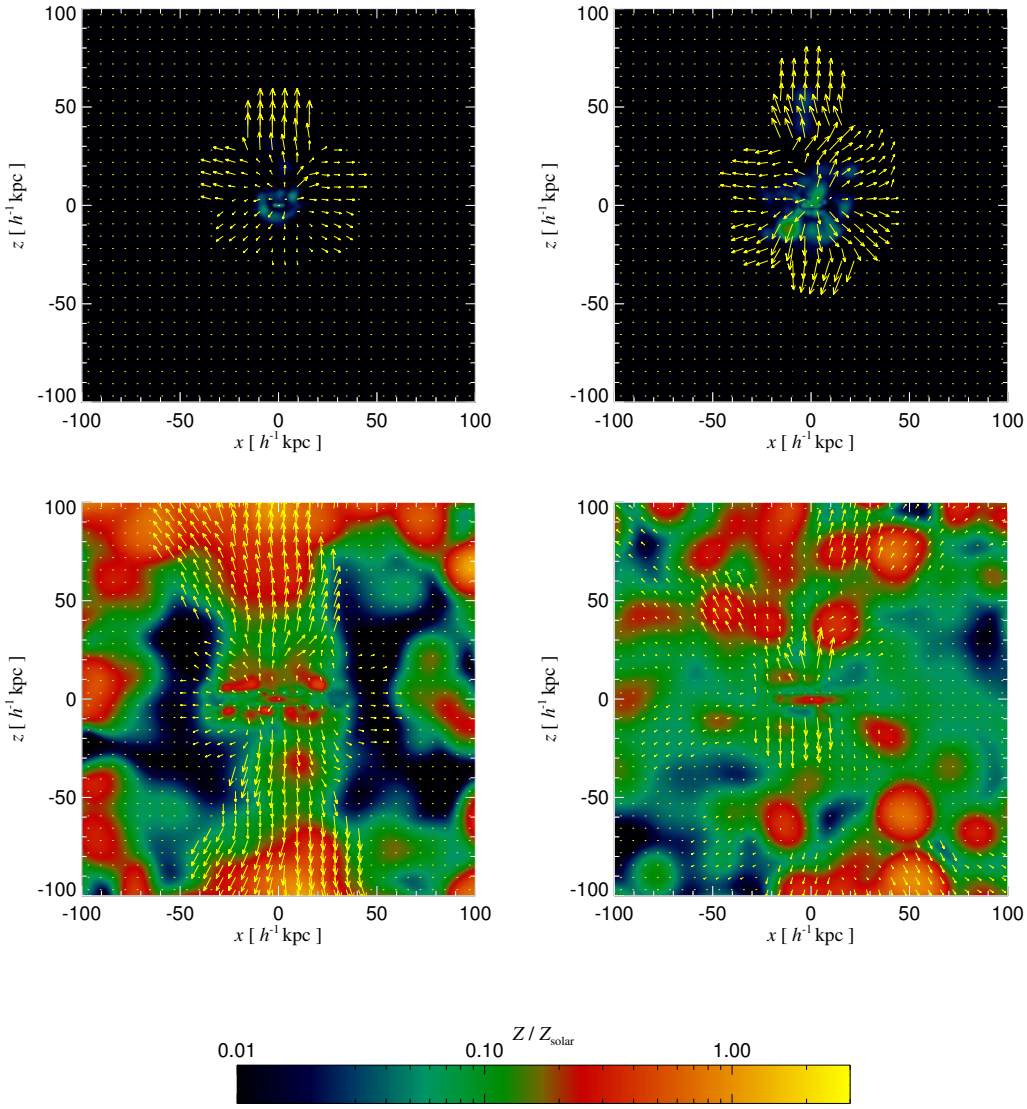


Figure 4.4: Projected velocity field of recently promoted particles (i.e. particles promoted in the last 0.2 $h^{-1}$ Gyr, arrows) for our simulation F12-0.5 with supernova feedback with $\epsilon_c = \epsilon_h = 0.5$. The different panels correspond to different times in the evolution of the system: $t = 0.3$ (upper left panel), 0.4 (upper right panel), 0.75 (lower left panel) and $1.0\,h^{-1}$Gyr. The lengths of the arrows scale with the magnitude of the local velocity, with the longest arrows corresponding to $\sim 1000\,\mathrm{km\,s^{-1}}$. The colour map in the background encodes the projected metallicity field, according to the colour-scale shown at the bottom.

changes accordingly. This flexibility arises because we do not prescribe in advance the thermodynamic properties of the hot and cold phases.

A further consequence of the reheating of cold gas and its promotion into the hot phase is the generation of a significant outflow of material from the system. As an illustrative example, we show in Fig. 4.4 an edge-on projection of the velocity field of promoted particles (arrows) in F12-0.5. Different panels correspond to different times during the evolution of the system: $t = 0.3$ (upper left panel), 0.4 (upper right panel), 0.75 (lower left panel) and $t = 1.0\,h^{-1}$Gyr (lower right panel). In each panel, the velocity field has been calculated using particles promoted in the last $0.2\,h^{-1}$ Gyr. The lengths of the arrows scale with the magnitude of the local velocity, with the longest arrows corresponding to $\sim 1000\,\mathrm{km\,s^{-1}}$. The background colour represents the projected metallicity for the total gas component. From this figure we can see that our promotion scheme establishes an effective mechanism for transporting gas from the centre of the disks into the haloes. Once particles are promoted, they are accelerated outwards, moving mainly in the direction perpendicular to the disk plane. As may be seen from this figure, the outflow is not completely symmetric, since it is determined by the local geometry of the gas and the stellar distribution. Note that the inclusion of energy feedback allows us to account for chemical enrichment of the region outside the disks since the galactic outflows are able to transport a significant fraction of the heavy elements (chemical elements higher than hydrogen and helium) outwards. We will come back to the impact of SN energy feedback on the chemical properties of galaxies in the next Chapter.

The exchange of mass between the cold and hot phases driven by our promotion scheme strongly affects the evolution of the systems and their resulting mass distributions. In Fig. 4.5, we show face-on projections of the disks in D12 (no energy feedback; upper panels) and F12-0.5 (with energy feedback; lower panels) at $t = 1.2\,h^{-1}$Gyr. We show the hot and cold media defined in section 2.1 separately, as well as the stellar component. We can see from this figure that energy feedback helps to generate a well defined hot phase which is distributed out to $\sim 300\,h^{-1}$kpc in this particular experiment. In the case of no energy feedback (upper panels) the hot phase is produced only by the collapse and virialization of the system, is a small fraction of the gaseous mass, and remains bound within $\sim 100\,h^{-1}$kpc. In this latter case, most of the gas has been able to cool and condense, producing a large stellar clump in the centre.

We have also tested how numerical resolution affects the evolution of systems of different total mass. For this purpose we ran three additional simulations increasing the initial number of gas and dark matter particles up to 40000 in each mass component (see Table 4.1). These tests were performed for systems with total masses of $10^9$, $10^{10}$ and $10^{12}\,h^{-1}\mathrm{M}_\odot$ (F12-0.5-H, F10-0.5-H, F9-0.5-H), respectively, using a feedback parameter of $\epsilon_c = 0.5$ in all cases. In Fig. 4.6, we show the evolution of the star formation rate for these models and compare them with their lower resolu-

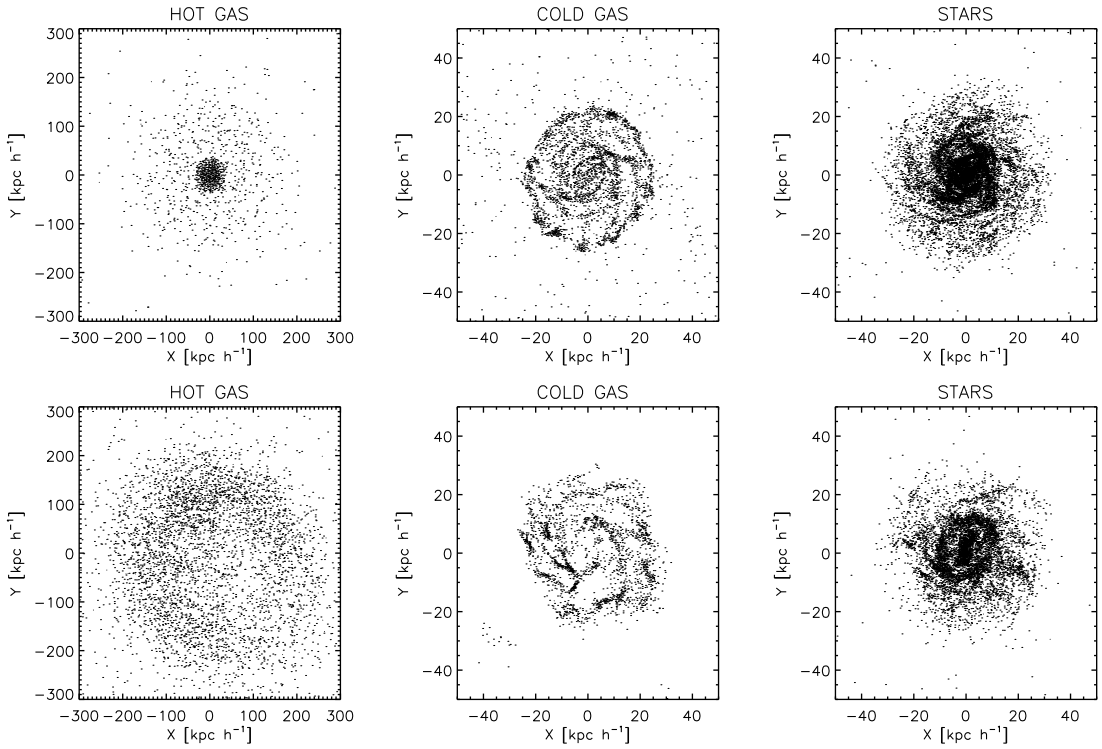


Figure 4.5: Face-on projections of the disks in $10^{12}\,h^{-1}\mathrm{M}_{\odot}$ systems after $1.2\,h^{-1}$Gyr of evolution. We show the hot gas ($A \geq A_{\rm crit}$), the cold gas ($A < A_{\rm crit}$) and the stars separately, both for D12 (no energy feedback; upper panels) and for F12-0.5 (SN feedback with $\epsilon_c = \epsilon_h = 0.5$; lower panels).

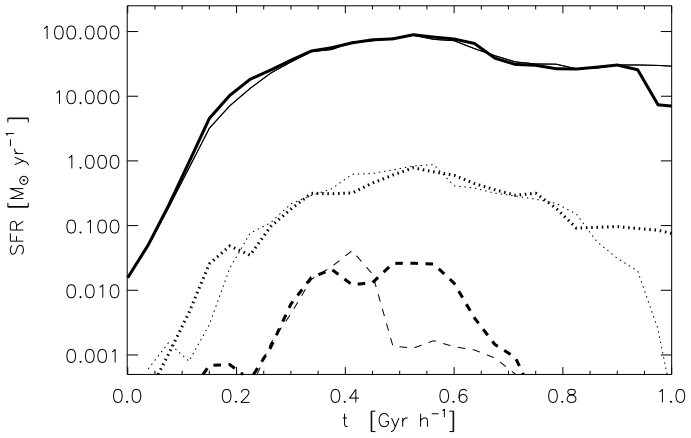


Figure 4.6: Star formation rates for F12-0.5 (solid thin line), F12-0.5-H (solid thick line), F10-0.5 (dotted thin line), F10-0.5-H (dotted thick line), F9-0.5 (dashed thin line) and F9-0.5-H (dashed thick line), corresponding to idealized protogalactic collapses of differing total mass and numerical resolution.

tion counterparts. From this figure we can see that the results are reasonably well converged for the higher halo masses. For the smallest system, stochastic bursting behaviour is observed so convergence is difficult to test.

The tests of this section confirm that our new model can produce the main phenomenology linked to SN feedback, in relation to the regulation of the star formation activity and the triggering of outflows which transport material into the outer regions of galaxies. In the next Chapter, we will use our test simulations in order to analyse the effects of our new feedback scheme on systems of different mass in relation to the star formation process. We will also assess the dependence of our results on the adopted feedback parameters, and investigate the impact of the energy feedback on the resulting metal distributions.

# Chapter 5

# Regulation of the Star formation and galactic winds

In Chapter 4 we have described a new scheme to treat a multiphase interstellar medium in SPH simulations of galaxy formation. This scheme can represent a co-spatial mixture of cold and hot ISM components, and is formulated without scale-dependent parameters. It is thus particularly suited to studies of cosmological structure formation where galaxies with a wide range of masses form simultaneously. We have also presented new algorithms for energy and heavy element injection by supernovae, and show that together these schemes can reproduce several important observed effects in galaxy evolution.

In this Chapter, we use idealized collapse simulations similar to those used in Chapter 4, and discuss the impact of SN feedback on galaxy formation. We include an analysis of the effects on star formation and the generation of winds (Section 5.1), on chemical enrichment of the ISM and the IGM (Section 5.2), and within galaxies of differing total mass (Section 5.3). In Section 5.4 we analyse both such collapse simulations and simulations of equilibrium galaxies similar to the Milky Way, exploring whether a suitable choice of star formation efficiency allows us to reproduce the observed Kennicutt relation between the surface densities of gas and of star formation in galaxies.

## 5.1 Star formation and outflows

We use our idealized collapse models in order to analyse several important properties related to SN energy feedback. As it was explained in Chapter 4, the initial conditions are generated by radially perturbing a spherical grid of superposed dark matter and gas particles to produce a cloud with density profile $\rho(r) \sim r^{-1}$ and radius $100\,h^{-1}$kpc. This sphere is initially in solid body rotation with an angular momentum characterized by spin parameter $\lambda \simeq 0.1$. The initial thermal energy of the system is only 5% of its binding energy, i.e. the gas is cold. We have simulated

a $10^{12}\,h^{-1}\mathrm{M}_{\odot}$ mass system, 10 per cent of which is in the form of baryons, and used $\sim 9000$ particles for the gas and $\sim 9000$ for the dark matter. This yields particle masses of $\sim 10^{8}\,h^{-1}\mathrm{M}_{\odot}$ for dark matter and $10^{7}\,h^{-1}\mathrm{M}_{\odot}$ for gas. We adopted gravitational softening lengths of 1.50 and 0.75 $h^{-1}$ kpc for dark matter and gas particles, respectively.

We have run simulations of different total masses. For these tests, the softening lengths as well as the initial radii have been scaled in proportion to $M^{1/3}$, relative to the parameters assumed for the $10^{12}\,h^{-1}\mathrm{M}_{\odot}$ system described above, leading to identical collapse times and characteristic densities for all systems.

In order to assess the response of galaxies to the adopted feedback parameters, we compare simulations F12-0.1, F12-0.5 and F12-0.9 (see Table 5.1) which only differ in the adopted value of $\epsilon_c$. For this analysis, we use the segregation of gas particles into cold and hot phases, as defined in the previous Chapter. In Fig. 5.1, we show the evolution of the cold ($A < A_{\rm crit}$, upper panel) and hot ($A \geq A_{\rm crit}$, middle panel) gaseous mass, in units of the total baryonic mass. For comparison, we also include the corresponding relations for simulation D12 which was run without energy feedback.

We have also estimated the fraction of unbound gas (lower panel), defining it here as the gas with a positive sum of kinetic and gravitational potential energy. As can be seen from this figure, the simulations with energy feedback have larger fractions of hot and unbound gas compared with their counterpart D12, indicating that the gas has been both heated and accelerated outwards. Note, however, that the effect of varying the input parameter $\epsilon_c$ is not simple. This is a consequence of the non-trivial interplay between release of supernova energy, promotion from cold to hot gas, and radiative cooling. All these processes influence the gas accretion and star formation rates and the formation of the cold and hot phases. As reference values we give in Table 5.1 the unbound gas fraction for all test simulations after $1.0\,h^{-1}$Gyr of evolution.

As a consequence of the exchange of material between the phases, our scheme can effectively regulate star-formation activity. This can be appreciated from Fig. 5.2 where we show star-formation rate and integrated stellar mass fraction as a function of time for our simulation series. Note that for the initial conditions adopted here, particles initially located at the edge of the system fall to the centre at $t \approx 0.55\,h^{-1}$Gyr. Compared to D12, supernova feedback reduces the final stellar mass by $\sim 45$, 40 and 65 per cent for F12-0.1, F12-0.5 and F12-0.9, respectively (see also Table 5.1). The larger $\epsilon_c$, the more energy injected into the cold phase, the sooner promotion becomes significant, leading to a reduction in the amount of cold gas and the suppression of star formation. On the other hand, as $\epsilon_c$ increases, less energy is dumped into the hot phase, making it easier both for hot gas to cool onto the disc and for cold gas to be promoted. The interplay between these processes leads to a non-monotonic dependence of the overall star-formation efficiency on $\epsilon_c$.

Table 5.1: Main properties of our simulations of idealized protogalaxy collapses: total mass (in units of $[h^{-1}\mathrm{M}_{\odot}]$), initial number of gas and dark matter particles, feedback input parameter ($\epsilon_c$), final stellar mass fraction, fraction of unbound baryons, fraction of metals locked into the hot gas, and fraction of metals locked into stars at $t = 1.0\,h^{-1}$Gyr.

| Test | $M_{\rm vir}$ | $N_{\rm gas} = N_{\rm dark}$ | $\epsilon_c$ | $M_{\rm star}/M_{\rm bar}$ | $M_{\rm unbound}/M_{\rm bar}$ | $f_{\rm met}^{\rm hot}$ | $f_{\rm met}^{\rm stars}$ |
|---|---|---|---|---|---|---|---|
| D12 | $10^{12}$ | 9000 | - | 0.581 | 0.025 | 0.002 | 0.557 |
| F12-0.1 | $10^{12}$ | 9000 | 0.1 | 0.324 | 0.411 | 0.910 | 0.045 |
| F12-0.5 | $10^{12}$ | 9000 | 0.5 | 0.362 | 0.309 | 0.556 | 0.212 |
| F12-0.9 | $10^{12}$ | 9000 | 0.9 | 0.231 | 0.315 | 0.710 | 0.188 |
| D11.5 | $10^{11.5}$ | 9000 | - | 0.738 | 0.002 | 0.000 | 0.663 |
| F11.5-0.1 | $10^{11.5}$ | 9000 | 0.1 | 0.415 | 0.361 | 0.903 | 0.050 |
| F11.5-0.5 | $10^{11.5}$ | 9000 | 0.5 | 0.390 | 0.441 | 0.755 | 0.170 |
| F11.5-0.9 | $10^{11.5}$ | 9000 | 0.9 | 0.276 | 0.613 | 0.793 | 0.152 |
| D11 | $10^{11}$ | 9000 | - | 0.824 | 0.000 | 0.000 | 0.703 |
| F11-0.1 | $10^{11}$ | 9000 | 0.1 | 0.398 | 0.364 | 0.904 | 0.044 |
| F11-0.5 | $10^{11}$ | 9000 | 0.5 | 0.403 | 0.407 | 0.694 | 0.169 |
| F11-0.9 | $10^{11}$ | 9000 | 0.9 | 0.273 | 0.666 | 0.813 | 0.146 |
| D10.5 | $10^{10.5}$ | 9000 | - | 0.712 | 0.000 | 0.000 | 0.608 |
| F10.5-0.1 | $10^{10.5}$ | 9000 | 0.1 | 0.342 | 0.416 | 0.903 | 0.043 |
| F10.5-0.5 | $10^{10.5}$ | 9000 | 0.5 | 0.318 | 0.525 | 0.780 | 0.141 |
| F10.5-0.9 | $10^{10.5}$ | 9000 | 0.9 | 0.207 | 0.779 | 0.881 | 0.119 |
| D10 | $10^{10}$ | 9000 | - | 0.520 | 0.000 | 0.000 | 0.426 |
| F10-0.1 | $10^{10}$ | 9000 | 0.1 | 0.271 | 0.501 | 0.911 | 0.031 |
| F10-0.5 | $10^{10}$ | 9000 | 0.5 | 0.258 | 0.633 | 0.848 | 0.107 |
| F10-0.9 | $10^{10}$ | 9000 | 0.9 | 0.174 | 0.819 | 0.901 | 0.085 |
| D9.5 | $10^{9.5}$ | 9000 | - | 0.451 | 0.000 | 0.000 | 0.405 |
| F9.5-0.1 | $10^{9.5}$ | 9000 | 0.1 | 0.155 | 0.548 | 0.913 | 0.017 |
| F9.5-0.5 | $10^{9.5}$ | 9000 | 0.5 | 0.184 | 0.821 | 0.899 | 0.101 |
| F9.5-0.1 | $10^{9.5}$ | 9000 | 0.9 | 0.113 | 0.902 | 0.945 | 0.051 |
| D9 | $10^{9}$ | 9000 | - | 0.373 | 0.004 | 0.000 | 0.382 |
| F9-0.1 | $10^{9}$ | 9000 | 0.1 | 0.107 | 0.596 | 0.912 | 0.011 |
| F9-0.5 | $10^{9}$ | 9000 | 0.5 | 0.041 | 0.662 | 0.840 | 0.031 |
| F9-0.9 | $10^{9}$ | 9000 | 0.9 | 0.069 | 0.927 | 0.950 | 0.044 |
| F12-0.5-H | $10^{12}$ | 40000 | 0.5 | 0.365 | 0.386 | 0.735 | 0.204 |
| F10-0.5-H | $10^{10}$ | 40000 | 0.5 | 0.240 | 0.326 | 0.782 | 0.095 |
| F9-0.5-H | $10^{9}$ | 40000 | 0.5 | 0.061 | 0.924 | 0.954 | 0.036 |

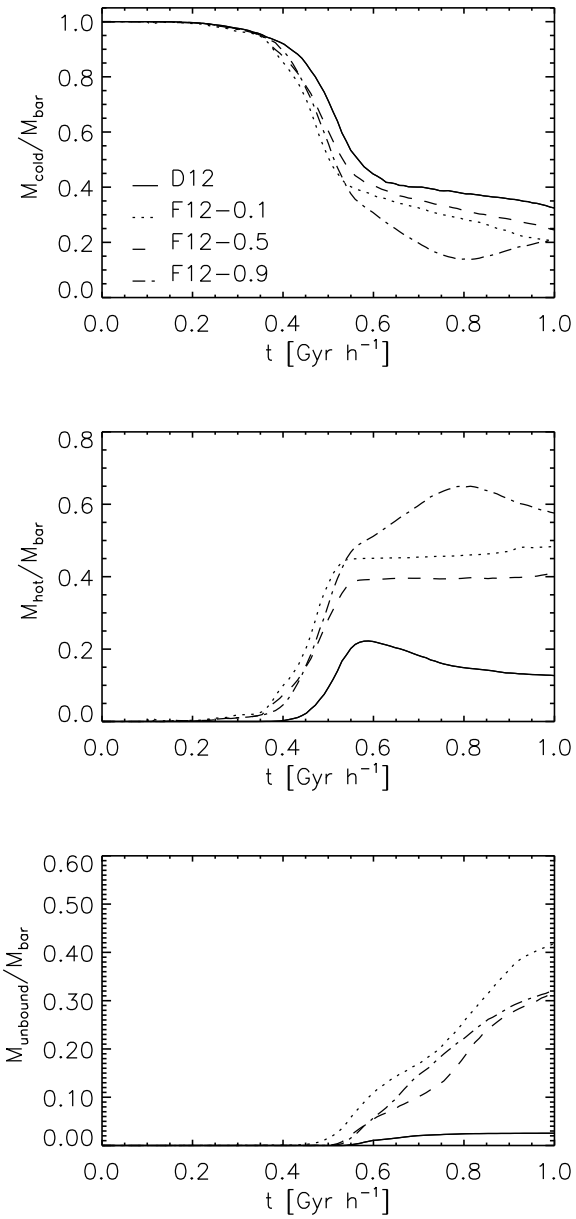


Figure 5.1: Evolution of the mass fraction in cold gas ($A < A_{\rm crit}$), hot gas ($A \geq A_{\rm crit}$) and unbound gas, normalized to the total baryonic mass of the system for simulations D12 (no energy feedback) and F12-0.1, F12-0.5 and F12-0.9 (with energy feedback but with different $\epsilon_c$ values).

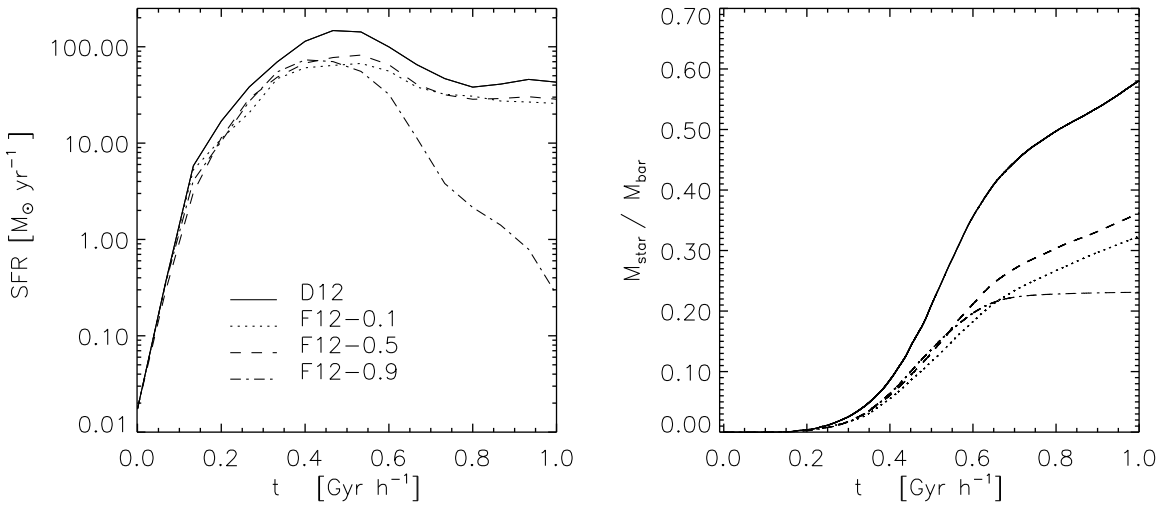


Figure 5.2: Evolution of the star formation rate (left panel) and integrated stellar mass fraction (right panel) for D12 (no energy feedback), and F12-0.1, F12-0.5 and F12-0.9 (supernova energy feedback with different values of $\epsilon_c$).

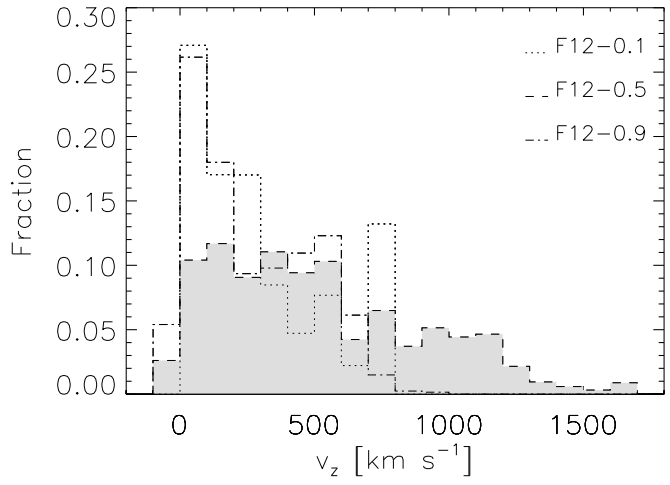


Figure 5.3: Fraction of promoted gas mass as a function of $z$-velocity, defined here as positive if particles are flowing away from the centre and negative otherwise. The plot shows results for our simulations of the $10^{12}\,h^{-1}\mathrm{M}_{\odot}$ system, run with different feedback parameters: F12-0.1 (dotted lines), F12-0.5 (dashed lines) and F12-0.9 (dotted-dashed lines), at time $t = 0.8\,h^{-1}$Gyr of the evolution.

Since in these tests promoted particles define the outflows, we show in Fig. 5.3 the mass-fraction in promoted gas as a function of $z$-velocity $v_z$, defined as positive if particles are moving away from the centre and negative otherwise. Results are given for F12-0.1, F12-0.5 and F12-0.9 after $0.8\,h^{-1}$Gyr of evolution (just after the maximum in star formation activity). Observationally, the velocities associated with galactic outflows are found to vary from a few hundred to thousands of kilometres per second (e.g., Lehnert & Heckman 1995, 1996). Here, we do not intend to make a detailed comparison with observation but we investigate the typical $z$-velocities that the gas components associated with outflows may reach in our model. For our test without SN energy feedback (D12), we calculated that 89 per cent of the gaseous mass has $|v_z| < 100\,\mathrm{km\,s^{-1}}$, with an upper limit of $|v_z| \approx 500$ km s$^{-1}$. In contrast, as may be seen in Fig. 5.3, in our simulations with feedback the fraction of *promoted* gas with $v_z > 500$ km s$^{-1}$ varies from 22 to 64 per cent. Clearly our scheme can produce outflows with relatively high velocities; the upper limits have increased to $v_z > 1000\,\mathrm{km\,s^{-1}}$. We can also infer from this figure that the fraction of promoted gas which flows back into the system (indicated by negative velocities) is small.

## 5.2 METAL DISTRIBUTION

The redistribution of the gas owing to the injection of energy by supernovae also affects the chemical abundances of the cold and hot gas and those of the stars. It is thought that SN feedback could be the mechanism responsible for the transport of heavy elements into the intergalactic medium. In order to study this process in detail, it would be necessary to simulate galaxies in their correct cosmological setting, which goes beyond the scope of this paper. As a first step, we can however investigate the potential effects of our feedback model on the metal distribution using our idealized simulations of protogalactic collapses of total mass $10^{12}\,h^{-1}\mathrm{M}_\odot$ (see Table 5.1).

In Fig. 5.4 (left panels), we show the evolution of the fraction of metals locked into cold gas ($A < A_{\rm crit}$), hot gas ($A \geq A_{\rm crit}$) and stars, normalized to the final total mass in heavy elements, for D12, F12-0.1, F12-0.5, and F12-0.9. In the right panels of Fig. 5.4, we also display the mean metallicity $Z$, in units of solar metallicity, for these same simulations. Note that the total mass in metals in the system is a function of time owing to ongoing star formation. From this figure we can see that if energy feedback is not included, the metal content remains completely locked into the stellar and cold gas components. This is expected, since there is no efficient mechanism to transport metals away from the star-forming ISM. This situation is radically changed by the powerful winds generated by the SN feedback scheme. These outflows redistribute the metals, increasing the amount of enriched hot gas at the expense of the cold gas and stars. Note that even in F12-0.9, for which only

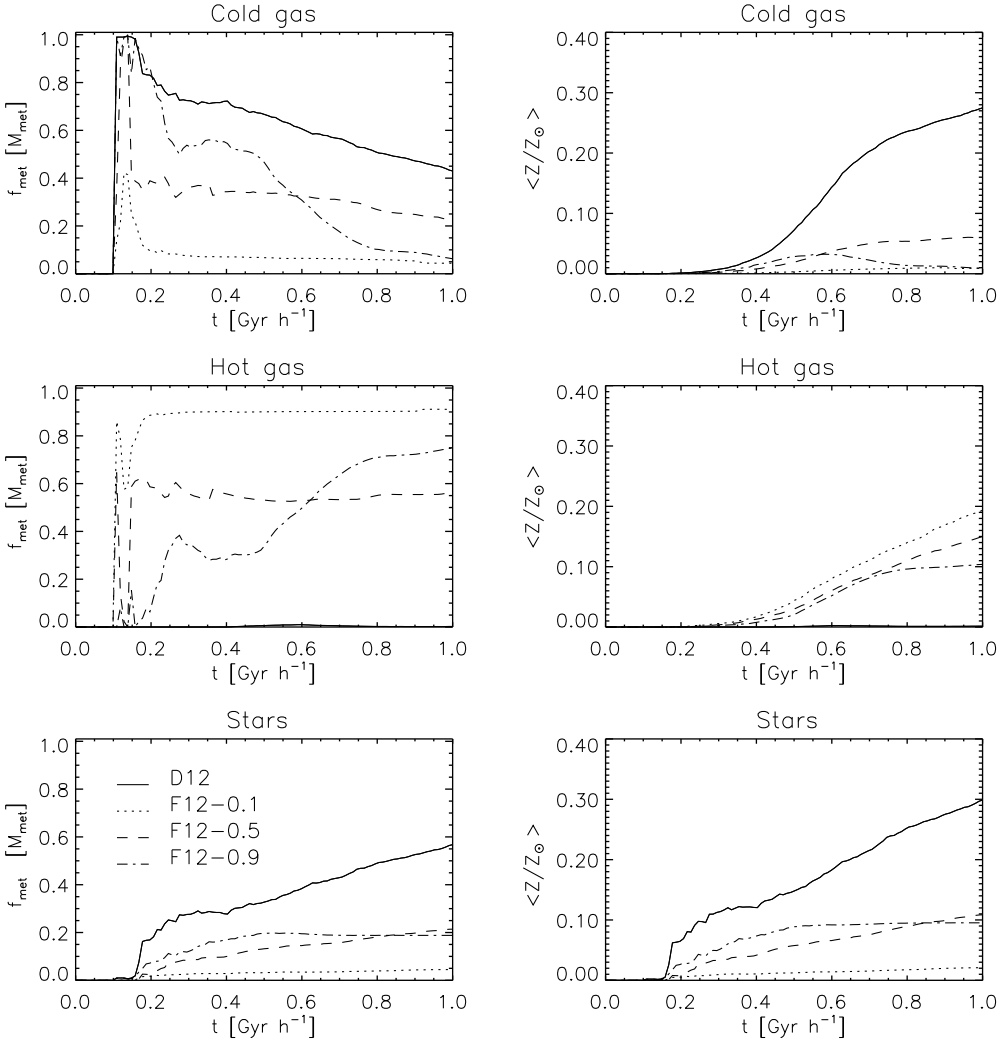


Figure 5.4: Evolution of the fraction of metals in the cold gas ($A < A_{\rm crit}$), hot gas ($A \geq A_{\rm crit}$) and in the stars (left panels), for our $10^{12}\,h^{-1}{\rm M}_{\odot}$ mass system. We show results for simulation D12 without energy feedback, and for simulations F12-0.1, F12-0.5 and F12-0.9 corresponding to different feedback parameters. We also show the evolution of the mean metallicity for the same runs (right panels).

10 per cent of the metals are directly injected into the hot phase, the dynamical and thermal evolution of the system differs markedly from the case without energy feedback, showing efficient enrichment of the hot gas. This is driven by promoted material which was enriched while cold. In the case of F12-0.1, the cold gas and the stars end up with a negligible fraction of the metals. These trends are also reflected in the mean metallicities of the gaseous and stellar components. Fine-tuning $\epsilon_c$ and $\epsilon_r$ in a simulation with self-consistent cosmological initial conditions may allow one to reproduce the observed metallicity trends for hot gas, cold gas and stars. We will attempt this for a Milky Way look-alike in a forthcoming paper.

## 5.3 DEPENDENCE ON VIRIAL MASS

From a theoretical point of view, supernova feedback is expected to play a crucial role in regulating the star formation activity in galaxies and in determining the level of enrichment of different environments. It is also expected that the impact of supernova feedback should depend strongly on virial mass, where smaller mass systems should be more strongly affected, their shallower gravitational potential wells making it easier for the supernovae to drive outflows (Larson 1976; White & Rees 1978; Dekel & Silk 1986). This concept has been widely applied in semi-analytic models of galaxy formation to explain several basic observational properties of the galaxy population such as the faint-end slope of the luminosity function (e.g. White & Frenk 1991). In previous sections we have demonstrated that our energy feedback model is able to produce gas outflows which lead to different levels of enrichment, depending on the adopted $\epsilon_c$ value. In this section, we discuss the effects of SN energy feedback as a function of the mass of the systems considered.

We again start from our idealized spherical initial conditions for protogalactic collapse. These initial conditions are simple enough to highlight the effects of feedback without being distracted by additional processes such as mergers and infall, which complicate the picture in fully hierarchical scenarios for galaxy formation. We analyse results from simulations that cover the total mass range $10^9 - 10^{12}\,h^{-1}\mathrm{M}_\odot$, as well as different choices of the feedback parameters (see Table 5.1). For comparison, we have also analysed simulations without feedback.

Fig. 5.5 compares star formation histories for systems of differing total mass, in each case for simulations without SN energy feedback (solid lines) and with the feedback model enabled, using $\epsilon_c = 0.1$ (dotted lines), $\epsilon_c = 0.5$ (dashed lines) and $\epsilon_c = 0.9$ (dashed-dotted lines). Note that all panels extend over the same y-range to facilitate direct comparison between the behaviour for the different mass systems. Clearly, SN feedback has a strong impact on these systems regardless of their total mass. For larger masses, the primary effect of SN feedback is a decrease in star formation activity. As one moves to lower mass systems, supernova feedback

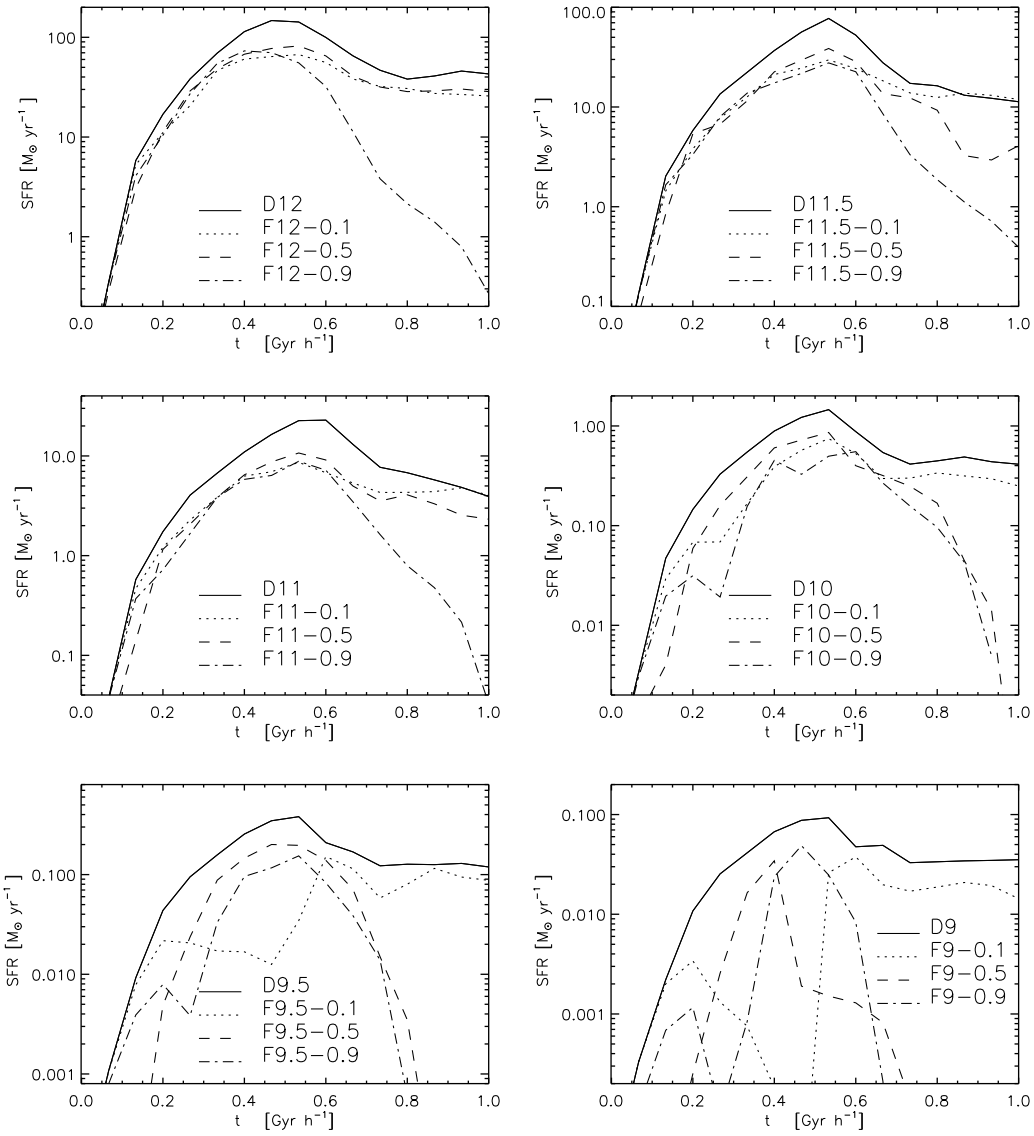


Figure 5.5: Star formation rates for simulations with total masses of $10^9$, $10^{9.5}$, $10^{10}$, $10^{11.5}$, and $10^{12}\,h^{-1}\mathrm{M}_\odot$. The plots give results both for simulations without supernova feedback (solid lines), and for simulations with SN feedback with $\epsilon_c = 0.1$ (dotted lines), $\epsilon_c = 0.5$ (dashed lines) and $\epsilon_c = 0.9$ (dashed-dotted lines). For comparison, all panels extend the same y-range.

modifies the star formation rates not only by decreasing the overall level of activity, but also by changing their character, producing a series of starbursts. From Fig. 5.5 we can also infer that increasing the value of $\epsilon_c$ generally leads to stronger feedback effects at all times. In particular, larger $\epsilon_c$ values are able to trigger several starburst episodes and to produce a significant decrease in the star formation activity at later times. Note that, specially for the smallest galaxies, star formation can stop completely after $\sim 1\ h^{-1}$ Gyr because the systems can lose their gas reservoirs. However, if more realistic initial conditions were considered, gas accretion from the intergalactic medium could contribute to fuel new star formation activity at later times.

In Fig. 5.6, we show the fraction of unbound gas as a function of virial mass after $0.85\,h^{-1}$Gyr of evolution, for simulations with $\epsilon_c = 0.1$ (dotted line), $\epsilon_c = 0.5$ (dashed line) and $\epsilon_c = 0.9$ (dashed-dotted line). We also show the results for our higher resolution simulations with $\epsilon_c = 0.5$ (squared asterisks). As discussed earlier, the unbound gas fraction can be viewed as a proxy for feedback strength since it quantifies the fraction of baryons that are swept away from the system as a result of a feedback-driven outflows. For a given total mass, as the value of $\epsilon_c$ is increased, the fraction of unbound gas increases. If no feedback is included, the fraction of unbound gas is negligible. As expected, for a given value of $\epsilon_c$, SN feedback has stronger effects as we go to smaller systems. The smaller the system, the larger the fraction of unbound gaseous mass and the smaller the final stellar mass fraction (see Table 5.1). These trends with total mass are very encouraging, suggesting that our feedback model may reproduce the shape of the faint-end of the galaxy luminosity function in hierarchical clustering scenarios (e.g. Trentham & Tully 2002). This has been an elusive goal in high-resolution simulations of galaxy formation thus far. The self-consistent regulation of the star formation activity together with the natural production of vigorous outflows can be viewed as an important achievement of our new feedback model.

Finally, in Fig. 5.7 we show the fraction of metals locked into the unbound gas (thin lines) and into the stellar component (thick lines), as a function of total mass after $0.85\,h^{-1}$Gyr. We show the results for simulations with $\epsilon_c = 0.1$ (dotted line), $\epsilon_c = 0.5$ (dashed line) and $\epsilon_c = 0.9$ (dashed-dotted line) and for our higher resolution tests with $\epsilon_c = 0.5$ (squared asterisks). From this figure we can see that the unbound gas is highly enriched, even in the largest mass systems. The anti-correlation in this figure indicates that the fraction of metals locked into the unbound gas increases with decreasing total mass. In contrast, the fraction of metals locked into stars increases slightly with the virial mass. In this case, note that the fraction of metals locked into the stellar component is less than 20 per cent which is perhaps suggestive of the need for a top-heavy IMF (Nagashima et al. 2005). Also note that in the simulations with $\epsilon_c = 0.1$, most of the metal content of the system is located in the unbound gas.

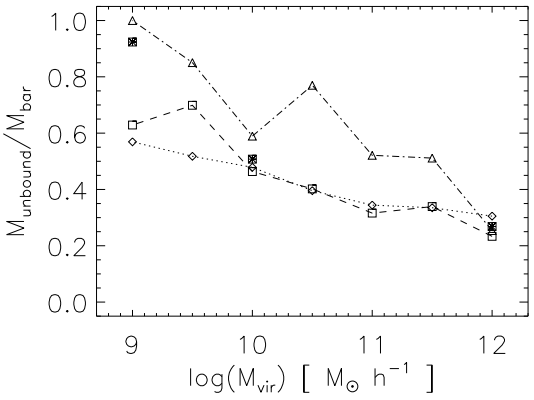


Figure 5.6: Fraction of unbound gas as a function of total baryonic mass for simulations with $\epsilon_c = 0.1$ (dotted line), $\epsilon_c = 0.5$ (dashed line) and $\epsilon_c = 0.9$ (dashed-dotted line) after $0.85\,h^{-1}$Gyr of evolution. We also show the results for our higher resolution simulations with $\epsilon_c = 0.5$ (squared asterisks).

The above results suggest that smaller systems would contribute to the enrichment of the intergalactic medium with larger fractions of their metal production. However, as large systems also produce important fractions of unbound and enriched gas, the amount of metals they release into the intergalactic medium could be very significant or even dominant. This behaviour may explain recent observational findings on the stellar mass-metallicity relation (Tremonti et al. 2004) where fewer metals were detected in massive galaxies than expected for closed box models, demonstrating rather directly that galaxies of all masses may have lost heavy elements to their surroundings.

## 5.4 STAR FORMATION EFFICIENCY AND THE KENNICUTT LAW

Our decoupling, star formation and feedback schemes contain a number of numerical and physical parameters for which values must be chosen. We discussed the phase separation parameters $\alpha$, $T_*$ and $\rho_*$ in sections **??** and **??**, arguing that the behaviour of our algorithms is not sensitive to their precise values; $\alpha$ is chosen to achieve effective decoupling of gas at very different entropies while the values of density and temperature which define cold gas for the purpose of our feedback algorithms are based on the shape of the radiative cooling curve and the properties of observed star-forming regions. In addition, values must be chosen for the efficiencies of star formation and of energy deposition in hot and cold gas, for the chemical yields

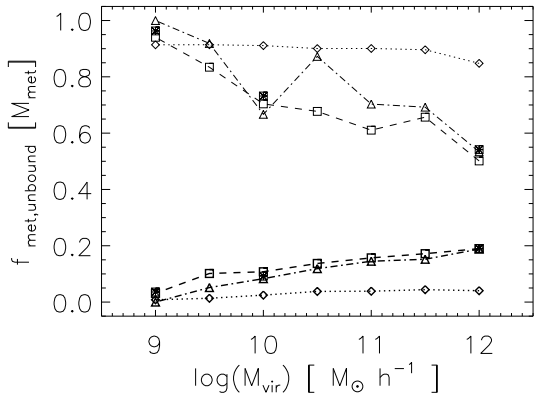


Figure 5.7: Fraction of metals locked into unbound gas (thin lines) and into stars (thick lines) as a function of total mass for simulations with $\epsilon_c = 0.1$ (dotted lines), $\epsilon_c = 0.5$ (dashed lines) and $\epsilon_c = 0.9$ (dashed-dotted lines) after $0.85\,h^{-1}$Gyr of evolution. We also show results for our higher resolution simulations with $\epsilon_c = 0.5$ (squared asterisks).

from stellar evolution, and for parameters which regulate the distribution of metals between the gas components. In previous sections we explored the effects of varying the efficiencies with which energy is deposited in hot and cold gas and we tied the distribution of metals to that of energy. In this section we determine appropriate values for the star formation efficiency.

Observationally, it is found that star formation rate per unit area is remarkably tightly correlated with total gas surface density (Kennicutt 1998). This purely empirical relation holds as a function of radius within galaxies as well as among galaxies of very different mass, type and redshift. It is a considerable challenge for galaxy formation models such as our own to reproduce this "Kennicutt Law", since we have freedom only to adjust the overall efficiency of star-formation; the slope and the surprisingly small scatter of the relation must emerge "naturally" from the self-regulation of star formation within the numerical model. Below we show that our model can indeed reproduce the observed behaviour both for the simplified collapse model used in earlier sections and for an equilibrium galaxy model with structure similar to that of the Milky Way.

Our star formation algorithm assumes a star formation rate per unit volume equal to

$$\dot{\rho}_\star = c\,\frac{\rho}{\tau_{\rm dyn}}, \tag{5.1}$$

where $\rho_\star$ is the density of the new born stars, $\rho$ is the gas density, $\tau_{\rm dyn}$ is the dynam-

ical time of the gas, defined simply as $\tau_{\rm dyn} = 1/(4\pi G\rho)^{1/2}$, and $c$ is a star formation efficiency parameter (see Chapter 2 for details). In the numerical experiments analysed above, we used $c = 0.1$. In this Section, we investigate the value required to reproduce the Kennicutt Law by comparing our previous collapse model F12-0.5, with a virial mass of $10^{12}\ h^{-1}{\rm M}_\odot$, to an otherwise identical model where we lowered the star formation efficiency to $c = 0.01$. In the upper panel of Fig. 5.8 we show the resulting projected surface star formation rates and surface gas densities at three times, 0.5, 1.0 and 1.5 Gyr, averaging over broad annuli out to a radius of 30 $h^{-1}$ kpc. The observed Kennicutt relation is indicated on this plot by a dashed straight line. Clearly, for $c = 0.1$ (the open symbols) star formation is much more efficient in the simulation than is observed; disk gas is consumed rapidly, and there is considerable scatter about the mean relation. Reducing $c$ by an order of magnitude reduces the star formation rates at given surface density by a similar factor, resulting in a much broader distribution of gas surface densities and an excellent fit to the zero-point slope and scatter of the observed relation. In addition, it is clear that as our idealized system builds up its disk it evolves along the Kennicutt relation. It is interesting that although star formation activity is reduced substantially for $c = 0.01$, the SN feedback model is still able to produce a strong galactic wind. After 1.5 Gyr of evolution, we find that $\sim 10$ per cent of all baryons are both unbound and enriched with heavy elements.

The collapse initial conditions used here and above are highly idealized. In order to assess whether the apparent agreement with observation extends to quiescent star formation in an equilibrium system, we analyze two further simulations from initial conditions representing a spiral galaxy similar in structure to the Milky Way. The initial system is based on that studied in Springel et al. (2005). It consists of a dark matter halo, a stellar bulge, a diffuse hot gas halo, and a disk with 10 per cent of its mass in gas and the rest in stars. The dark matter distribution is modelled as a spherical NFW distribution with a circular velocity at $r_{\rm vir} = 160h^{-1}$kpc of 161 km s$^{-1}$ and a concentration parameter of 9 (Navarro, Frenk & White 1996, 1997). The disk has a radial scalelength of $2.5\,h^{-1}$kpc, a vertical scale-height of $0.5\,h^{-1}$kpc, and a Toomre stability parameter[1] of $Q > 1$ for the stars. The spherical bulge is taken to have an exponential profile with scalelength 0.2 times that of the disc. The density of the hot gas follows that of the dark matter. The bulge, disc, hot gas halo and dark matter halo are taken to have initial masses of 0.13, 0.39, 0.059 and $9.0 \times 10^{11}\,h^{-1}{\rm M}_\odot$ respectively. Initially dark matter, gas and stars are represented by simulation particles with mass 300, 2.0 and $15 \times 10^5\,h^{-1}{\rm M}_\odot$ respectively. We have used gravitational softenings of 0.16, 0.32 and 0.2 $h^{-1}$ kpc for gas, dark matter and

[1]The Toomre parameter measures the stability of a galactic system. It is defined as $Q = \frac{\kappa\sigma_v}{3.36G\Sigma_{\rm d}}$, where $\kappa$ is the epyciclic frequency, $\sigma_v$ the radial velocity dispersion of the stars, $G$ the gravitational constant and $\Sigma_{\rm d}$ the projected disk surface density. The Toomre parameter should be $Q > 1$ in order to prevent instabilities in the disk and to allow spiral structures to develop.

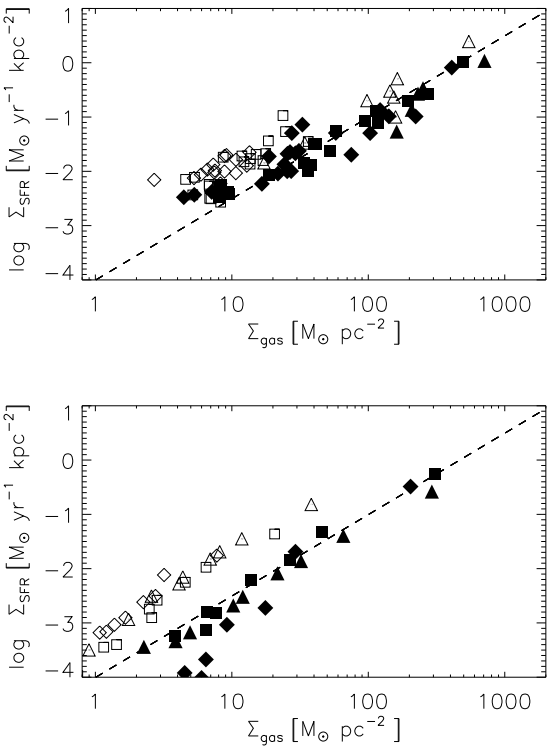


Figure 5.8: The upper panel shows projected star formation rate density as a function of gas surface density for two simulations of the collapse of a $10^{12}\,h^{-1}\mathrm{M}_{\odot}$ mass system. Both surface densities are averaged over a series of annuli in face-on projections of the simulations. Open symbols refer to the model F12-0.5 discussed above at times 0.5 (triangles), 1.0 (squares) and 1.5 Gyr (diamonds), while corresponding filled symbols refer to the same times and to an otherwise identical model with $c = 0.01$. The lower panel shows results for two simulations from equilibrium initial conditions representing a spiral galaxy with structure similar to that of the Milky Way. The symbols refer to the same times and values of $c$ as in the upper panel. The dashed line in both panels represents the relation of Kennicutt (1998).

star particles, respectively. In these simulations, we assume that bulge and disk stars are old (i.e. they do not contribute to metal and energy ejection). Metals and SN energy are exclusively produced by the new stars which can be formed from the 10% of the initial gas component. The system is set up in equilibrium and we followed its evolution using our full phase separation, star formation and feedback models with feedback parameters $\epsilon_r = 0$ and $\epsilon_c = 0.5$ and with $c = 0.1$ and $c = 0.01$. The star formation physics thus corresponds to the two versions of F12-0.5 compared above.

The lower panel of Fig. 5.8 shows the Kennicutt relations we find for these simulations at three different times. Despite the difference in initial conditions, the results resemble those found already for F12-0.5. For $c = 0.1$ the disk gas is used up quite rapidly (only 30, 17 and 11 per cent of the initial cold disk gas remains in the disk at the three times shown) and the star formation rates lie well above the empirical Kennicutt relation. With the lower star formation efficiency the observational relation is matched quite well and gas consumption times are lengthened (81, 67 and 54 per cent of the initial cold disk gas now remains in the disk at the three times shown). It is remarkable that even with the relatively modest star formation rates now found in this model, a significant galactic wind is generated. At the final time ($t = 1.5$ Gyr), 51 per cent of all metals formed are in the hot halo gas and 99 per cent of this gas is formally unbound and will likely leave the galaxy. Dividing this unbound mass by the age of the system leads to an estimated mass-loss rate in the wind of $6 M_\odot$ yr$^{-1}$ which can be compared with the mean star formation rate of $2 M_\odot$ yr$^{-1}$ averaged over the duration of the simulation. The ratio of these two rates is gratifyingly close to observational estimates for real wind-blowing galaxies (Martin 1999, 2004). The correct representation of the Kennicutt law found for $c = 0.01$ suggests this star formation efficiency as a good choice. The tests of this section confirm that our new SN-feedback model can match the observed phenomenology of star formation both during starburst episodes and during phases of quiescent star formation.

# Chapter 6

# Disk Formation and Supernova Feedback

Numerical simulations are a powerful tool to study the formation of galaxies. In particular, reproducing the chemical, dynamical, and angular momentum properties of spiral galaxies altogether, in the context of a cosmological scenario, is a big challenge for galaxy formation models. In Chapter 3 we have explained that simulations which do not include the effects of SN energy feedback fail to reproduce the main properties of disk galaxies. We have illustrated this behaviour by using a simulation of a galaxy specifically chosen to evolve into a disk-like system. In this experiment, a well-formed, extended disk could not form because of the early consumption of gas into stars which contributed to the formation of an important spheroidal, stellar component that dominates the baryonic content of the system at redshift $z = 0$. We have also found that the gas component suffered from the catastrophic angular momentum loss, being unable to describe the formation of a spiral galaxy with observational counterparts.

As it has been suggested by theoretical models and observations, the formation of disks seems to be related to quiescent phases in which the gas collapses smoothly, conserving its specific angular momentum. This process requires that enough baryons stay in the form of gas to build up the disks while the survival of the disks depends on their stability properties within the potential wells where they form. In a hierarchical model, mergers and interactions are common events which significantly affect the properties of interacting systems. In particular, depending on the properties of the encounters and the internal physical characteristics of the disks, they can either survive or be destroyed during these violent events. Numerical simulations have found that, in most merger events, the star formation activity is enhanced as the result of gas inflows triggered during the interaction, converting an important fraction of the gaseous mass into stars. As the rate of mergers increases with redshift, the existence of extended disks at redshift $z = 0$ suggests that they have formed recently, or that they have not experienced major mergers or interactions in the recent past, as it is thought to be the case for the thin disk of our Milky Way Galaxy.

In this context, in order to understand the formation of disk systems in a hierarchical scenario, some physical process, which prevents early gas consumption allowing the gas reservoirs not to be exhausted at early epoques, needs to be invoked to explain the survival of extended disk galaxies. SN explosions are thought to provide a self-regulated mechanism for star formation through the heating and disruption of cold gas clouds, helping to keep baryons in the form of gas for a longer period, and therefore their effects are supposed to be linked to disk formation.

In order to overcome the problems found in disk galaxy formation simulations so far, we have developed a new method to include SN energy feedback within our code for metal enrichment (Chapter 2), which we have described and tested in Chapters 4 and 5. By analysing simulations of isolated galaxies, we have shown that our model succeeds in reproducing the main physical characteristics associated to SN explosions, in relation to the self-regulation of the star formation activity and the generation of strong, mass-loaded galactic winds which, on its turn, could help to contaminate the intergalactic medium with metals. This Chapter is devoted to revisit disk formation and analyse how the inclusion of our model for SN energy feedback and our multiphase treatment for the ISM affects the formation of disk systems, carrying out a comparison with the results obtained in Chapter 3. Our goal is to understand and test the role played by SNe in the star formation activity and the morphology and dynamics of the disks using realistic initial conditions that allow the consistent treatment of processes such as mergers, interactions, inflows.

This Chapter is organized as follows. In Section 6.1 we summarize the main characteristics of the simulations of disk-like galaxies run with our model for SN energy feedback. We use these tests to analyse the main properties of the galaxies at redshift $z = 0$ (Section 6.2.1) and their star formation histories (Section 6.2.2). We also study several important galaxy properties such as dynamics (Section 6.2.3), angular momentum (Section 6.2.4) and morphology (Section 6.2.5). In Section 6.3 we select one of the simulated galaxies and analyse in more detail its formation process (Section 6.3.1), stellar age distribution (Section 6.3.2) and chemical properties (Section 6.3.3). Finally, in Section 6.3.4 we describe the gas flows and metallicity transport driven by SN energy feedback.

## 6.1 DISK FORMATION SIMULATIONS WITH SN ENERGY FEEDBACK

In order to study the effects of SN energy feedback on the evolution of disk systems, we simulate the formation of a spiral-like galaxy by using the resimulation technique explained in Section 3.1. This initial condition (the same as in Chapter 3) has been extracted from a large volume of a ΛCDM simulation by requiring that the main structure did not experience a major merger since redshift $z = 1$. This condition

produces the correct environmental condition for an extended disk to be able to form. The simulation has adequate high spatial resolution to analyse in detail the formation of a single galaxy in the correct cosmological setting with a total of $\sim 3$ million particles at redshift $z = 0$. The initial conditions are consistent with a $\Lambda$CDM Universe with the following cosmological parameters: $\Omega_\Lambda = 0.7$, $\Omega_{\rm m} = 0.3$, $\Omega_{\rm b} = 0.04$, a normalization of the power spectrum of $\sigma_8 = 0.9$ and $H_0 = 100\ h$ km s$^{-1}$ Mpc$^{-1}$ with $h = 0.7$. The mass resolution for dark matter and gas particles is $1.6 \times 10^7$ and $2.4 \times 10^6\ h^{-1}$ M$_\odot$, respectively. At redshift $z = 0$, the central galaxy is sampled with $\sim$ 120000, 30000 and 60000 dark matter, gas and star particles, respectively.

In the simulations analysed in this Chapter, we have assumed a star formation efficiency of $c = 0.1$. We have used a maximum gravitational softening of 0.8 $h^{-1}$ kpc (in physical units) for gas, dark matter and star particles. We have run a set of simulations including our model for SN energy feedback, assuming different input feedback parameters (different $\epsilon_c$ values) with $\epsilon_r = 0$ (i.e. no SN energy lost by radiation). We have also run a test with $\epsilon_r = 0.3$. In this latter experiment, the metal fractions dumped into the cold and hot phase were assumed to be $\epsilon_c^m = \epsilon_h^m = 0.5$. The computational time needed for running each of these high resolution simulations in 16 processors is of about 200 CPU hs. The final set of simulations required 50 CPU days. The main characteristics of the simulations are summarized in Table 6.1.

## 6.2 RESULTS AND ANALYSIS

### 6.2.1 THE SIMULATED GALAXIES AT $z = 0$

In order to analyse the characteristics of the simulated galaxies and test the dependence on the input parameter $\epsilon_c$, we plot in Figs. 6.1 to 6.5 the distributions of dark matter, gas and star particles within $1.5 \times r_{\rm opt}$ at redshift $z = 0$, for the different tests and for two different spatial projections. In these plots, we have aligned the $z-$axis along the direction of the total angular momentum of the system and hence, $xy$ and $xz$ projections correspond to face-on and edge-on views, respectively.

From these figures, we can see that the inclusion of our SN energy feedback model has helped to produce systems in which larger fractions of gas survive up to redshift $z = 0$ without having been transformed into stars. Conversely, in Chapter 3 we found a dominant stellar component and a small fraction of leftover gas, which was reflected in the small value for the mass gas fraction $f_{\rm gas} = 0.026$. If we include our model for SN energy feedback, at redshift $z = 0$ we get larger total gas fractions in the range $f_{\rm gas} = [0.047 - 0.061]$, a factor of $2 - 3$ times larger than the result for DZ, as shown in Table 6.1. Note that the gas fractions are also influenced by the fact that gas can also be lost from the galaxy as the result of galactic winds.

Table 6.1: Main characteristics of the simulated disk-like systems: fraction of energy assumed to be lost by radiation ($\epsilon_r$) and fraction of energy and metals distributed into the cold phase ($\epsilon_c$ and $\epsilon_c^m$, respectively). We also list the gas mass fraction ($f_{\rm gas}$) within $2 \times r_{\rm opt}$ at $z = 0$ (defined as the ratio between the gaseous mass and the baryonic mass), the fraction of stellar mass formed in the last 7 $h^{-1}$ Gyr ($f_{t<7}$) within $2 \times r_{\rm opt}$, and the stellar mass within $2 \times r_{\rm opt}$ ($M_{\rm s}$) for the galaxies at redshift $z = 0$.

| Test | $\epsilon_r$ | $\epsilon_c$ | $\epsilon_c^m$ | $f_{\rm gas}$ | $f_{t<7}$ | $M_{\rm s}$ |
|---|---|---|---|---|---|---|
| DZ | 1 | - | - | 0.026 | 0.24 | 13.36 |
| FZ-0.3 | 0 | 0.3 | 0.3 | 0.047 | 0.36 | 4.18 |
| FZ-0.5 | 0 | 0.5 | 0.5 | 0.048 | 0.48 | 5.32 |
| FZ-0.75 | 0 | 0.75 | 0.75 | 0.061 | 0.56 | 5.57 |
| FZ-0.9 | 0 | 0.9 | 0.9 | 0.055 | 0.51 | 6.35 |
| FZ-0.35-R | 0.3 | 0.35 | 0.5 | 0.047 | 0.44 | 7.28 |

From these figures, we can also appreciate that the gaseous components have preferentially located onto disk-like structures, some of them showing bars (e.g. Fig. 6.1). In particular, our test FZ-0.3, where only a 30% of the SN energy was assumed to be dumped into the cold phase, shows the smallest SN feedback impact on the mass distribution with respect to test DZ (no energy feedback). In contrast, in tests FZ-0.5, FZ-0.75, FZ-0.9 and FZ-0.35-R, where larger fractions of the energy were assumed to contribute to the thermal energy in the cold phase, well-defined disk structures formed.

On its turn, the existence of extended gaseous disks has allowed the formation of stellar disks structures with different extensions and typical heights. We can also appreciate from the figures the existence of two stellar spheroidal structures superposed to the disks, a small one located at the centre and a more diffuse one surrounding the disk. From this first view, the fact that our simulations with SN energy feedback produced systems with different components similar to disks, bulges and stellar haloes are encouraging and suggest that SN energy feedback is a key process for the formation of spiral galaxies.

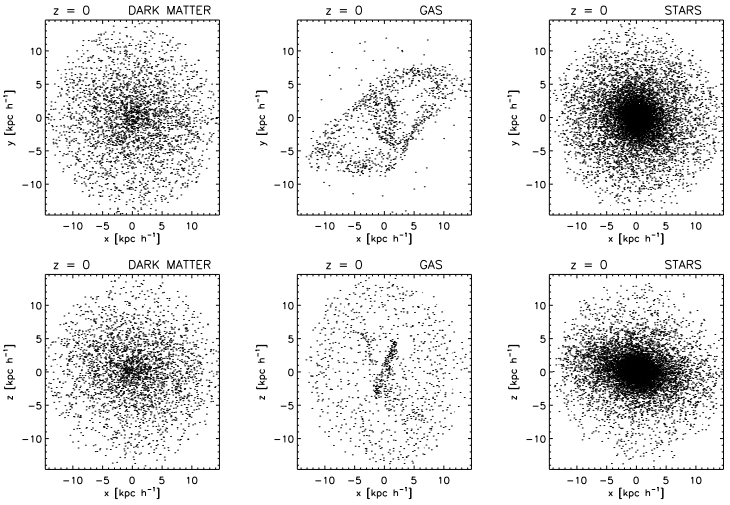


Figure 6.1: Face-on (upper panels) and edge-on (lower panels) projections of the comoving distribution of dark matter, gas and star particles within $1.5 \times r_{\rm opt}$, in our test FZ-0.3, run with SN feedback input parameter of $\epsilon_c = 0.3$, at redshift $z = 0$.

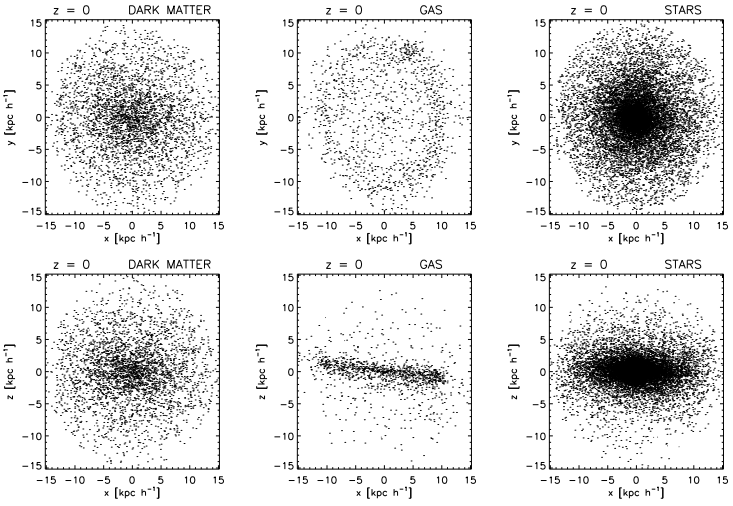


Figure 6.2: Face-on (upper panels) and edge-on (lower panels) projections of the comoving distribution of dark matter, gas and star particles within $1.5 \times r_{\rm opt}$, in our test FZ-0.5, run with SN feedback input parameter of $\epsilon_c = 0.5$, at redshift $z = 0$.

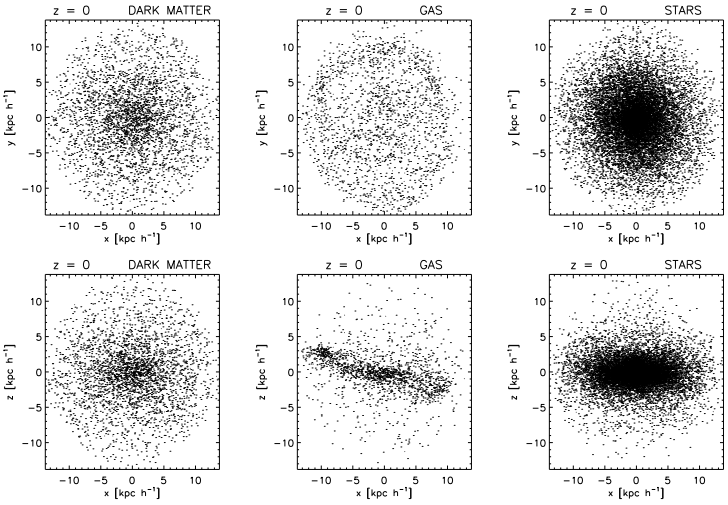


Figure 6.3: Face-on (upper panels) and edge-on (lower panels) projections of the comoving distribution of dark matter, gas and star particles within $1.5 \times r_{\rm opt}$, in our test FZ-0.75, run with SN feedback input parameter of $\epsilon_c = 0.75$, at redshift $z = 0$.

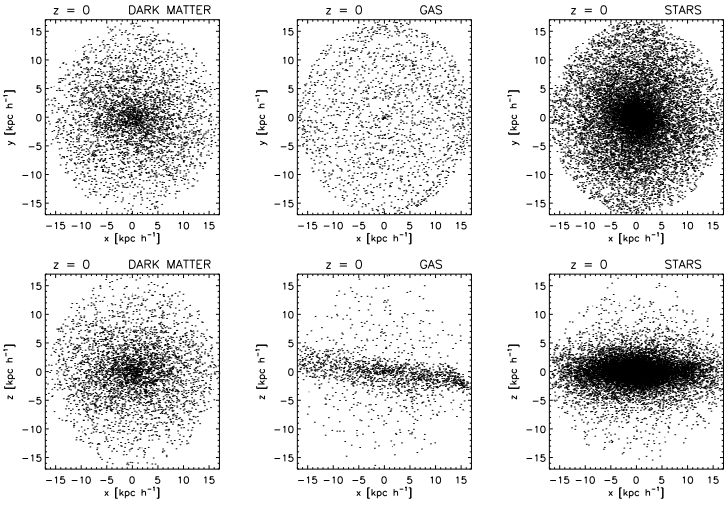


Figure 6.4: Face-on (upper panels) and edge-on (lower panels) projections of the comoving distribution of dark matter, gas and star particles within $1.5 \times r_{\rm opt}$, in our test FZ-0.9, run with SN feedback input parameter of $\epsilon_c = 0.9$, at redshift $z = 0$.

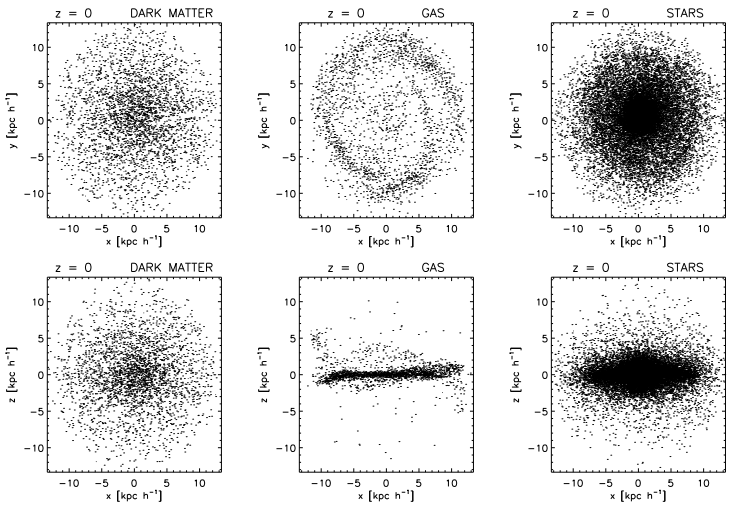


Figure 6.5: Face-on (upper panels) and edge-on (lower panels) projections of the comoving distribution of dark matter, gas and star particles within $1.5 \times r_{\rm opt}$, in our test FZ-0.35-R, run with SN feedback input parameter of $\epsilon_c = 0.35$, and assuming a fraction of energy lost by radiation of $\epsilon_r = 0.3$, at redshift $z = 0$.

### 6.2.2 Star Formation Histories

In Fig. 6.6 we show the star formation rates (SFRs) for our tests run with SN energy feedback (solid lines): FZ-0.3 (upper right panel), FZ-0.5 (middle left panel), FZ-0.75 (middle right panel), FZ-0.9 (lower left panel) and FZ-0.35-R (lower right panel). In the upper left panel and also in the other panels, we show the result for the test DZ (dashed lines, Fig. 3.9 in Chapter 3) for comparison. From these figures, we can appreciate that SN energy feedback produces a general decrease in the SFR level in comparison to the results obtained if no energy feedback is included, as it was the case in simulation DZ. The SN energy feedback helps to regulate the star formation activity preventing the exhaustion of the gas reservoir at very early times and allowing the triggering of recent star formation activity.

For particular values of the input feedback parameters, we find that recent star formation activity can occur at higher levels than in the no feedback counterpart in DZ. However, note that the SFRs for the tests run with SN energy feedback show different patterns, indicating that the self-regulation of the star SFR depends on the particular evolutionary history of each galaxy. The self-regulation of the star formation activity driven by SN energy feedback is also reflected in the bursty behaviour of the SFRs. Note that each star formation burst is followed by an important decrease in the SFR level. This is a consequence of the strong outflows triggered by SN feedback produced by the heating up and expansion of the gas

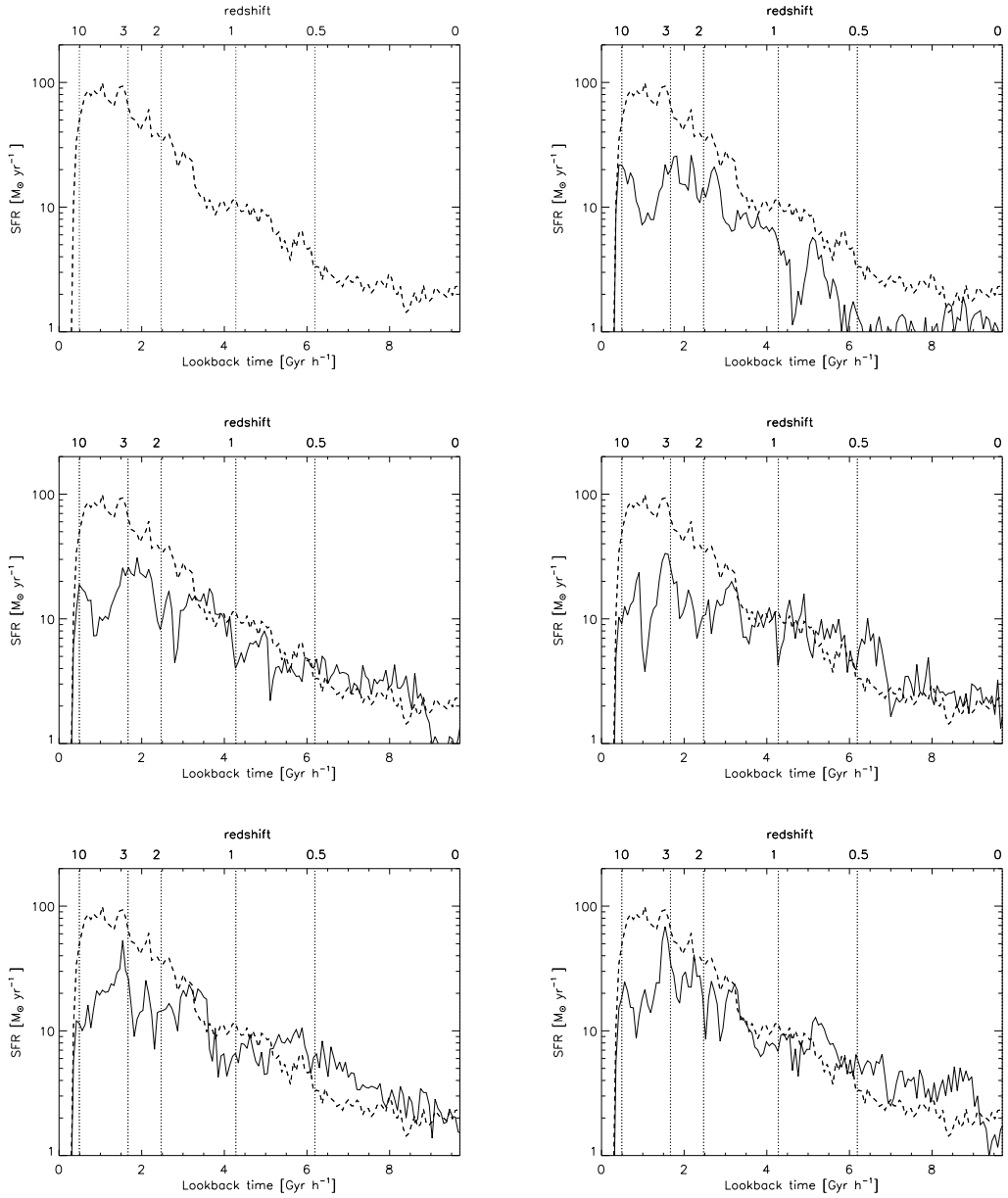


Figure 6.6: Star formation rate as a function of time and redshift (solid lines) for our tests FZ-0.3 (upper right panel), FZ-0.5 (middle left panel), FZ-0.75 (middle right panel), FZ-0.9 (lower left panel) and FZ-0.35-R (lower right panel). In the upper left panel we show the result for the test DZ (dashed line), run with no energy feedback and analysed in Chapter 3. We also include the DZ curve as dashed lines in the other panels, for comparison. The plots correspond to stars located within the corresponding $1.5 \times r_{\rm opt}$ at redshift $z = 0$.

surrounding SN explosions, as it was discussed in Chapter 4 (see also Section 6.3.4).

In particular, we find that for test DZ, only a 24% of the stellar mass at $z = 0$ formed in the last 7 $h^{-1}$ Gyr, as it is shown in Table 6.1, where we list this magnitude for all analysed tests. As it can be seen from this Table, the tests run with SN energy feedback have larger fractions of recently-born stars $f_{t<7} \sim 50\%$ (except for test FZ-0.3). This behaviour shows the ability of our model to allow the formation of stars at later times. From the SFRs obtained for tests with different $\epsilon_c$ value, we find that as $\epsilon_c$ increases, more recent star formation activity can occur. Note that the final stellar mass in the system ($M_{\rm s}$, also listed in Table 6.1) increases with the feedback input parameter. This result is explained by the fact that simulations with larger $\epsilon_c$ values decrease more strongly the SFR during the first stages of evolution, leaving more leftover gas to feed further star formation activity.

### 6.2.3 DYNAMICS

It is accepted that, in the local universe, spiral galaxies have well-defined dynamical properties for the spheroidal and disk components, which any galaxy formation model should be able to reproduce. In this Section, we investigate the dynamics of our simulated galaxies and the impact of SN energy feedback on them. In Figs. 6.7 to 6.11, we plot the angular momentum component of star and gas particles along the direction of the total angular momentum of the corresponding simulated galaxies, as a function of projected distance onto the disk plane. Particles in co- and counter-rotation have been plotted separately for the sake of clarity. We also estimated the theoretical curve assuming that particles follow exact circular orbits in the corresponding potential well. Note that the potential wells are mainly determined by the dark matter.

In contrast to the results obtained for the DZ test analysed in Chapter 3 (Fig. 3.5), we find that, in these SN energy simulations, the gaseous components determine very tight relations which lie on the theoretical predictions, indicating that the gas components form very well defined disk configurations. These figures also show that the gas has conserved angular momentum, and hence SN energy feedback has contributed to attenuate the catastrophic angular momentum loss (see also Section 6.2.4). Note that, in test FZ-0.3, where only 30% of the SN energy was assumed to be dumped into the cold phase, there is still some angular momentum loss by the gas component (Fig. 6.7).

The angular momentum distribution found for the stars is also consistent with the theoretical prediction, indicating that the stars also contribute to define the disks in these simulations. Note that there are extra stellar components which are consistent with spheroidal structures where the material is disordered. These stars determine bulges and stellar haloes. It is also interesting to note that the theoretical prediction of these tests is slightly different from the one obtained for DZ in Chapter 3, in such

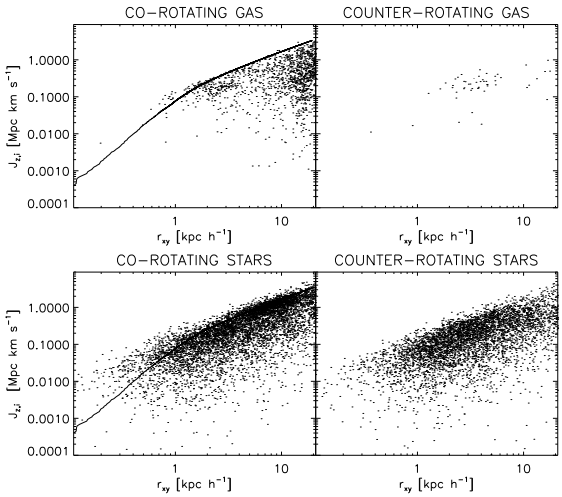


Figure 6.7: Angular momentum for star and gas particles in co- and counter-rotation as a function of projected distance onto the disk plane for our test FZ-0.3 run with SN energy feedback with $\epsilon_c = 0.3$. The solid line shows the theoretical relation assuming assuming that particles follow exact circular orbits in the corresponding potential well.

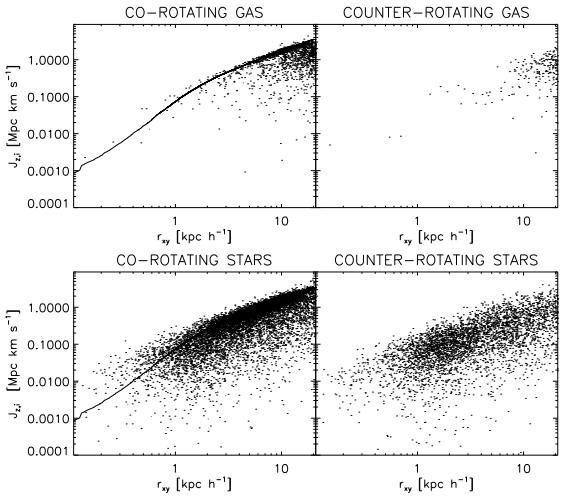


Figure 6.8: Angular momentum for star and gas particles in co- and counter-rotation as a function of projected distance onto the disk plane for our test FZ-0.5 run with SN energy feedback with $\epsilon_c = 0.5$. The solid line shows the theoretical relation assuming that particles follow exact circular orbits in the corresponding potential well.

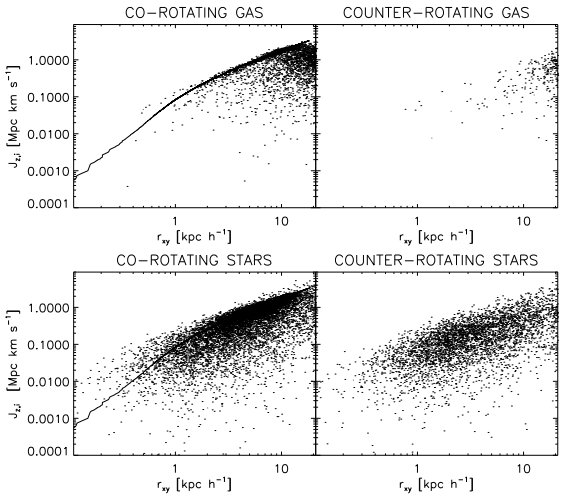


Figure 6.9: Angular momentum for star and gas particles in co- and counter-rotation as a function of projected distance onto the disk plane for our test FZ-0.75 run with SN energy feedback with $\epsilon_c = 0.75$. The solid line shows the theoretical relation assuming that particles follow exact circular orbits in the corresponding potential well.

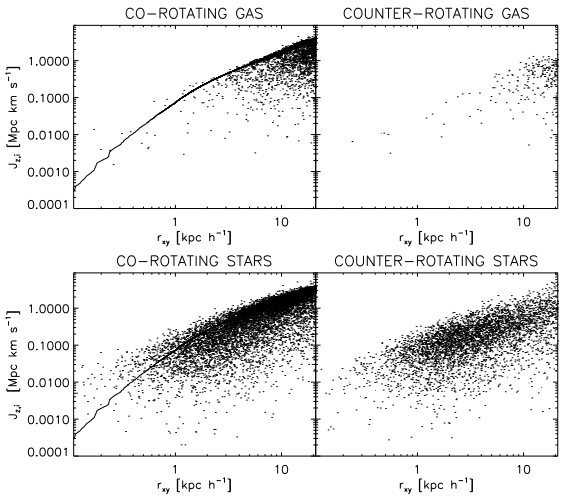


Figure 6.10: Angular momentum for star and gas particles in co- and counter-rotation as a function of projected distance onto the disk plane for our test FZ-0.9 run with SN energy feedback with $\epsilon_c = 0.9$. The solid line shows the theoretical relation assuming that particles follow exact circular orbits in the corresponding potential well.

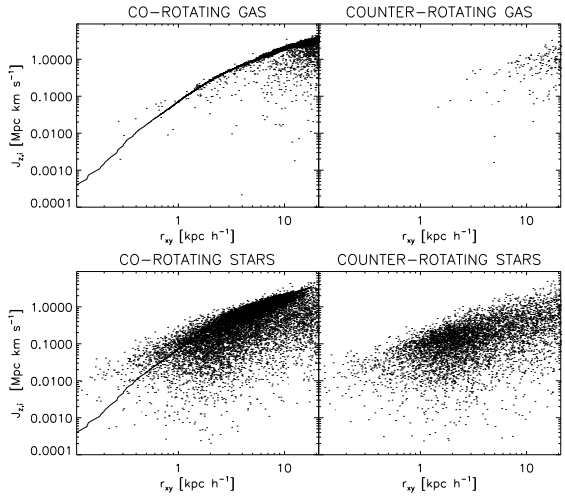


Figure 6.11: Angular momentum for star and gas particles in co- and counter-rotation as a function of projected distance onto the disk plane, for our test FZ-0.35-R run with SN energy feedback with $\epsilon_c = 0.5$ and $\epsilon_r = 0.3$. The solid line shows the theoretical relation assuming that particles follow exact circular orbits in the corresponding potential well.

a way that the predicted angular momentum curve is shifted downwards when SN feedback is included. As the angular momentum prediction is proportional to the circular velocity of the system ($j_i \simeq v_{\rm circ} \times r_i$) determined by the mass distribution, the shift in angular momentum indicates that SN energy feedback produces potential wells shallower than the one obtained in DZ (see also Section 6.3.1).

The fact that our treatment for SN energy feedback has been able to produce galaxies with angular momentum distributions in good agreement with the theoretical prediction for disk structures constitutes a dramatic success of our model, and opens the possibility to study galaxy formation in a consistent way that has not hitherto been possible. Recall that the catastrophic angular momentum loss has been widely investigated during the last decade (e.g. Domínguez-Tenreiro et al. 1998; Okamoto et al. 2003; Robertson et al. 2004), but the poor modellization of SN energy feedback and of the multiphase character of the interstellar medium has not allowed a convergent solution to be found.

The dynamical properties of the different components of the simulated galaxies can be also appreciated in Fig. 6.12 where we show the ratio between velocity dispersion and azimuthal velocity for stars in our tests FZ-0.3, FZ-0.5, FZ-0.75, FZ-0.9 and FZ-0.35-R. In contrast to the result obtained for DZ (Fig. 3.6 in Chapter 3, reproduced in the upper-right panel of this Figure), we find, when SN energy feedback is considered, an important fraction of the star particles with $\sigma/v_\phi < 1$, indicating

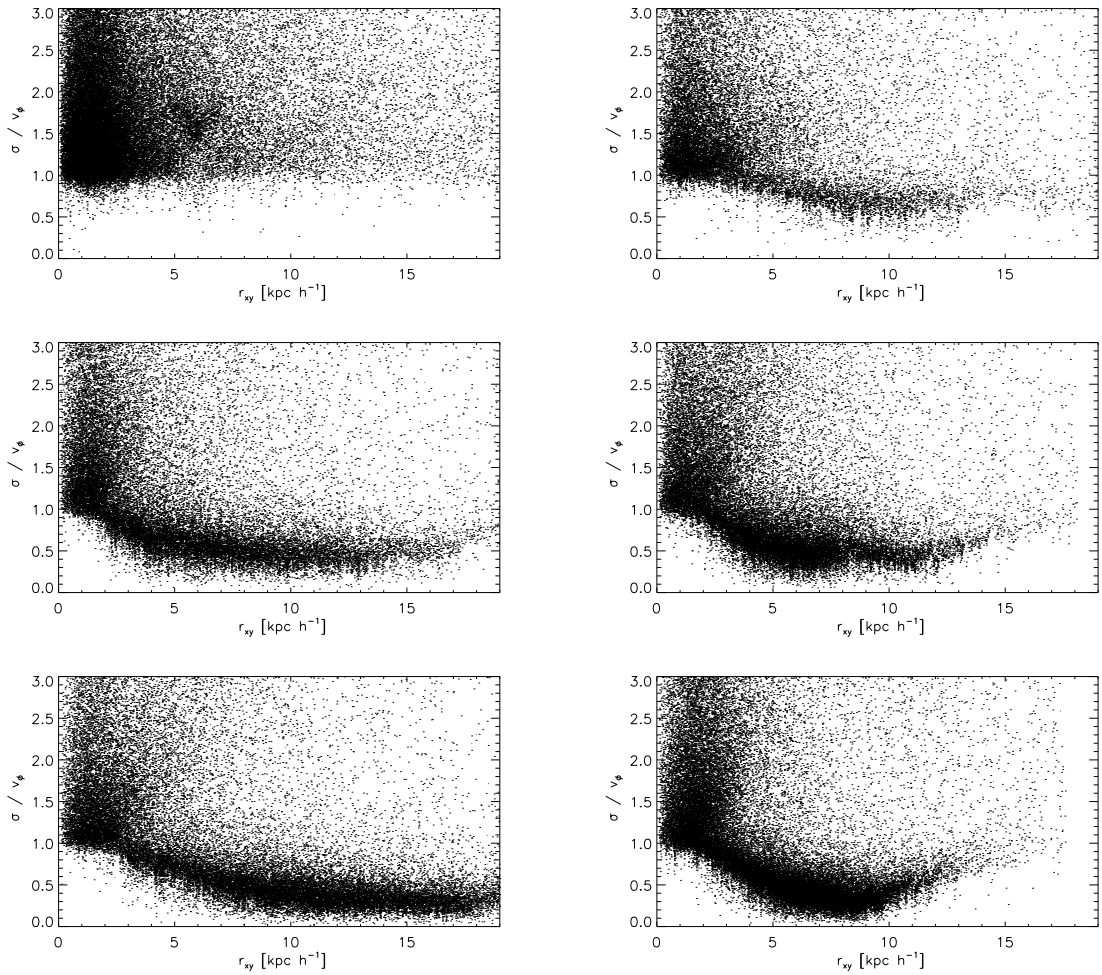


Figure 6.12: Distribution of velocity dispersion over azimuthal velocity, $\sigma/v_\phi$, as a function of projected radius, for the stars in our tests FZ-0.3 (upper right panel), FZ-0.5 ( middle left panel), FZ-0.75 (middle right panel), FZ-0.9 (lower left panel) and FZ-0.35-R (lower right panel). For comparison, in the upper left panel we show the results for test DZ, run with no energy feedback and analysed in Chapter 3.

that the azimuthal velocity dominates over the velocity dispersion, as expected in disk-like structures. Note that the different feedback input parameters produce disks of different level of order and spatial extension, as already found from other indicators. The spheroidal components with $\sigma/v_\phi > 1$ are also clearly distinguished. Note that an important fraction of stars in these components are located at the centre of the systems while the remaining fraction is spread up to the edge of the distributions. These stars form the bulges and stellar haloes, respectively.

### 6.2.4 ANGULAR MOMENTUM

As it was already explained in Chapter 3, the evolution of the specific angular momentum plays a fundamental role in the formation of spiral galaxies. In Chapter 3 we have shown that the specific angular momentum of a simulation test without SN energy feedback (test DZ) produced configurations with too low specific angular momentum values in comparison with observations, being inconsistent even with the properties of elliptical galaxies.

In Fig. 6.13 we show the specific angular momentum of bulges (open symbols) and disks (filled symbols) in our tests run with SN energy feedback, as a function of baryonic mass, at redshift $z = 0$. We also include the results for DZ, for comparison. We have segregated bulges and disks according to distance to the centre and height over the disk plane, in order to compare with the results obtained in Chapter 3. We also show the corresponding value for the dark matter components, which is similar for all simulations. From this figure we can appreciate that the inclusion of our model for SN energy feedback produces disk and bulge components with angular momentum content in good agreement with the observed trends for spirals and ellipticals, respectively. Note that the disks have specific angular momentum values comparable to those of the dark matter haloes, indicating that the dark matter and baryonic components have received the same initial angular momentum, and that the disk components have not suffered from angular momentum loss during their evolutionary processes. These results demonstrate that SN energy feedback is a key mechanism which affects the formation of galaxies in such a way that disk and bulge structures with angular momentum content similar to those observed in galaxies can form.

### 6.2.5 MORPHOLOGY

The different properties of the simulated disks can also be analysed quantitatively by studying the parameters obtained from bulge-disk decompositions to the projected surface mass distributions, as explained in Appendix D. As it can be seen from Table 6.2, the inclusion of SN energy feedback has allowed the formation of disks with scalelengths as large as $\sim 5\,h^{-1}$ kpc, depending on the input $\epsilon_c$ parameters. Also note

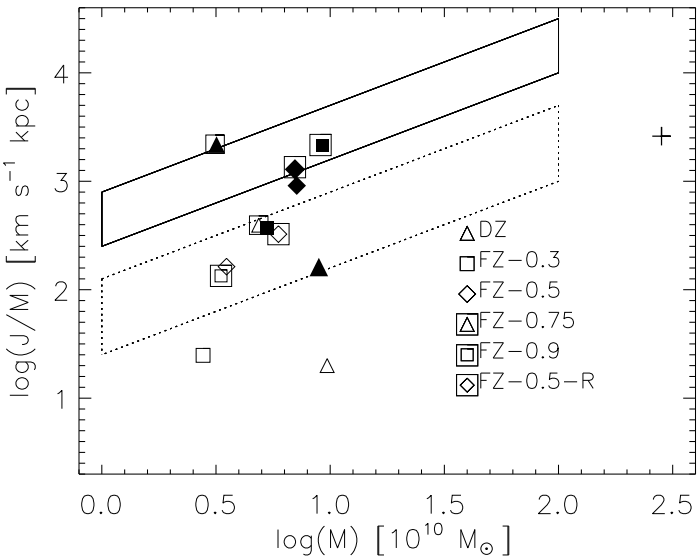


Figure 6.13: Specific angular momentum for the disk (filled symbols) and bulge (open symbols) components in our disk formation simulations DZ (triangles), FZ-0.3 (squares), FZ-0.5 (diamonds), FZ-0.75 (squared triangles), FZ-0.9 (squared squares), FZ-0.35-R (squared diamonds). We have used gas and star particles within $1.5 \times r_{\rm opt}$ and a vertical distance of $|z| < 4\ h^{-1}$ kpc to define the disk and bulge components. The disk was assumed to be formed by particles with $r_{xy} > 2r_{\rm eff}$ and the bulge by particles with $r_{xy} < 2r_{\rm eff}$. The cross corresponds to the results for the dark matter halo which is similar in all simulations. The solid (dotted) area represents the observed values for for spirals (ellipticals).

that the bulge shape parameters obtained in all simulations with SN energy feedback are $n \sim 1$, indicating that the bulges have approximately exponential profiles. From Table 6.2 we can also appreciate that SN energy feedback has produced bulge-to-disk ratios that are in better agreement with observations ($M_{\rm b}/M_{\rm d} \approx 0.3$ for the Milky Way), in comparison to the high value ($M_{\rm b}/M_{\rm d} = 1.35$) obtained for simulation DZ [1].

In order to study in more detail the properties of the simulated galaxies, we select simulation FZ-0.5 which has a well-formed disk with scalelength $r_{\rm d} = 3.29\ h^{-1}$kpc. This simulation has produced a galaxy with a bulge-to-disk ratio ($M_{\rm b}/M_{\rm d} = 0.77$)

[1] We have used Eqs. D.1 and D.2 of Appendix D to estimate these values. A note of caution should be made in relation to these estimations since different criteria can be used to quantify bulge and disk masses.

Table 6.2: Parameters obtained from bulge-disk decompositions to the simulated galaxies: disk scalelength ($r_{\rm d}$), bulge scalelength ($r_{\rm b}$), bulge effective radius ($r_{\rm eff}$), bulge parameter ($n$), disk central surface mass density ($\Sigma^0_{\rm d}$), bulge central surface mass density ($\Sigma^0_{\rm b}$), disk mass ($M_{\rm d}$), bulge mass ($M_{\rm b}$) and bulge-to-disk ratio ($M_{\rm b}/M_{\rm d}$).

| Test | $r_{\rm d}$ | $r_{\rm b}$ | $r_{\rm eff}$ | $n$ | $\Sigma^0_{\rm d}$ | $\Sigma^0_{\rm b}$ | $M_{\rm d}$ | $M_{\rm b}$ | $M_{\rm b}/M_{\rm d}$ |
|---|---|---|---|---|---|---|---|---|---|
| DZ | 2.31 | 1.00 | 1.70 | 1.01 | 0.183 | 1.31 | 6.14 | 8.31 | 1.35 |
| FZ-0.3 | 2.04 | 1.05 | 1.55 | 0.92 | 0.064 | 0.38 | 1.67 | 2.29 | 1.38 |
| FZ-0.5 | 3.29 | 1.12 | 2.08 | 1.06 | 0.055 | 0.33 | 3.71 | 2.88 | 0.77 |
| FZ-0.75 | 2.59 | 1.05 | 2.85 | 1.26 | 0.114 | 0.31 | 4.80 | 3.63 | 0.76 |
| FZ-0.9 | 4.99 | 1.01 | 2.29 | 1.17 | 0.032 | 0.30 | 5.02 | 2.72 | 0.54 |
| FZ-0.35-R | 3.65 | 1.42 | 2.66 | 1.06 | 0.080 | 0.35 | 6.71 | 4.96 | 0.74 |

and, as we will show later on, the chemical properties of its different components are in global agreement with observations. In Fig. 6.14 we show the face-on and edge-on maps of the stellar mass density at redshift $z = 0$ for the analysed galaxy. From these maps, we can appreciate the morphology of the galaxy, which clearly shows the existence of a a well-defined disk-like structure, in contrast to the morphology of the simulated galaxy shown in Fig. 3.7 (Chapter 3) where no SN energy feedback has been included.

## 6.3 A MILKY WAY-TYPE GALAXY

As we have shown in the previous section, test FZ-0.5 has produced a galaxy with a well-formed disk configuration and structural parameters in agreement with those found for normal spiral galaxies (e.g. MacArthur, Courteau & Hotltzman 2002). In this Section, we analyse the formation process for this galaxy and its chemical properties. We also qualitatively describe the outflows and metallicity transport driven by SN explosions in this simulation.

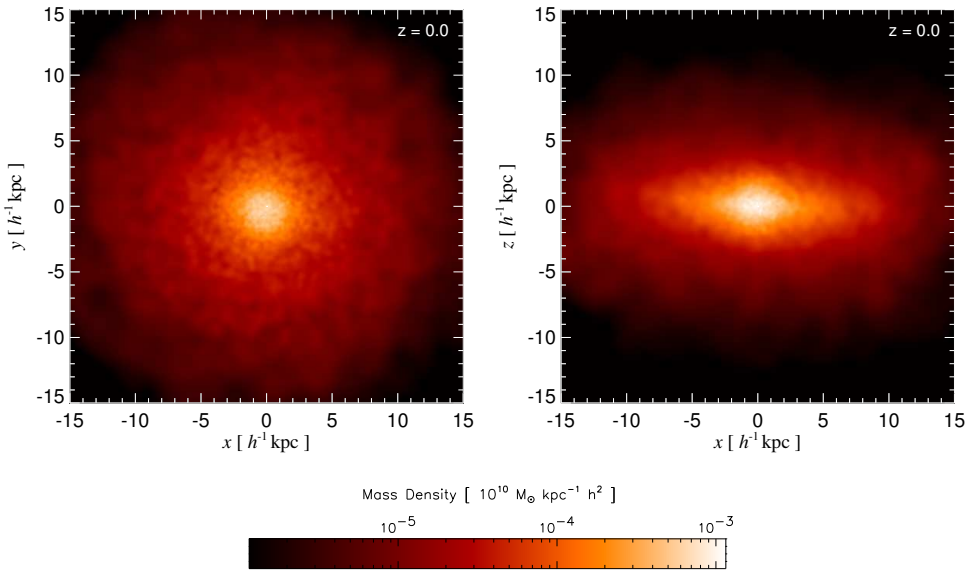


Figure 6.14: Face-on (left panel) and edge-on (right panel) projections of the stellar mass density of the simulated galaxy in our test FZ-0.5 run with SN energy feedback. The density scale is also shown.

### 6.3.1 THE FORMATION PROCESS

In order to compare the evolutionary process of the simulated galaxy in test FZ-0.5 with that of DZ run without energy feedback (Chapter 3), in Figs. 6.15 to 6.17 we show the comoving distribution of dark matter, gas and star particles for a series of redshifts in FZ-0.5. The plotted distributions for all redshifts correspond to those particles which, at redshift $z = 0$, are located within $1.5 \times r_{\rm opt}$ from the centre of the galaxy. From these figures we can appreciate how the dark matter and baryonic components grow through their hierarchical assembly. As dark matter aggregates into progressively larger clumps, the gas cools and condenses within these dark matter haloes, giving rise to the formation of stars in the central regions. As a result of this evolution, the distribution becomes more concentrated with time. Note the existence of a diffuse gas component which is the result of SN energy feedback that heats up material in the central regions. This gas expands forming a diffuse, extended component around the galaxy.

If we compare these figures with those obtained for our test DZ (Figs. 3.2, 3.3 and 3.4 in Chapter 3), several clear differences arise. When SN energy feedback is included, the dark matter clumps are less concentrated, and there is a significant larger amount of diffuse gas. The smallest structures formed in test DZ are not

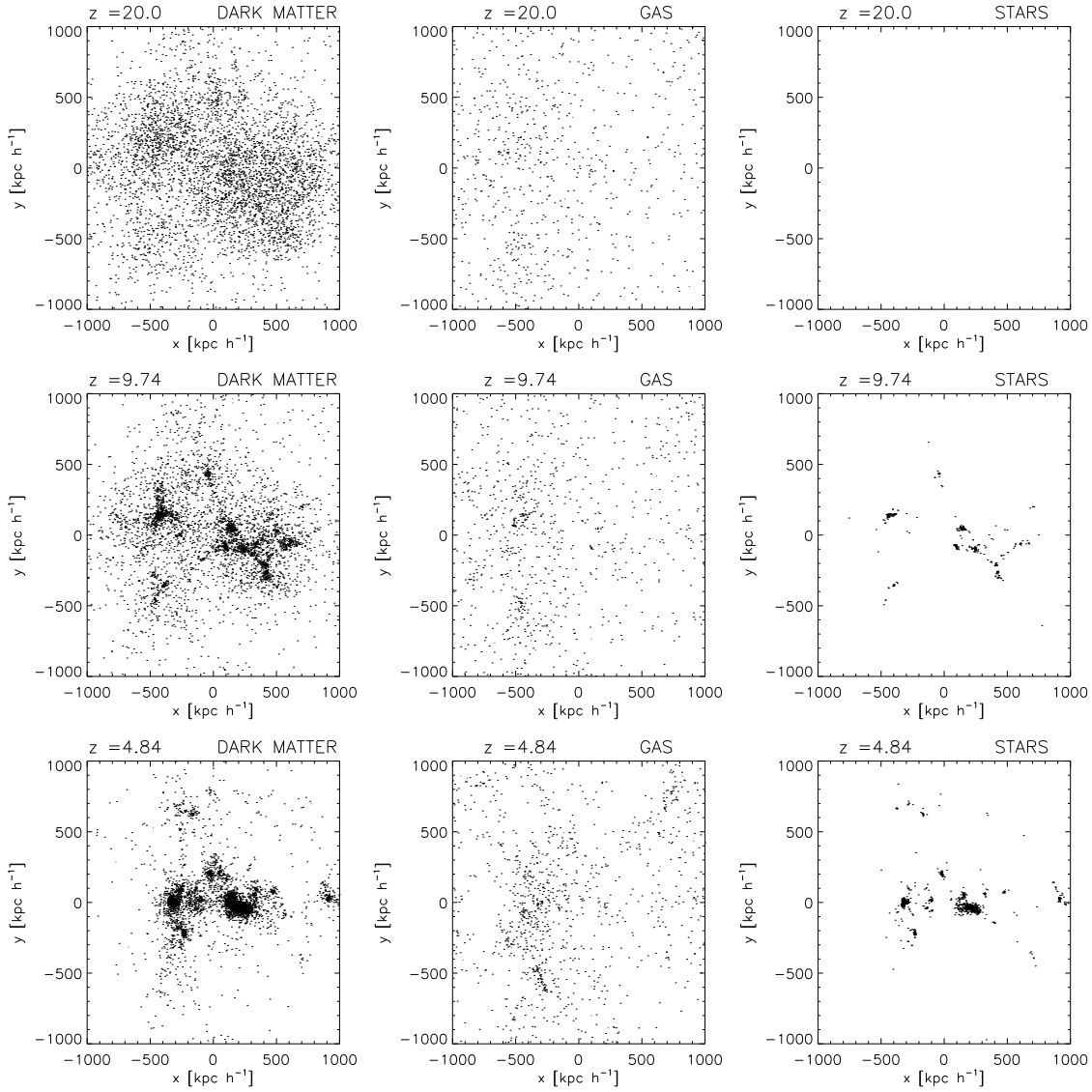


Figure 6.15: Comoving distribution of dark matter, gas and star particles located within $1.5 \times r_{\rm opt}$ at redshift $z = 0$, in our test FZ-0.5. The different rows correspond to the indicated redshifts.

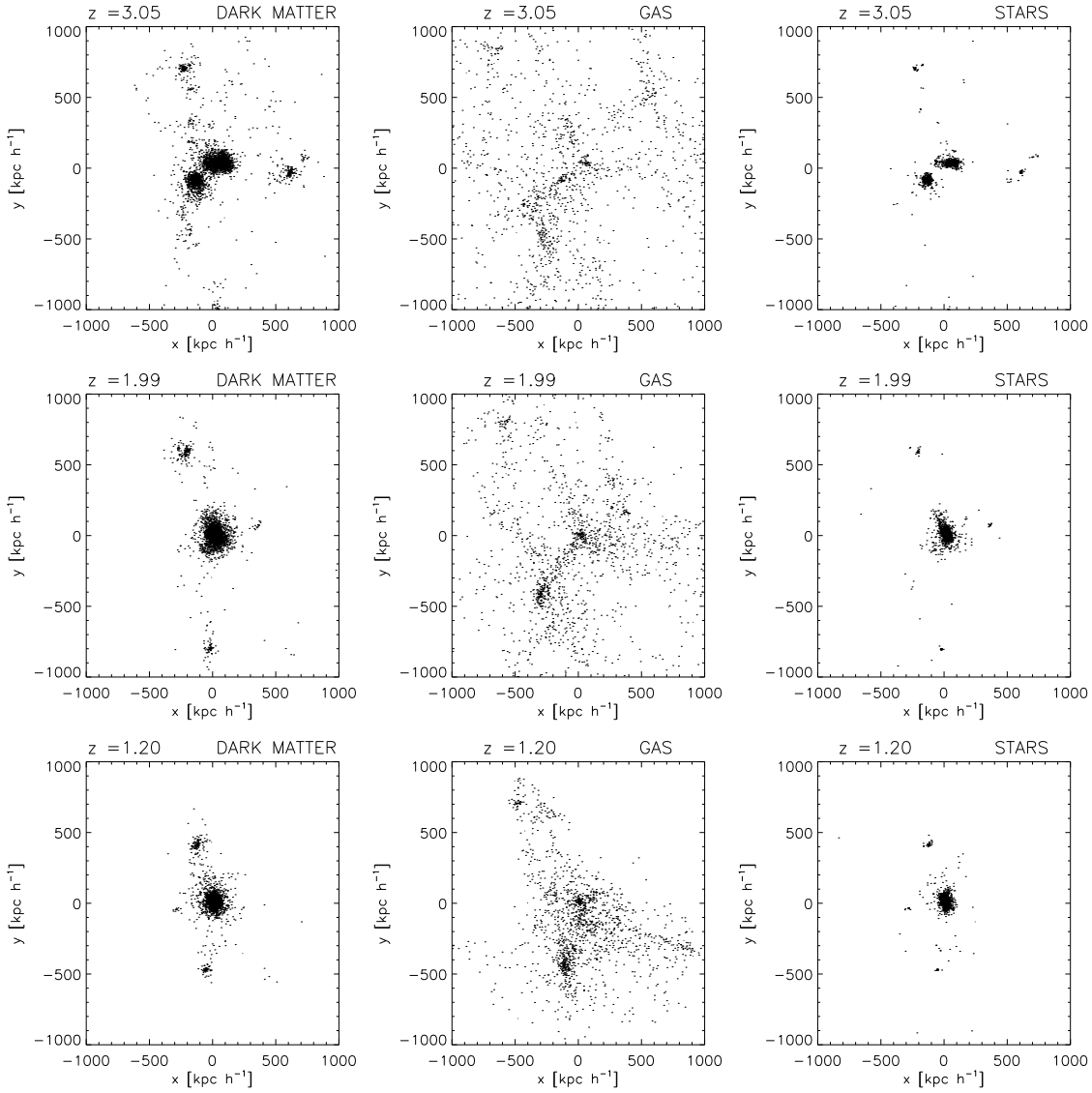


Figure 6.16: Comoving distribution of dark matter, gas and star particles located within $1.5 \times r_{\rm opt}$ at redshift $z = 0$, in our test FZ-0.5. The different rows correspond to the indicated redshifts.

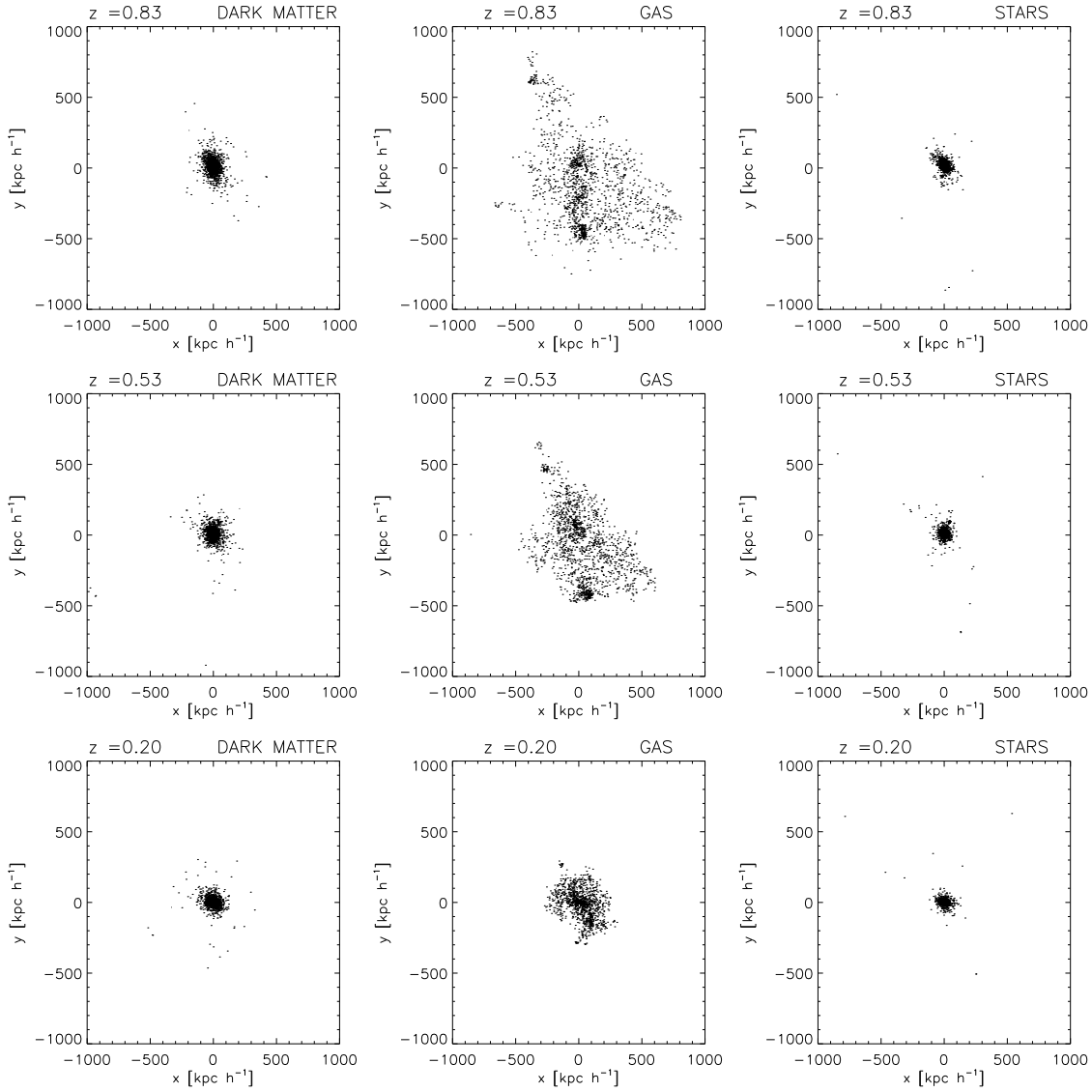


Figure 6.17: Comoving distribution of dark matter, gas and star particles located within $1.5 \times r_{\rm opt}$ at redshift $z = 0$, in our test FZ-0.5. The different rows correspond to the indicated redshifts.

present in FZ-0.5. These small structures have shallow potential wells and in the first stages of their evolution, the SN energy ejected as the result of the formation of the first stars triggers strong outflows which contribute to delay the condensation and collapse of the surrounding gas. On its turn, the effects of SN energy feedback on the baryonic components of these small structures translate into the dark matter potential wells. As a consequence of the changes in the dark matter and baryonic distributions produced by the inclusion of the SN energy feedback model, the formation of many small stellar clumps present in DZ has been prevented in FZ-0.5.

### 6.3.2 STELLAR AGE DISTRIBUTIONS

In this Section we compare the stellar age distribution of our simulated galaxy with observational results of the Milky Way. For this purpose, we separate the stellar matter in our simulation into four different components: a thin disk, a thick disk, a bulge and a stellar halo. In order to select stars which trace the main properties of these components, particles were selected as follows: the bulge component is assumed to be formed by stars within a radial distance of $r < 1.5r_{\rm eff}$, the thin disk by stars with $1.5r_{\rm eff} < r < 3.2r_{\rm d}$ [2] and a vertical distance over the disk plane of $|z| < 0.5\ h^{-1}$ kpc (similiar to the value for the thin disk of the Milky Way), the thick disk by stars with $1.5r_{\rm eff} < r < 3.2r_{\rm d}$ and a vertical distance over the disk plane in the range $0.5\ h^{-1}$ kpc $< |z| < 6\ h^{-1}$, and the stellar halo is traced by stars with $|z| > 8\ h^{-1}$ kpc. Recall that our results are not sensitive to the exact definitions for the different components, provided they are reasonably well chosen to trace their main properties. Note that in test DZ (Chapter 3), we were not able to segregate stars into four distinct components because of the nearly absence of extended disks. For the other tests run with SN energy feedback, the stellar age distributions only change slightly in relation to the results obtained for FZ-0.5.

We show in Fig. 6.18 the stellar mass fraction as a function of stellar age for the four components defined above for our test FZ-0.5. In the upper panel we show the results for the disk-like components (i.e. thin and thick disks) while in the lower panel results for the spheroidal configurations (i.e. bulge and stellar halo) are plotted. The stellar age distributions for the disk components show that stars in the disks spread a wide range in stellar ages, from the first epochs to the more recent ones. The main difference between the distributions of these components is that stars in the thick disk show a trend to be older, in comparison to those of the thin disk. In particular, we find that 70% of stars in the thin disk are younger than $7\ h^{-1}$ Gyr while this percentage decreases to 55% for stars in the thick disk. The fact that an important fraction of the disk stars are relatively young demonstrates the ability

[2] In a purely exponential disk, the radius $3.2r_{\rm d}$ encloses 83% of the disk mass.

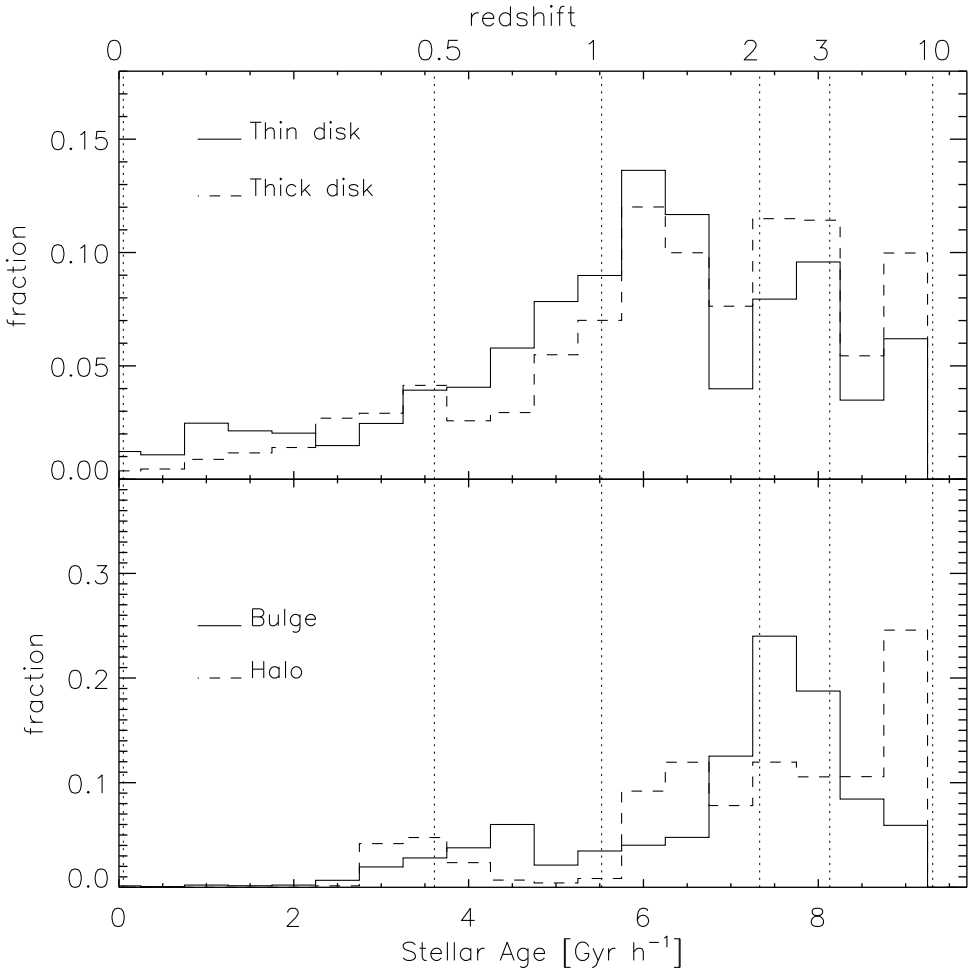


Figure 6.18: Fraction of stellar mass as a function of stellar age for our test FZ-0.5 run with feedback input parameter $\epsilon_c = 0.5$. All stars within a radial distance $r < 2 \times r_{\rm opt}$ at redshift $z = 0$ are shown, segregated according to radial ($r$) and vertical ($z$) distance into bulge ($r < 1.5 r_{\rm eff}$), thin disk ($1.5 r_{\rm eff} < r < 3.2 r_{\rm d}$ and $|z| < 0.5\ h^{-1}$ kpc), thick disk ($1.5 r_{\rm eff} < r < 3.2 r_{\rm d}$ and $0.5\ h^{-1}$ kpc $< |z| < 6\ h^{-1}$), and stellar halo ($|z| > 8\ h^{-1}$ kpc.)

of our SN energy feedback model to regulate the star formation activity allowing later, recent star formation episodes. In contrast, for test DZ we found that only 24% of all stars in the system have stellar ages $t < 7\ h^{-1}$ Gyr in open contradiction with observations (Liu & Chaboyer 2000; Nordstrom et al. 2004).

The spheroidal components have different properties compared to the disk configurations. We find that the distributions for both the bulge and the stellar halo components are shifted towards older stellar ages. Note that there are almost no stars formed in these components in the last $\sim 3\ h^{-1}$ Gyr (stellar ages $< 3\ h^{-1}$ Gyr). For both components, there is a $\sim 70\%$ of the stars with stellar ages larger than $7\ h^{-1}$ Gyr. Observationally, it is found that the galactic bulge is mainly old (Rich 2001). In agreement with our previous results, these findings suggest that SN energy feedback contributes to the formation of systems which are in better agreement with the properties of observed spiral galaxies.

### 6.3.3 CHEMICAL PROPERTIES

As we mentioned before, the requirement of reproducing both the dynamical and chemical properties of each component of a Milky Way type galaxy is a challenging task. In order to compare the chemical properties of the different components of the simulated galaxy in FZ-0.5 with observations, in Fig. 6.19 we show the stellar mass fraction as a function of iron abundance for stars in FZ-0.5, at redshift $z = 0$. In the upper panel we show the results for disk-like configurations (i.e. thin and thick disks) and in the lower panel, the corresponding distributions for spheroidal-like ones (i.e bulge and stellar halo), as defined in the previous section. If we compare the distributions for the thin and the thick disk, we find that stars in the thin disk show a trend to be more metal-rich than stars in the thick disk. In particular, we find that 29% of the thin disk stars have [Fe/H] $< -0.8$ while this percentage is 41% for the stellar mass in the thick disk. Observationally, it is found that the iron abundance of the thin disk of the Milky Way peaks at [Fe/H] $\sim -0.2$ dex (Nordstrom et al. 2004), while the thick disk stellar mass has metallicity in the range [Fe/H] $\sim [-2.2, 0.5]$ dex with a peak at [Fe/H] $\sim -0.6$ dex (Chiba & Beers 2000). Our results for the thick disk agree better with these observations than those for the thin disk, where the distribution peaks at a lower metallicity in comparison to the distribution for Milky Way stars. Note that for test DZ without SN energy feedback we have found that the disk component presented a distribution with a peak at a too high value ([Fe/H] $\sim +0.3$ dex), in open disagreement with observational results of the Milky Way.

The results for the bulge component show that the metallicity distribution peaks at $<$ [Fe/H] $>\sim -0.5$ dex. This is consistent with observations in bulge stars of the Milky Way galaxy which show a peak in iron abundance at [Fe/H] $\sim -0.3$ dex with a long tail towards [Fe/H] $\sim -1$ dex (Zoccali et al. 2003). For the stellar halo

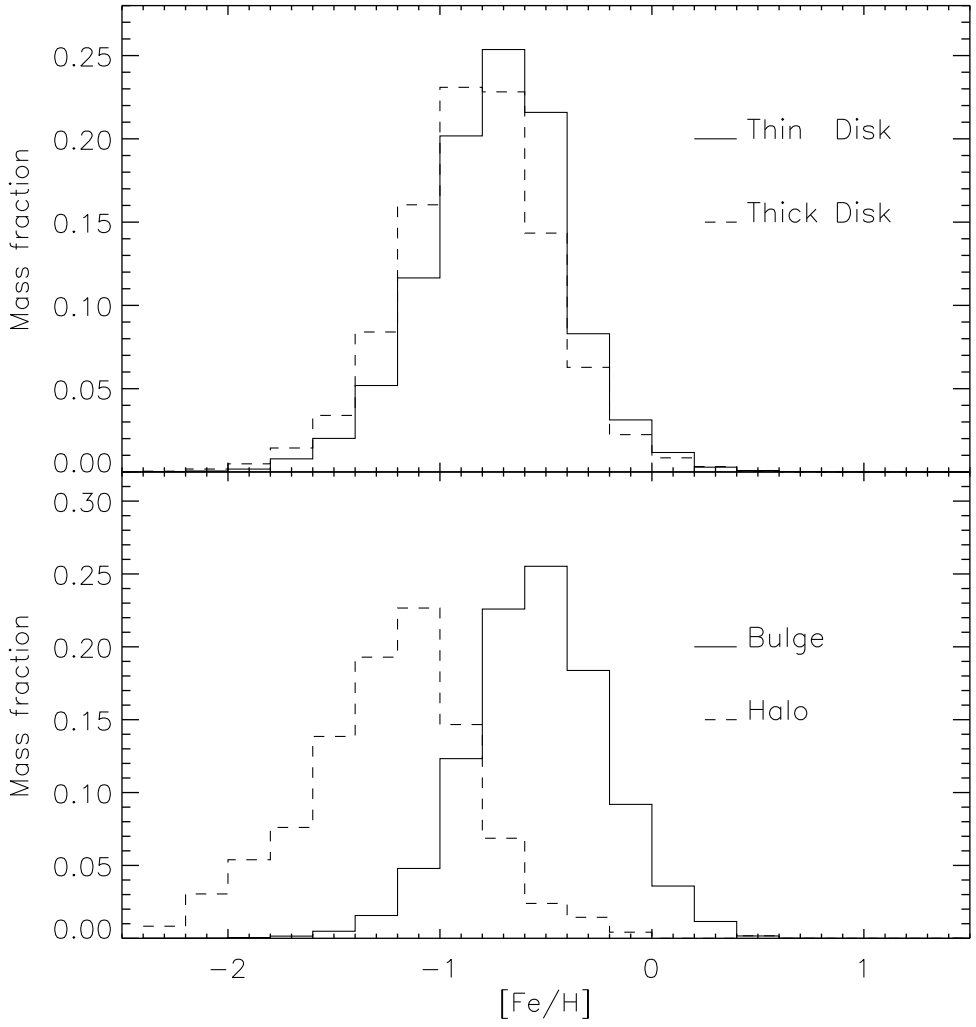


Figure 6.19: Fraction of stellar mass as a function of stellar metallicity for our test FZ-0.5 run with feedback input parameter $\epsilon_c = 0.5$. All stars within radial distance $r < 2 \times r_{\rm opt}$ at redshift $z = 0$ are shown, segregated according to radial ($r$) and vertical ($z$) distance into bulge ($r < 1.5 r_{\rm eff}$), thin disk ($1.5 r_{\rm eff} < r < 3.2 r_{\rm d}$ and $|z| < 0.5\ h^{-1}$ kpc), thick disk ($1.5 r_{\rm eff} < r < 3.2 r_{\rm d}$ and $0.5\ h^{-1}$ kpc $< |z| < 6\ h^{-1}$), and stellar halo ($|z| > 8\ h^{-1}$ kpc.)

component, we find a distribution that peaks at $< [\mathrm{Fe/H}] >\sim -1.1$ dex, showing that this component is, on average, less chemically enriched than the bulge and disk components, in agreement with observations. In the Milky Way, stellar halo stars show iron abundances in the range $[\mathrm{Fe/H}] \sim [-2.4, -0.6]$ dex (Chiba & Beers 2000). In particular, the fraction of stellar mass with $[\mathrm{Fe/H}] < -0.8$ for bulge and stellar halo stars is 12% and 83%, respectively. Note that for test DZ (run without SN energy feedbak), we found that stars in the stellar halo component had too high metallicities with a peak at $[\mathrm{Fe/H}] \sim +0.3$ dex, in disagreement with observations. An important result of our model is that it has been able to produce two spheroidal components with different chemical characteristics, the bulge and the stellar halo, and that their chemical properties agree quite well with observational trends.

Finally, in Fig. 6.20 we show stellar (upper panel) and gaseous (lower panel) oxygen profiles for our test DZ (dashed lines), as well as for test FZ-0.5 (solid lines), at redshift $z = 0$. For all relations, the standard deviations are similar, of the order of 0.5 dex. In the case of the stellar profiles, we can observe that the relations for both simulations have similar slopes (linear fits in the inner $3.2r_{\mathrm{d}}$ for each galaxy give slopes of $-0.027 \pm 0.006$ dex kpc$^{-1}$ for DZ and $-0.033 \pm 0.005$ dex kpc$^{-1}$ for FZ-0.5), but in DZ there is a shift towards higher abundances. This is reflected in the zero points obtained performing linear fits to the relations, which yield values of $12 + \log(\mathrm{O/H})|_0 = 8.78 \pm 0.03$ dex for DZ and $12 + \log(\mathrm{O/H})|_0 = 8.24 \pm 0.04$ dex for FZ-0.5.

The gaseous oxygen profiles show stronger differences. When we consider the effects of SN energy feedback, the oxygen abundance shows a smooth decrease with distance to the centre. Conversely, in test DZ we find that, although the gas has a relatively high oxygen abundance in the centre, it drops rapidly with distance. This is owing to the fact that there is only little gas left in this simulation and it is concentrated within the inner 4 $h^{-1}$ kpc (the gas mass fraction is $f_{\mathrm{gas}} = 0.026$). In addition, as SN energy feedback has not been included in DZ, the metals remain in the central regions where they are ejected in SN events, since there is no efficient mechanism to transport the metals outwards. We have performed linear fits to the relation found for FZ-0.5, obtaining a slope of $-0.014 \pm 0.007$ dex kpc$^{-1}$ and a zero point of $12 + \log(\mathrm{O/H})|_0 = 8.07 \pm 0.05$ dex. Note that for DZ, a linear fit is not a good representation of the data.

The results for the gaseous profiles can be compared with the observations of Zaritsky et al. (1994) for a sample of spiral galaxies. These authors find that most observed oxygen profiles have slopes in the range $[-0.06, -0.02]$ dex kpc$^{-1}$, while the zero-points are in the range $[8.6 - 9.4]$ dex. The results obtained for our test simulation FZ-0.5 run with SN energy feedback shows better agreement with these observations, in comparison to the results of test DZ without SN energy feedback. Note that test DZ has a too low zero-point and is steeper than the observed profiles. For FZ-0.5, the zero-point obtained is a bit lower than observed values. This could

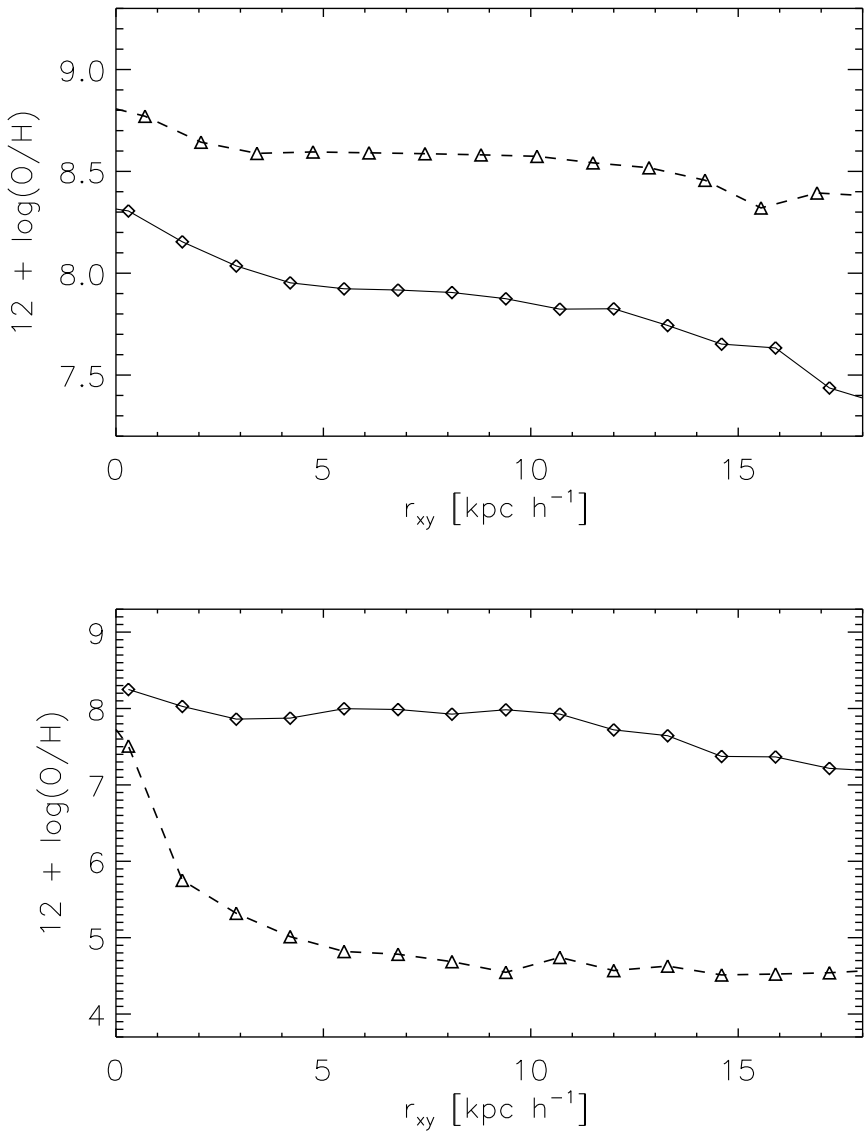


Figure 6.20: Oxygen profiles for the stellar (upper panel) and gaseous (lower panel) components in our test FZ-0.5 (solid lines), at redshift $z = 0$. For comparison, we also show the results obtained for test DZ (dashed lines) run without SN energy feedback.

indicate the need for a top-heavy IMF or a less efficient transportation of metals outwards (that could be tunned changing the input feedback parameter used for metal distribution). The fact that we have obtained metallicity profiles in pretty good agreement with observations show that our model for SN energy feedback is capable to consistently describe the dynamical and chemical properties of spiral galaxies altogether.

### 6.3.4 GAS FLOWS AND METALLICITY TRANSPORT

As we have already mentioned, one of the most relevant effect of SN energy feedback is the generation of galactic outflows which transport gas and metals from the centre of the systems into the intergalactic medium. In Chapters 4 and 5 we have used isolated disk galaxy models in order to show the ability of our SN energy feedback model in driving important galactic winds which transport a significant amount of metals into the outer regions of galaxies. In this Section, we describe the gas flows and metallicity transport driven by SN explosions in our test FZ-0.5 which has a more realistic initial condition.

In Figs. 6.21 to 6.24 we show face-on and edge-on stellar density maps for a series of different redshifts. These distributions correspond to projections parallel and perpendicular to the total angular momentum of the system, respectively. We also plot with arrows the velocity field of the stars in order to analyse the general dynamics of the system. For these plots, the colour reference is indicated in Fig. 6.24. From these figures we can appreciate that at redshifts higher than about $z = 1.5$, stars are located in a nearly spheroidal distribution and the disk has not yet formed at this early time. Note that at this redshift, the galaxy is suffering from the accretion of a satellite, which can be clearly seen in the distribution at redshift $z = 1.99$. From $z = 1.5$, we can see how a disk-like structure appears, where stars have a velocity field consistent with circular orbits onto the $xy$ plane. As time evolves, the stellar disk gets larger and better defined. Also note the presence of the bulge component which is concentrated in the very central regions of the galaxy. Note that the galaxy formed at redshift $z = 0$ has been feeded by satellites during its evolution, reflecting the hierarchical building up of the structure.

In Figs. 6.25 to 6.28 we show face-on and edge-on density maps for the gas component, as well as its velocity field, in test FZ-0.5, for different redshifts. The colour reference is indicated in Fig. 6.28. From these figures we can appreciate how the gas collapses and settles into a disk-like configuration as time evolves. In particular, at redshift $z = 1.5$, the gas shows an ordered rotation which indicates the presence of the disk. Note that spiral-like arms of high density can be formed. Also note that the velocity field of the gas is quite complex, since it is the result of several processes, such as radiative cooling, SN feedback, inflows and outflows. In particular, from the edge-on views it is clear that the gas can flow from the disk outwards, but

accretion of gas into the system also occurs. It is also important to remark that the gas component shows a clumpy density field, showing that gas clumps of different density can co-exist in nearly the same region. This is an important success of the model, related to our multiphase gas treatment.

As a result of the complex gas flows present in this simulation, non trivial chemical patterns develop. In Figs. 6.29 to 6.32 we show face-on and edge on gas metallicity maps for the same redshifts analysed in the previous figures, for test FZ-0.5. The velocity field of gas particles is also indicated by arrows. The colour reference for these plots is indicated in Fig. 6.32. From these figures we can appreciate how the gas flows help to enrich the intergalactic medium with metals. Recall that if there are no galactic winds generated, metals stay locked up into the inner regions of the galaxy where they are formed. This can be appreciated from Fig. 6.33 where we show the gas metallicity maps at redshift $z = 0$ for the galaxy in test DZ run without SN energy feedback. Comparing the results for DZ and FZ-0.5, it is clearly seen that SN energy feedback is capable of triggering the metal enrichment of the interstellar and intergalactic medium. This is a very important result since most simulations are not capable of reproducing the chemical enrichment of the IGM consistently, while observations suggest that this process is, in fact, related to SN feedback.

The findings obtained in this section have demonstrated the ability of our SN feedback model to reproduce the main chemical and dynamical features of disk galaxies in a self-consistent way. It is worth mentioning that our model does not include any scale dependent resolution parameter. This is one of the reasons for being able to describe the formation of a disk galaxy from its first epochs to the present time, consistently taking into account the effects of SN feedback in the evolving potential well. It is remarkable that our model succeeds in setting a self-regulated star formation process, in triggering strong mass-loaded outflows, and in enriching the IGM with metals. Our model is then a new and powerful tool to study galaxy formation on a more physical basis.

However, note that a lot of work still needs to be done (Scannapieco et al. 2006b, in preparation). Reproducing the Kennicutt law in cosmological simulations will allow to select the best fitting parameter for the star formation efficiency. Analysing in more detail the chemical and dynamical properties of the different components of disk galaxies such as our Milky Way will allow fine tunning our feedback input parameter which sets the percentage of SN energy dumped into the cold phase. This will also allow to select the best fitting Initial Mass Function. The ever growing data gathered from observations will also help to better constrain galaxy formation theories. The success of our model to reproduce the main aspects of the SN energy feedback process is a step forward to our understanding of the formation and evolution of galaxies.

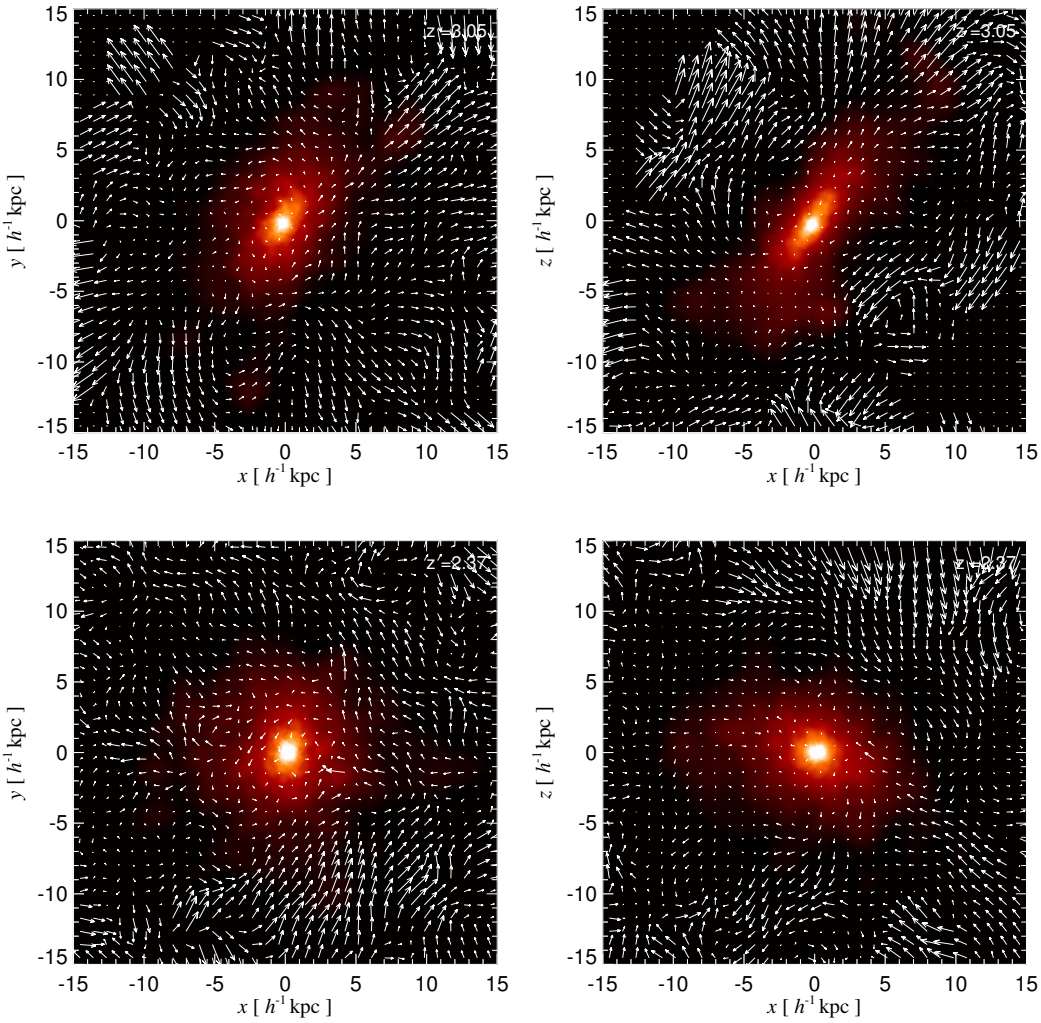


Figure 6.21: Face-on (left panels) and edge-on (right panels) maps of stellar density for our test FZ-0.5. The arrows map the velocity field of the stellar component. The different rows correspond to the indicated redshifts.

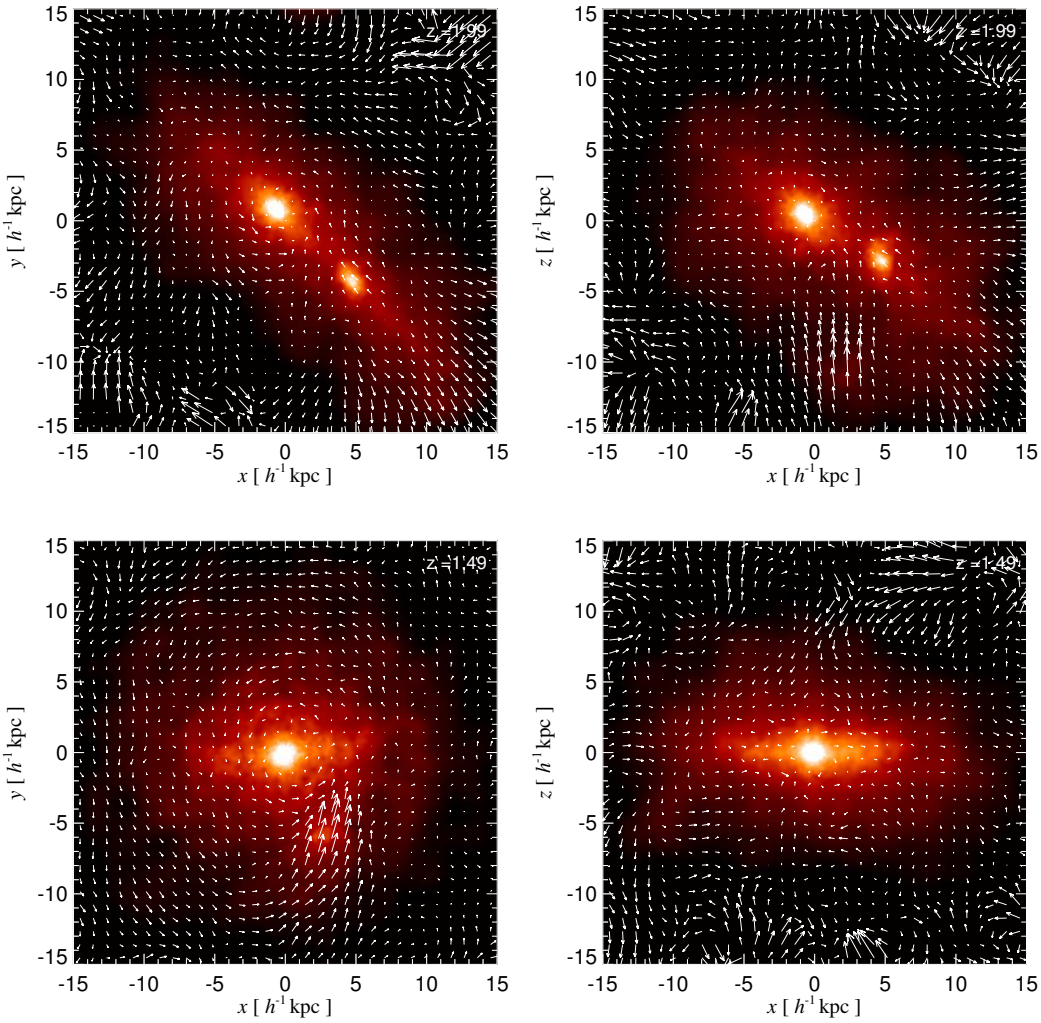


Figure 6.22: Face-on (left panels) and edge-on (right panels) maps of stellar density for our test FZ-0.5. The arrows map the velocity field of the stellar component. The different rows correspond to the indicated redshifts.

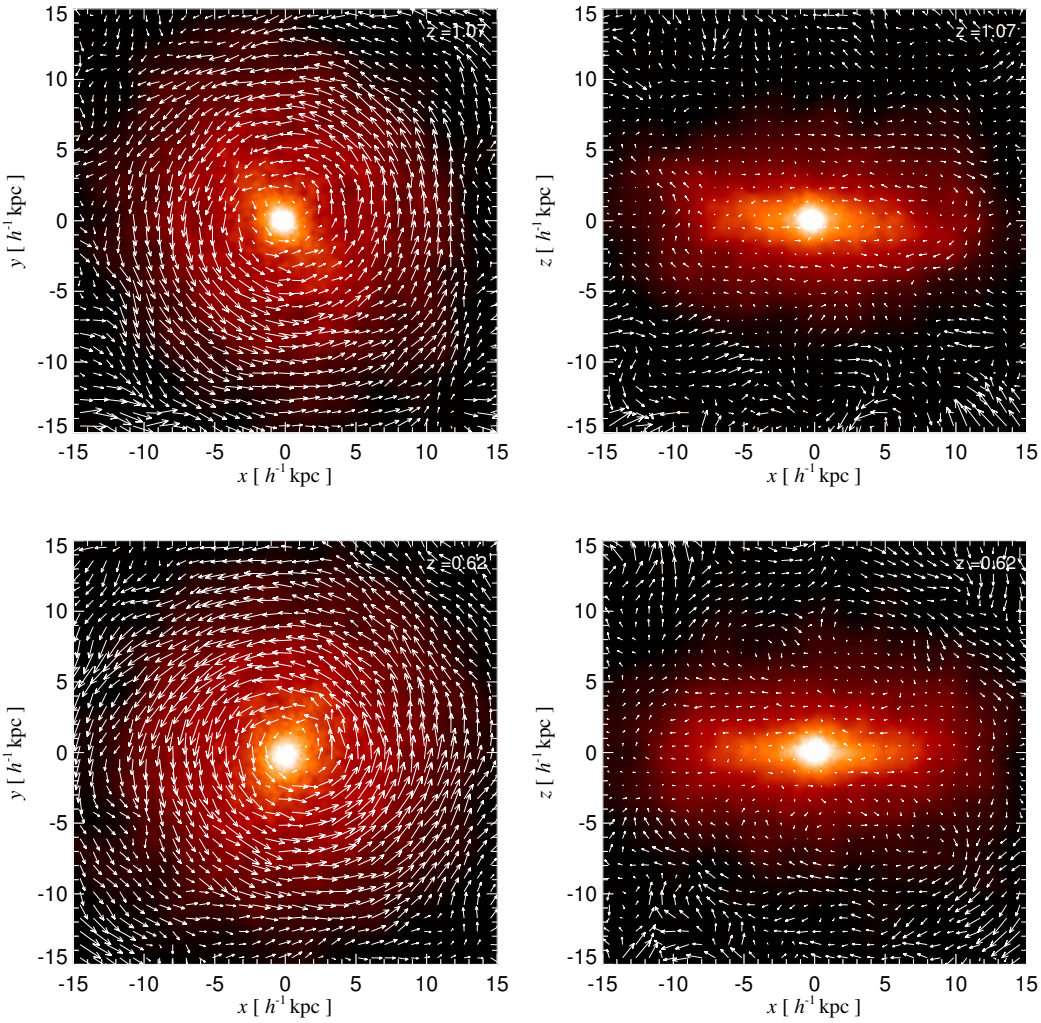


Figure 6.23: Face-on (left panels) and edge-on (right panels) maps of stellar density for our test FZ-0.5. The arrows map the velocity field of the stellar component. The different rows correspond to the indicated redshifts.

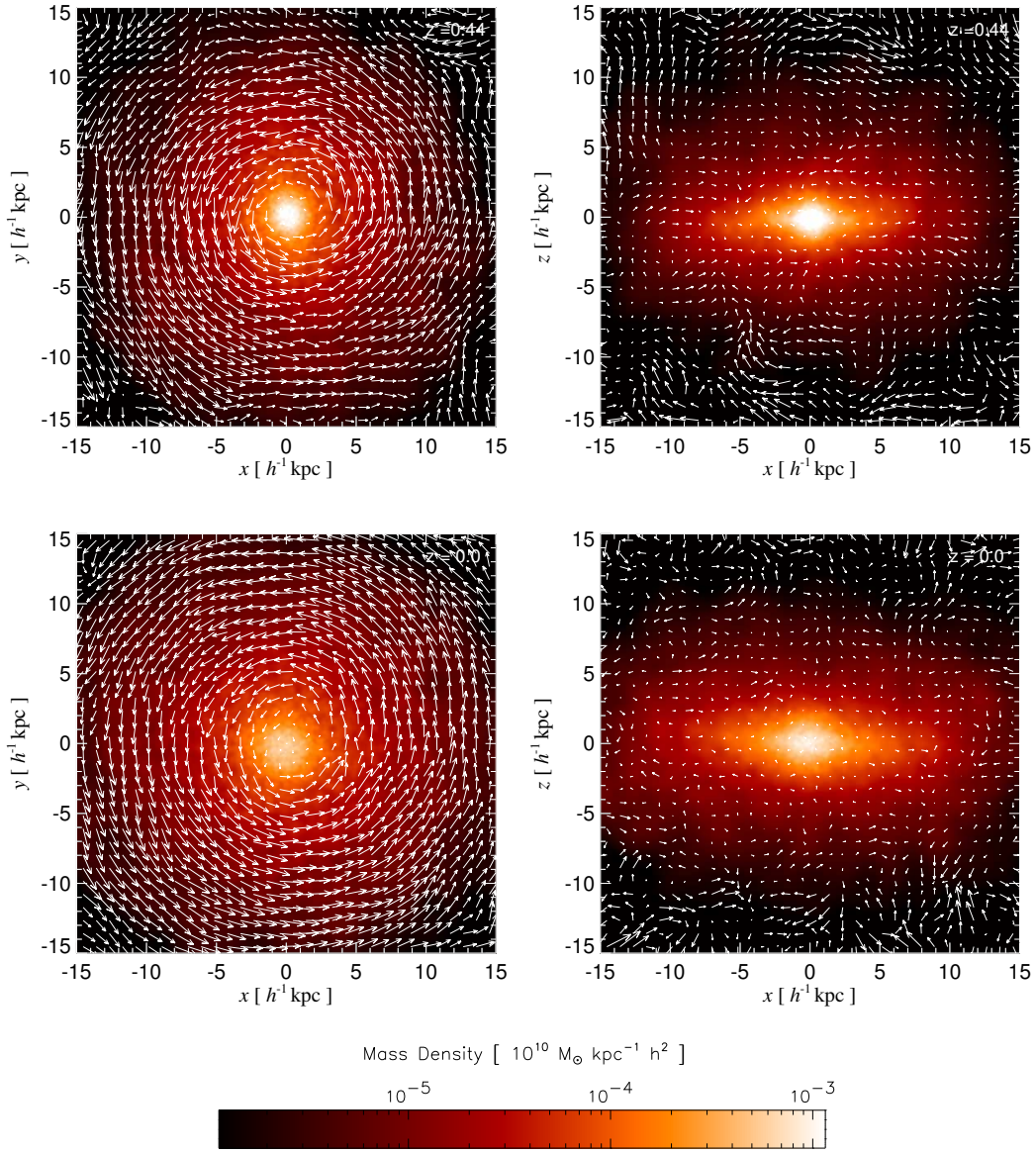


Figure 6.24: Face-on (left panels) and edge-on (right panels) maps of stellar density for our test FZ-0.5. The arrows map the velocity field of the stellar component. The different rows correspond to the indicated redshifts. The stellar density scale is also shown.

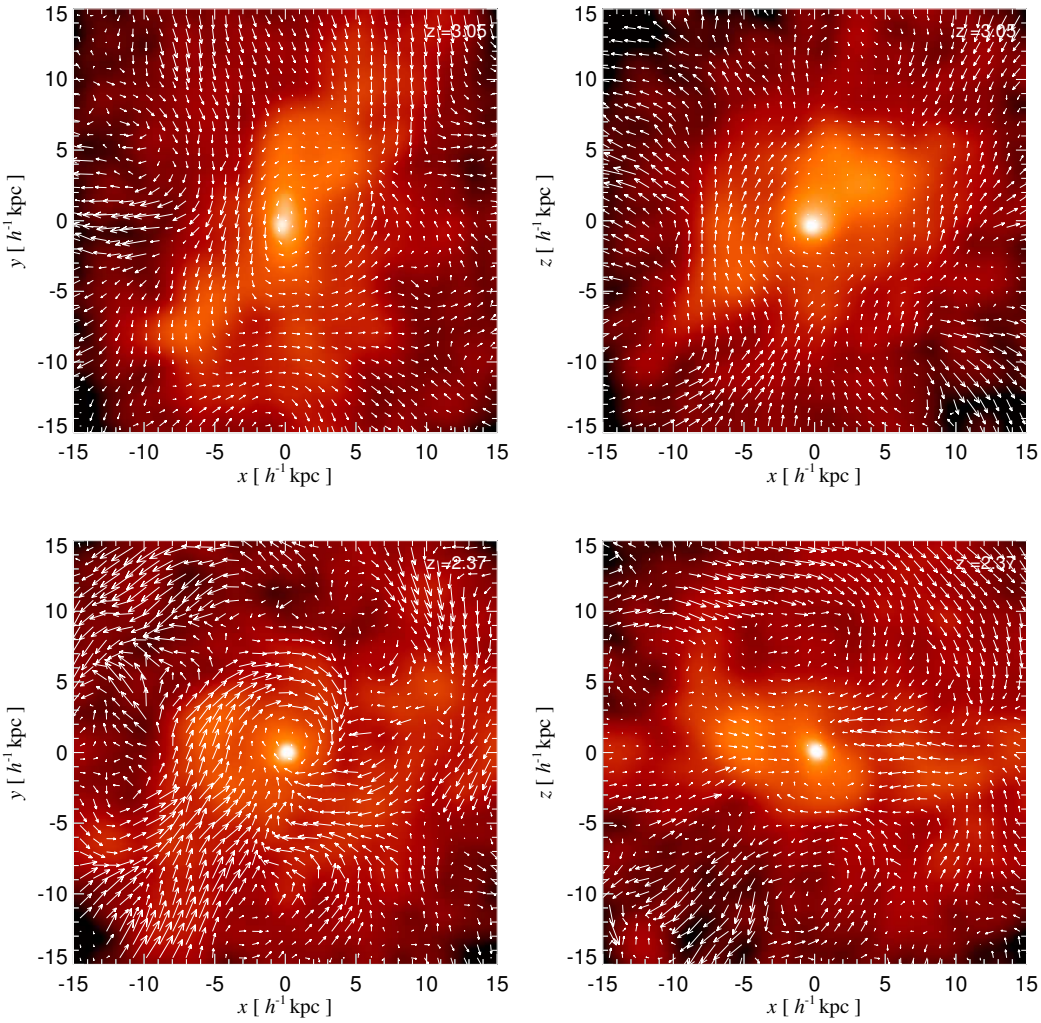


Figure 6.25: Face-on (left panels) and edge-on (right panels) maps of gas density for our test FZ-0.5. The arrows map the velocity field of the gas component. The different rows correspond to the indicated redshifts.

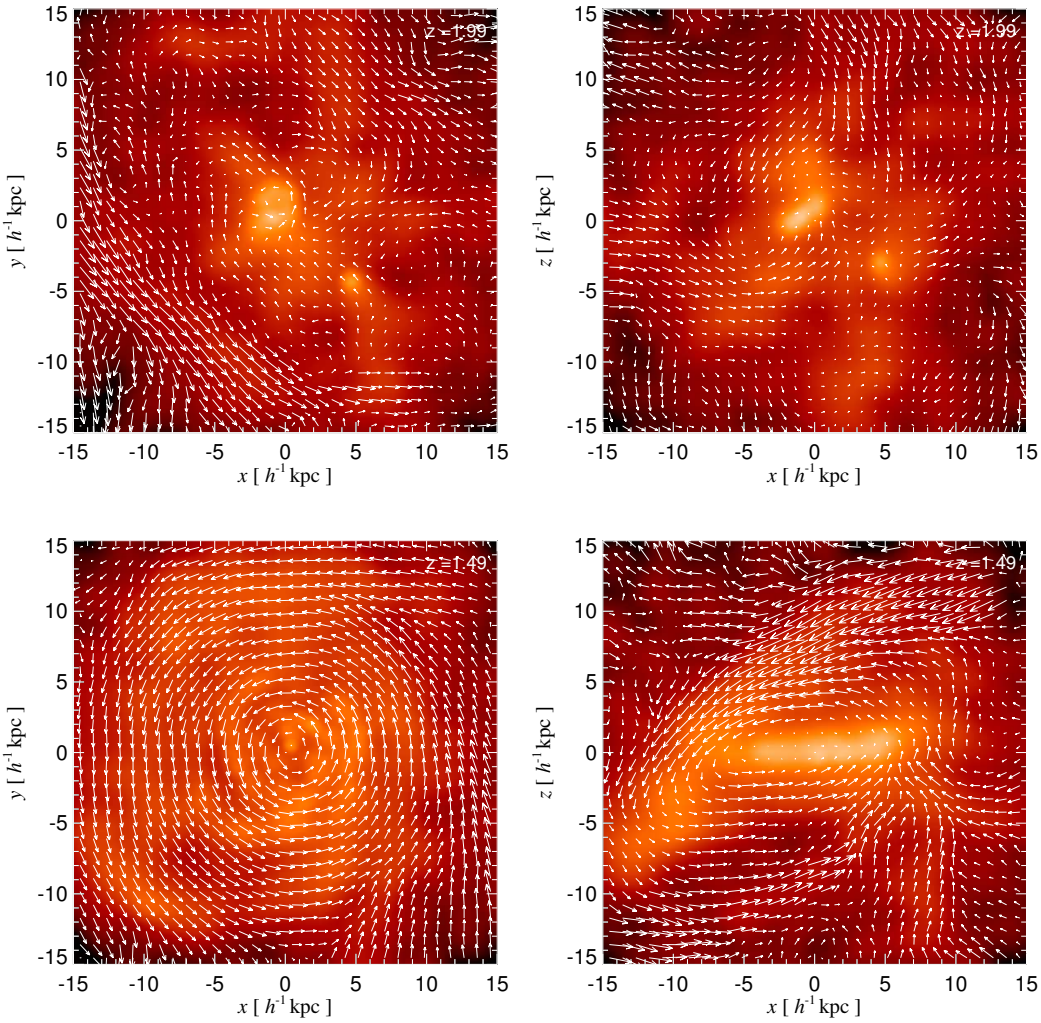


Figure 6.26: Face-on (left panels) and edge-on (right panels) maps of gas density for our test FZ-0.5. The arrows map the velocity field of the gas component.The different rows correspond to the indicated redshifts.

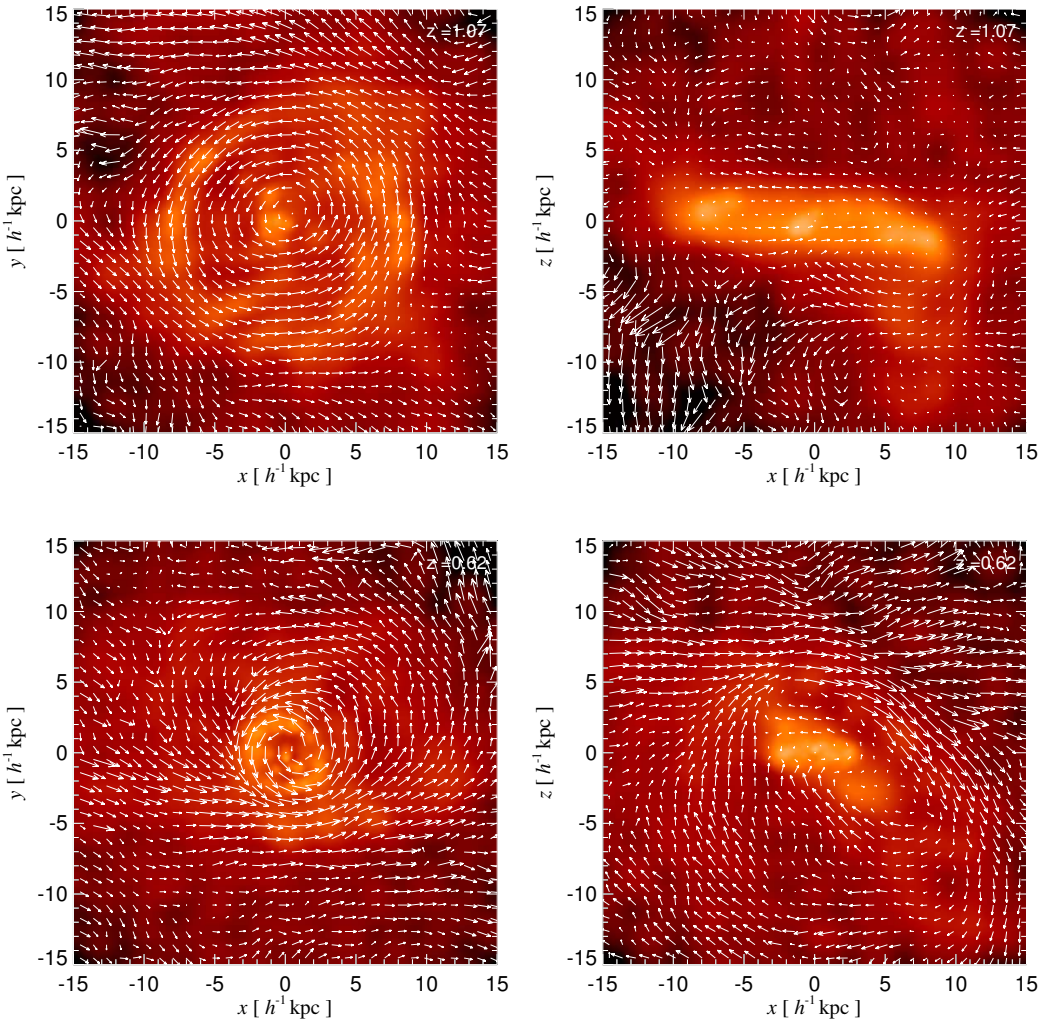


Figure 6.27: Face-on (left panels) and edge-on (right panels) maps of gas density for our test FZ-0.5. The different rows correspond to the indicated redshifts.

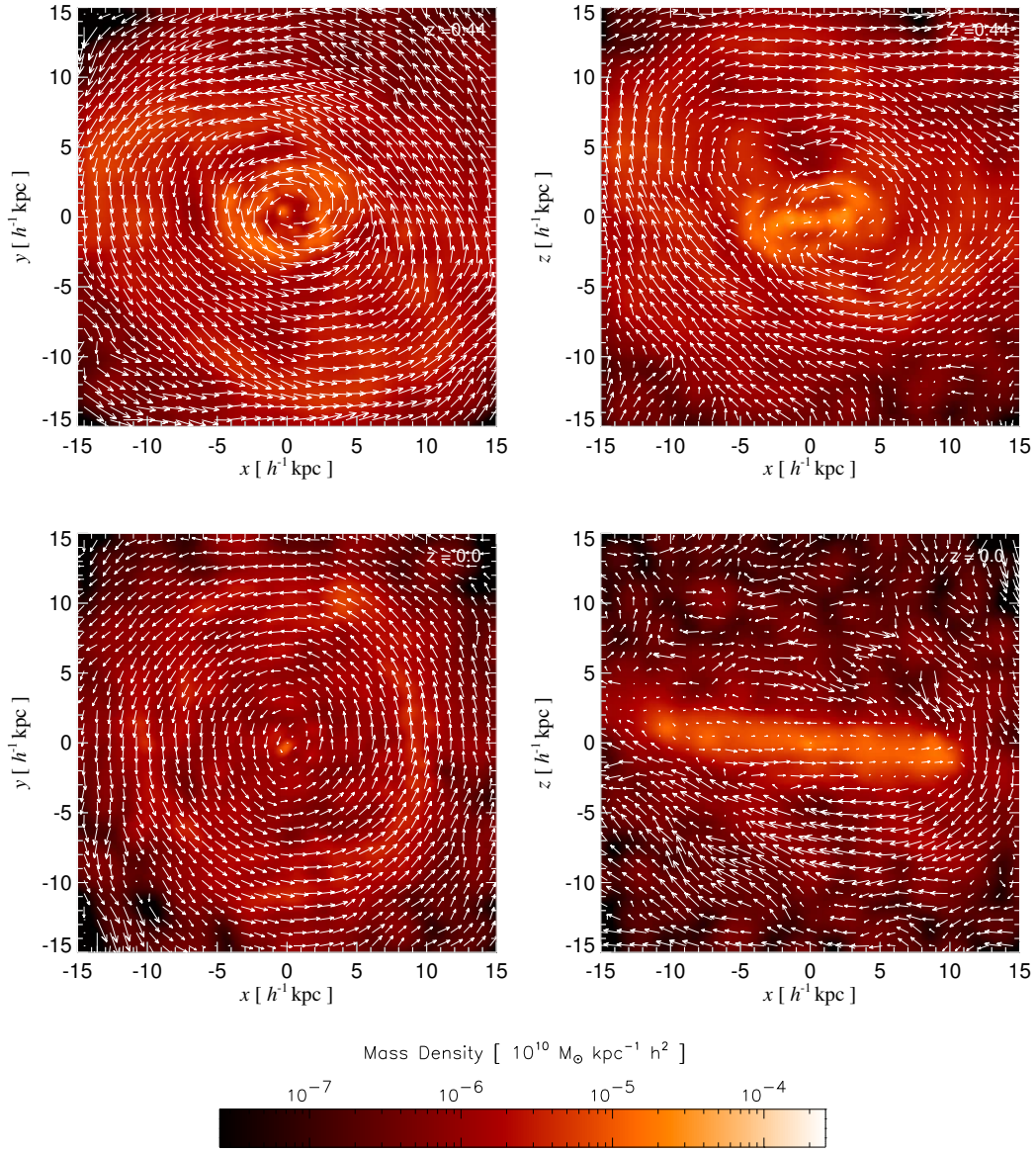


Figure 6.28: Face-on (left panels) and edge-on (right panels) maps of gas density for our test FZ-0.5. The arrows map the velocity field of the gas component. The different rows correspond to the indicated redshifts. The gas density scale is also shown.

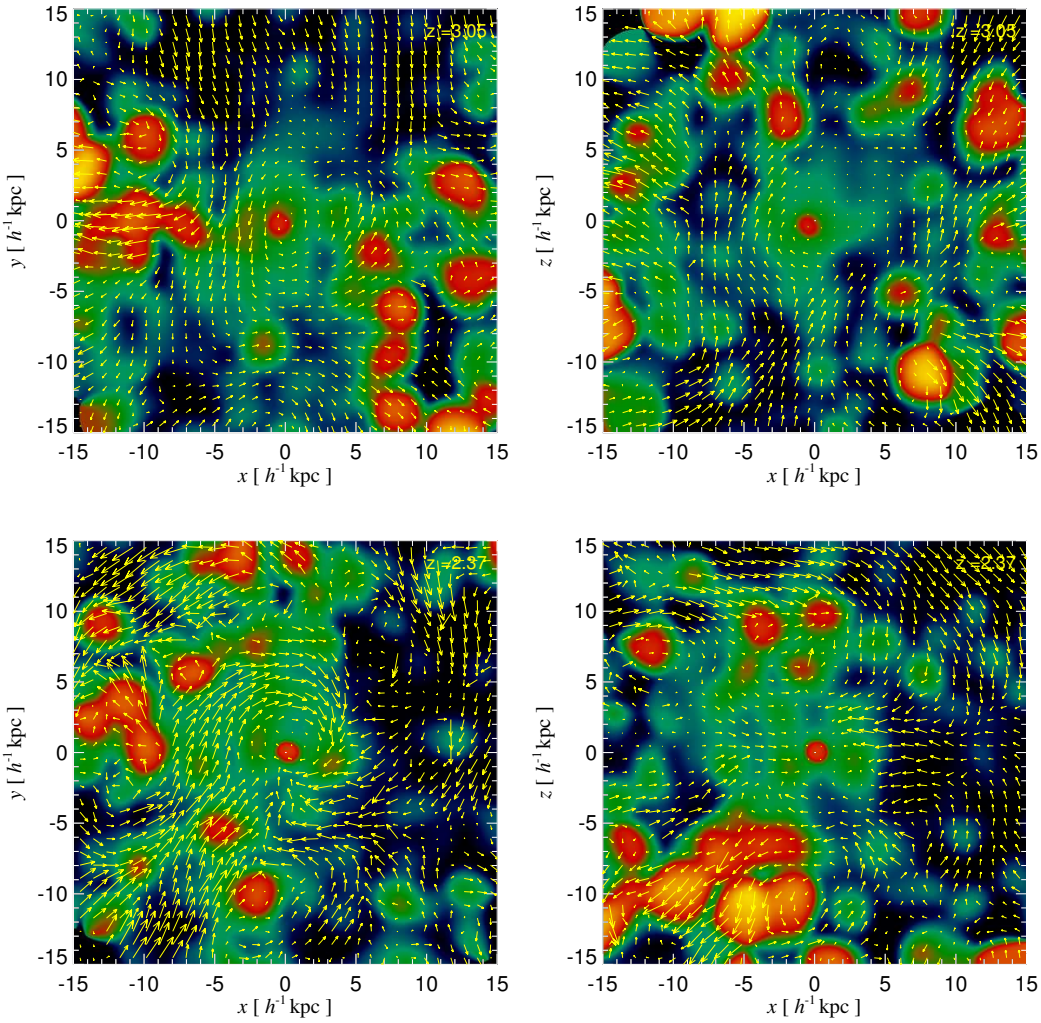


Figure 6.29: Face-on (left panels) and edge-on (right panels) maps of gas metallicity for our test FZ-0.5. The arrows map the velocity field of the gas component. The different rows correspond to the indicated redshifts.

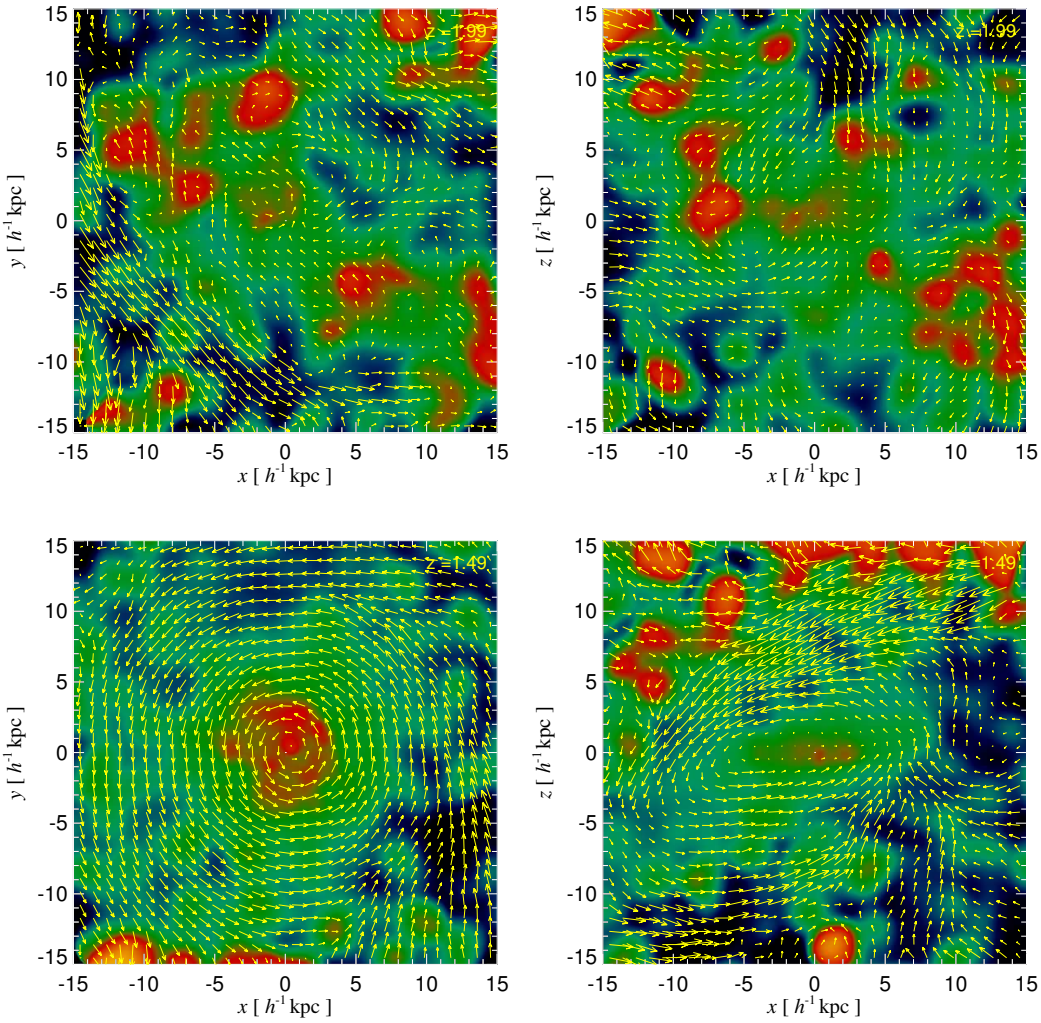


Figure 6.30: Face-on (left panels) and edge-on (right panels) maps of gas metallicity for our test FZ-0.5. The arrows map the velocity field of the gas component. The different rows correspond to the indicated redshifts.

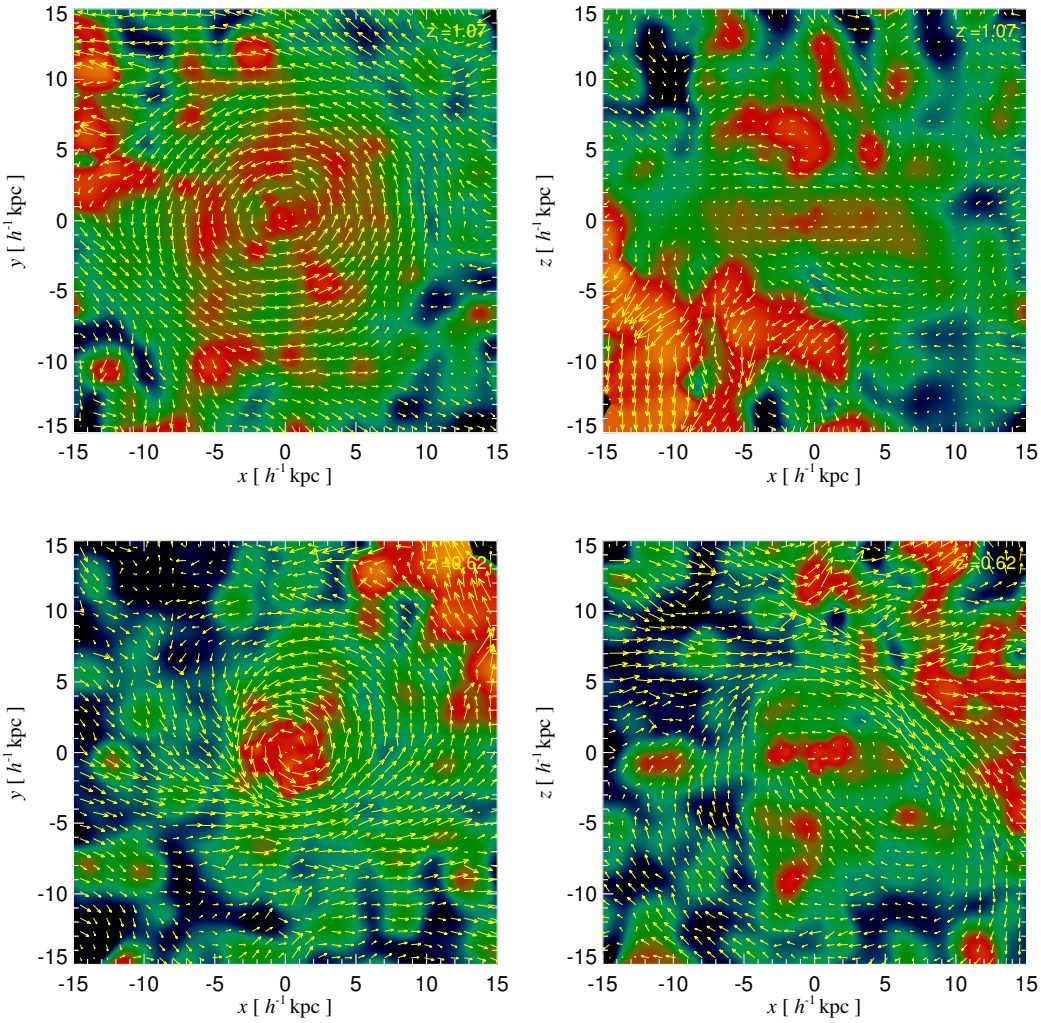


Figure 6.31: Face-on (left panels) and edge-on (right panels) maps of gas metallicity for our test FZ-0.5. The arrows map the velocity field of the gas component. The different rows correspond to the indicated redshifts.

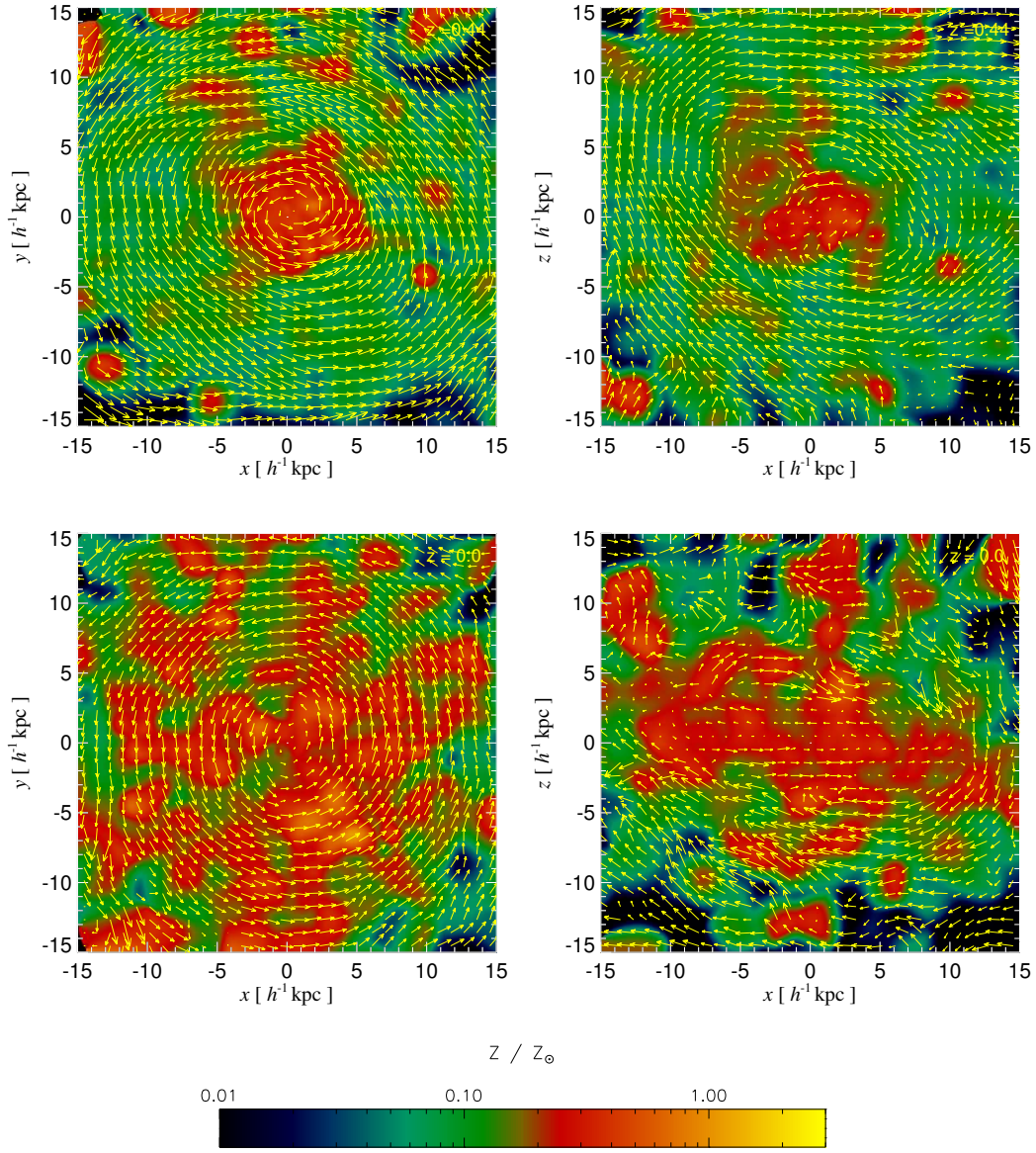


Figure 6.32: Face-on (left panels) and edge-on (right panels) maps of gas metallicity for our test FZ-0.5. The arrows map the velocity field of the gas component. The different rows correspond to the indicated redshifts. The metallicity scale is also shown.

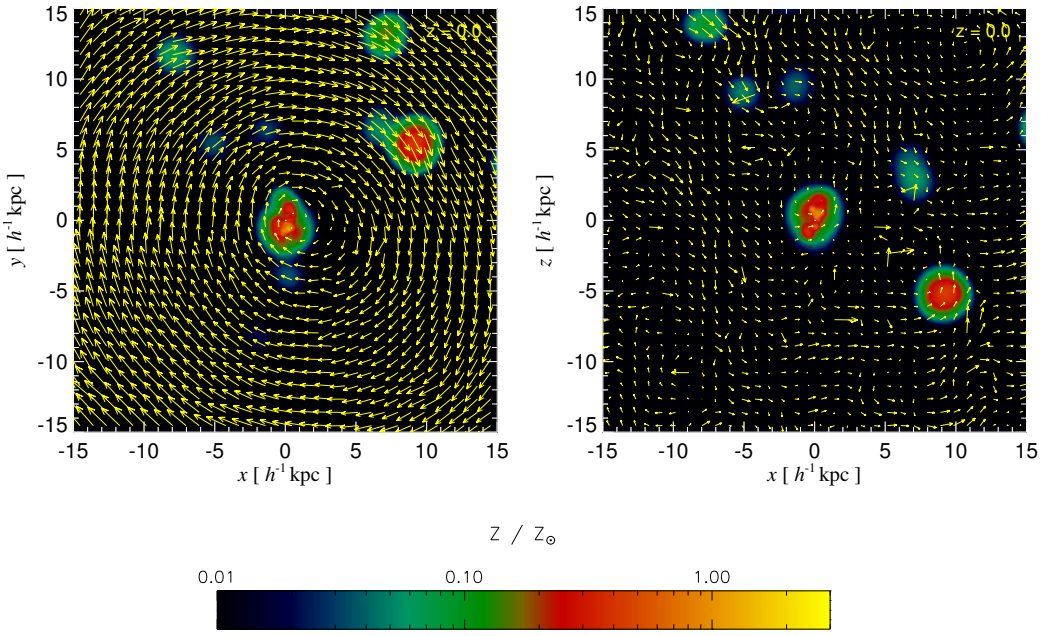


Figure 6.33: Face-on (left panels) and edge-on (right panels) maps of gas metallicity for our test DZ run without SN energy feedback, at redshift $z = 0$. The arrows map the velocity field of the gas component. The metallicity scale is also shown.

# Chapter 7

# Conclusions

This work has focused on the development of a new scheme to describe chemical and energy feedback by Supernovae (SN), in the context of numerical simulations of cosmological structure formation. We have assumed a Cold Dark Matter model and a hierarchical building up of the structure. SNe explosions constitute a key process in galaxy formation since, through the ejection of metals and energy into the interstellar medium, they are believed to trigger important galactic winds, to set a self-regulated cycle for star formation, and to enrich with metals the intergalactic medium. For these reasons, the main goal of our model is to introduce a self-consistent treatment of supernova feedback in numerical simulations, in order to study their possible effects on galaxy formation, and in particular, on disk formation. In addition, with the aim at better reproducing the multiphase character of the real interstellar medium, we have developed a new model for multiphase gas which works consistently with our SN energy feedback treatment.

Our new model has been developed within the Tree-SPH code GADGET-2 (Springel & Hernquist 2002) which works in parallel systems and is specially suitable for running full cosmological and high resolution simulations. The combined model of chemical and energy feedback in the context of the multiphase treatment for the gas component provides a powerful tool to exploit observational data on the chemical and dynamical properties of galaxies to constrain galaxy formation theories.

As a first step towards the description of SN feedback within the simulations, we have implemented a model for chemical evolution (Scannapieco et al. 2005) which takes into account nucleosynthesis from SNIa and SNII separately (Chapter 2). In our model, radiative cooling of the gas according to self-consistent metallicity values is performed by means of precomputed look-up tables. The scheme was designed to allow a reasonably accurate treatment of the main features of stellar evolution while still not becoming computationally too expensive.

Using a number of test simulations both of isolated galaxies and of cosmological structure formation including our chemical model, we have validated our implementation and established some basic results for the effects of chemical enrichment. An important consequence of the presence of metals is the increase in the cooling efficiency that it can cause, leading to accelerated star formation. In our isolated galaxy simulations, the star formation rate for test runs with metal-dependent cooling function can be up to a factor of 1.5 higher than the corresponding one for a test with a primordial cooling function, and up to a factor of 3 lower than for a test run assuming supra-solar cooling. We found that these differences do not originate in the gas in the central regions, because it is already cold and dense anyway. Instead, the differences are caused by more diffuse gas at outer radii which has yet to cool. Here the increase of the cooling efficiency allows condensation of gas and star formation to occur further away from the centre of the systems.

An important implication of this result is that strong effects owing to metal-dependent cooling can only be expected when heavy elements are efficiently transported and mixed into diffuse gas that has yet to cool. In our test runs with chemical enrichment only and which lack of a prescription for SN energy feedback, we found that simulations with metal-dependent cooling produced similar results as simulations with a primordial cooling function. We expect however that this could be very different if a model for efficient metal distribution, such as that produced by SN energy feedback, is added to our chemical simulations. An explicit demonstration of this has been provided by our test simulation where we assumed supra-solar cooling rate functions, resulting in substantially elevated star formation activity and different abundance profiles. Note that in these tests we have explored galaxy scale systems which cool very efficiently. Larger effects from chemical mixing are expected in more massive haloes such as clusters of galaxies (White & Frenk 1991; De Lucia, Kauffmann & White 2004).

We have also tested the impact of a number of assumptions made in our chemical model, and the relevance of numerical parameters. Relaxing the instantaneous recycling approximation for SNII has only a negligible effect and does not change the chemical properties of the simulated systems. However, as also shown by previous work (e.g. Raiteri, Villata & Navarro 1996; Chiappini et al. 1997; Mosconi et al. 2001), the chemical properties of both the stellar populations and the interstellar medium are sensitive to the time-delay associated with SNIa explosions. In agreement with previous results, we found that the latter must be included in order to be able to reproduce the observed chemical properties of galaxies.

We have shown that chemical enrichment can modify the chemical and dynamical properties of forming galactic systems significantly. However, our analysis of chemical feedback has also made it clear that the strength of the influence of metals

on the galaxy formation process depends sensitively on the physics of energy feedback. If the latter is neglected, as we have done as a first approach, metals are not mixed widely in gas that has yet to cool. Effects due to metal-dependent cooling remain then moderate.

As a second step, we have tested the effects of chemical feedback using more realistic initial conditions of a galactic system, specifically chosen from a full cosmological simulation to evolve into a disk-like galaxy (Chapter 3). This galaxy was selected from a cosmological volume of a ΛCDM universe, under the condition of the absence of major mergers since redshift $z = 1$, and is resolved with $\sim 1$ million particles. This gives the correct environmental condition for a disk galaxy to form and enough resolution to avoid numerical artifacts. We have used this simulation, analysing the chemical and dynamical properties of the galaxy, in order to illustrate the main difficulties found so far in simulations which lack an efficient treatment for SN energy feedback.

The analysis of this simulation has shown that, at redshift $z = 0$, the galaxy has consumed most of its gas into stars, leading to a stellar dominant component with a morphology consistent with a spheroid and without an important disk. We found that, within 1.5 $r_{\rm opt}$, the gas mass fraction is very low, $f_{\rm gas} = 0.026$. The spheroidal character of the final galaxy is reflected in the dynamical properties of the baryons: most stellar mass is found to be dominated by velocity dispersion, while only a little fraction of the baryons being consistent with the relation expected for circular orbits in the gravitational potential well of the galaxy. The parameters obtained from a bulge-disk decomposition performed to the projected surface mass density also reflects the lack of a well-formed disk: the disk scalelength is too small in comparison to observations, and the bulge-to-disk ratio found, $M_{\rm b}/M_{\rm d} = 1.35$, is in open disagreement with the observed values for spirals (e.g. MacArthur et al. 2003).

The main cause for this behaviour is the early consumption of gas into stars and the little amount of leftover gas at later times for feeding the formation of a disk. We have found that in this simulation without SN energy feedback, nothing prevents the gas to rapidly cool down and condensate, producing an important stellar, early component which dominates the baryonic matter of the system. In particular, we have found that only $\sim 25\%$ of the final stellar mass of the galaxy was formed in the last 7 $h^{-1}$ Gyr.

As a result of the efficient and early transformation of gas into stars found in this simulation, the chemical properties of the stellar populations do not resemble those of observed spiral galaxies. By roughly segregating our stellar populations into disk, bulge and stellar halo components we have found that all of them have similar

levels of enrichment, in open disagreement with results of our Milky Way which show distinguishable chemical properties for its different components. In particular, we find an excess of metallicity, with distributions which peak at [Fe/H] $\sim +0.3$. This is, in part, explained by the fact that, without an efficient mechanism of metal mixing such as that expected to be driven by SN energy feedback, metals remain in the dense, star-forming regions where they are produced. The inclusion of SN energy feedback would trigger a transportation of metals to the outer regions of galaxies, on its turn decreasing the metal content of the central regions.

In this experiment, the gas component was found to suffer from the 'catastrophic angular momentum loss' problem, already found in other works (e.g. Navarro & Benz 1991; Navarro & White 1994). This has lead to a deficit in the specific angular momentum of the disk and the bulge components of the simulated galaxy, in comparison to observations of spiral galaxies. Moreover, the results are not consistent even with the typical values for ellipticals. These results clearly show the need for introducing other physical processes in order to reproduce galaxies with observational counterparts. SN energy feedback is thought to contribute to the conservation of the angular momentum of the gas and hence it would help to consistently simulate the formation of disk systems.

The results of this simulation (Chapter 3) have shown that our chemical code fails to reproduce the formation of the disk components, as found in other models which lack an efficient SN energy feedback prescription (e.g. Katz & Gunn 1991; Cen & Ostriker 1992,1999; Navarro & White 1993; Metzler & Evrard 1994; Yepes et al. 1997; Kay et al. 2002; Lia, Portinari & Carraro 2002; Semelin & Combes 2002; Marri & White 2003; Springel & Hernquist 2003). Our findings suggest the need for an efficient mechanism capable of self-regulating the star formation rate in galaxies. This would allow recent star formation episodes to occur, contributing to the formation of extended disks. SN explosions are believed to provide such mechanism, through the heating heating up of gas and the disruption of cold gas clouds, and the triggering of galactic outflows. These outflows would also help to contaminate the outer regions of galaxies with metals and could explain observational results which show the presence of metals in the intergalactic medium. The interplay between SN heating, cooling and gas flows would then lead to the formation of the different baryonic components observed in spiral galaxies with distinct dynamical and chemical patterns.

Taking into account our previous results, we have complemented our model for chemical enrichment with a treatment of SN energy feedback by SNII and SNIa (Scannapieco et al. 2006; Chapter 4). This model is tied to a multiphase treatment of the gas components in the ISM, designed to improve the description of the hot, diffuse material in the context of the SPH technique. One of the major advantages

of our model is that no scale-dependent parameters need to be introduced. This makes it especially well suited for simulations of cosmological structure formation where systems of widely different mass form naturally.

We have used a number of idealized simulations of the formation of disk galaxies to study the performance of our numerical techniques. We found that our multiphase scheme leads to an improved description of the diffuse, hot gas which can reach densities up to an order of magnitude higher than those found with a standard SPH implementation of GADGET-2. The multiphase scheme is insensitive to its single free parameter $\alpha$ when the value is varied within a physically motivated range.

Our SN energy feedback scheme efficiently regulates star formation by reheating cold gas and generating winds. The overall impact of SN feedback depends on total mass: in large systems the inclusion of feedback reduces star formation by a factor of a few compared to simulations where it is absent. Smaller systems are more strongly affected, with star formation reduced by more than an order of magnitude and occurring in starburst episodes. This is consistent with observational studies which detect bursty behaviour in the star formation activity of dwarf galaxies (e.g. Kauffmann et al. 2003; Tolstoy et al. 2003). Overall, however, our SN feedback model can reproduce the Kennicutt relation between the surface densities of gas and of star formation both in collapsing and in quiescent systems.

For all the masses we considered, the star formation histories of our idealized protogalactic collapse models are sensitive to the fraction $\epsilon_c$ of energy (and metals) which is dumped into the cold phase. In general, the larger the value of $\epsilon_c$, the more star formation is suppressed, but the effects of varying this parameter are complex because of the nonlinear coupling between star formation, supernova energy release, and radiative cooling.

Our supernova feedback model results in strong winds from star-forming galaxies. The outflows are generally perpendicular to the disk plane and can reach velocities of up to $1000\,\mathrm{km\,s^{-1}}$. We detect a clear anti-correlation between the unbound gas fraction and the total mass, indicating that the strength of the outflows is sensitive to the depth of the gravitational potential well, as expected from theoretical considerations. For a given total mass, we find that the unbound gas fraction increases with the assumed value of the feedback parameter $\epsilon_c$. The mass loss rates we find typically exceed the star formation rates by a factor of a few, as observed in starbursting galaxies.

These winds are efficient in enriching the outer regions of our simulated galaxies and would plausibly contaminate the intergalactic medium. We found that the unbound gas component, regardless of total mass, ends up containing more than 60 per cent of the metals produced in our protogalactic collapses. For the smallest galaxies,

this percentage goes up to 80 per cent or more, independent of the assumed value of $\epsilon_c$. Galaxies with a wide range of masses may thus contribute to the enrichment of the intergalactic medium. This appears required to explain the observation that the bulk of the heavy elements in galaxy clusters resides in the intracluster medium rather than in the galaxies themselves. It will be extremely interesting to compute detailed predictions for this enrichment using cosmological simulations based on our feedback scheme.

Finally, we have applied our treatments of chemical and energy feedback, metal-dependent cooling and multiphase gas in order to analyse the impact of including SN energy feedback on the formation of disk galaxies (Chapter 6). We have resimulated the galaxy analysed in Chapter 3 switching on these mechanisms, and comparatively studied the two simulations. We have also tested the dependence of the results on different assumed input parameters of the SN feedback model. The main result of this analysis is related to the key role of the SN energy feedback process, which contributes to the formation of extended, well-defined disk components. In particular, we have found that the simulated galaxies define bulge-disk systems with structural parameters comparable to those of observed spirals. The existence of a stellar halo component also compares well with the observed patterns of the Milky Way stars (e.g. Freeman & Bland-Hawthorn 2002 and references therein).

In these simulations, we have found that SN energy feedback sets a self-regulated star formation process, leading to the formation of systems in which stars of different ages contribute to the different baryonic components. In particular, we find that $55-70\%$ of the stellar mass in the thick and thin disk components was formed in the last 7 $h^{-1}$ Gyr, in contrast to the spheroidal components (bulge and stellar halo), where only 30% of the stellar mass was formed in the same period.

The different baryonic components formed in these simulations agree quite well with their counterparts in the Milky Way galaxy and other spirals, in both the dynamical and chemical properties. In particular, we found that the specific angular momentum for both disk-like and spheroid-like components are consistent with observations of spirals and ellipticals, respectively. This results from the conservation of angular momentum by the gas component. This is a very important result because of the primary role of the specific angular momentum in disk galaxy formation. Our results have shown that the disk-like components end up with a specific angular momentum content similar to those of the dark matter haloes, supporting the most accepted theory for disk formation.

As it was mentioned before, the chemical properties of the simulated galaxies are consistent with the observational results for stars in our Milky Way. We found that the different baryonic components (thin disk, thick disk, bulge and stellar halo) have

distinguishable chemical abundances, with the stellar halo being the less enriched one. We found a deficit in the metallicity of the thin disk, which we expect can be easily solved by tunning the fraction of metals dumped into the cold and hot phases.

The inclusion of SN energy feedback in our simulations have lead to differences in the dark matter and gas collapse, and in the stellar distributions, in comparison to their counterparts when this process is not included. We find that SN energy feedback produces dark matter haloes which are less concentrated, and more spread gas distributions with a large fraction of diffuse gas. The SN driven winds have prevented the formation of the smallest gas clumps, on its turn preventing the formation of very compact stellar systems. The number of satellite galaxies obtained in simulations with SN energy feedback is smaller than its counterpart when this process is not considered. The survival of the gas reservoirs up to redshift $z = 0$ is another important goal of our model.

We have illustrated the formation process of the galaxies by showing the velocity fields and density maps for the stellar and gaseous components, as a function of time. From this analysis we found that the as the dark matter haloes grow, the gas collapses and settles onto disk-like configurations near redshift $z = 1.5$. Before this time, the systems are mainly spheroidal. Since SN energy feedback helped to maintain the gas reservoirs, the formation of stars at low redshift contributes to the formation of disk-like stellar components. As the result of the complex interplay between SN heating, cooling, accretion of satellites and gas flows, the velocity field of the gas is non trivial. However, the gas flows produced in our simulations including SN energy feedback have allowed a mixing of the metals which are able to enrich the intergalactic medium.

The dramatic impact of this new model for the interstellar medium and SN feedback on the formation of the structure can be envisaged from the results already obtained by applying early versions of this model to the study of different problems related to galaxy formation during the development of this thesis: galaxy-galaxy interactions (Pérez et al. 2006a,b), the mass-metallicity relation (De Rossi 2005, Lic. Thesis; Tissera et al. 2005; De Rossi et al. 2006, in preparation), prepared galaxy mergers (Ganopol 2006, Lic. thesis), GRB host galaxies (Nuza et al. 2006, in preparation), and bulge formation (Tissera et al. 2006).

The model presented in this thesis constitutes a powerful tool to explore the assembly of the structure in a cosmological context, and the evolution of its dynamical, chemical and astrophysical properties. Since it is suitable for running full cosmological simulations, processes such as mergers, interactions and accretion of satellites, which affect the gas collapse and dynamical properties of systems, can be consistently taken into account. As the observational data on astrophysical and

chemical properties of galaxies and the intergalactic medium, in the local universe as well as at high redshift, is increasing dramatically nowadays, this new model will allow better constrain of galaxy formation models by confronting their predictions with observations of different nature.

# Appendix A

# The simulation code GADGET-2

In this Appendix we summarize the main basic characteristics of the numerical methods used to compute the cosmological evolution of the matter. We have developed our model for Supernova chemical and energy feedback within the code GADGET-2 (Springel & Hernquist 2002; Springel 2005) which describes the coupled evolution of a collisionless fluid and an ideal gas. This code uses a lagrangian approach in which the physical quantities of the matter are traced by a set of particles which evolve in a universe whose global dynamics is determined by the assumed cosmological model. In simulations of galaxy formation, three independent components are usually used to trace the evolution of the interstellar medium, the dark matter component and the stars. These different components are described as gas, dark matter and stellar particles, respectively. Dark matter and stars are treated as self-gravitating, collisionless fluids while the motion of the gas is followed in terms of the hydrodynamical equations. GADGET-2 can be used to simulate individual, isolated galaxies as well as cosmological volumes. However, even the simplest simulations normally involve a large computational cost. For this reason, GADGET-2 is a fully parallel code prepared to run in a number of processors which divide the computational work. This helps to run very large simulations in relative small times. In what follows we briefly summarize the main characteristics of the code GADGET-2.

## A.1 Gravity

For the computation of gravitational forces, GADGET-2 combines a Particle Mesh method (PM; Hockney & Eastwood 1981; Efstathiou et al. 1985) and a Tree algorithm (Barnes & Hut 1986; Jernigan & Porter 1989). In order to avoid the high computational cost of direct summation methods for computing the gravitational force on a given particle which results from the interaction with all other particles (this scales as the squared of the number of particles), it is usual to decompose the gravitational force in a large-range force which varies smoothly over the particle distribution, plus a contribution from nearby particles. In particular, different

approaches to calculate this latter term range from an exact particle-to-particle calculation to more sophisticated models such as Tree algorithms.

In GADGET-2, the large range force is calculated by means of the PM method. In the context of the PM method, the simulated matter is divided into a number of *superparticles* which are placed over a regular mesh. In order to avoid numerical divergences, these superparticles are assumed to occupy a given volume and they are not allowed to get closer to each other than a given distance, called the *gravitational softening*. From this distribution of superparticles the large-range gravitational force is computed, and then interpolated to obtain the corresponding force at any point in the simulated volume.

On the other hand, tree algorithms (Barnes & Hut 1986; Jernigan & Porter 1989) are used to compute the gravitational force exerted at a given particle by nearby material. In this scheme, close particles are arranged in a hierarchy of groups. The gravitational force resulting from distant groups on a given particle is obtained by summing over multipole expansions of these groups. Tree algorithms are efficient at computing the gravitational forces wiht a computational cost which scales as $N\ln(N)$ (instead of the $N^2$ scaling of direct summation). Tree codes are easily implemented in distributions of any geometry, which makes them specially suitable for cosmological simulations where different levels of clustering need to be reproduced.

## A.2 HYDRODYNAMICS

GADGET-2 describes the gas component by integrating the hydrodynamical equations applying the Smoothed Particle Hydrodynamics (SPH; Lucy 1977; Gingold & Monaghan 1977) technique. Within SPH, a fluid is represented by $N$ particles whose motion is governed by the laws of the hydrodynamics. These particles carry the physical information of the mass they represent, such as their positions and velocities. The thermodynamical state of a fluid element is followed by using equivalently, its energy per mass unit, $u_i$, or its entropy per mass unit, $s_i$. GADGET-2 uses $s_i$ instead of $u_i$ as the independent thermodynamic variable evolved in SPH. In this way, the system's set of equations fulfills the conservation of entropy as well as energy in absence of sinks of heat. Standard implementations of SPH which instead integrate the energy per mass unit can suffer from violations of the conservation of entropy in some situations (Springel & Hernquist 2002). An entropic function $A \equiv P/\rho^\gamma$, where $P$ and $\rho$ denote pressure and density, respectively, is usually more convenient to work with than the entropy per mass unit. Since $A$ is only function of $s$, $A$ is often refered to as *entropy*. In the above equation, $\gamma$ characterizes the equation of state of the fluid, which, in cosmological applications, is often described as an ideal, inviscid gas, i.e.,

$$P = (\gamma - 1)\rho\, u \tag{A.1}$$

with $\gamma = 5/3$.

Relevant in the SPH formalism is the concept of a particle *neighbours*, defined in some convenient manner. Its importance relies on the fact that, in SPH, the physical quantities of simulated particles are *smoothed* over the physical space, taking into account the properties of the closest neighbours. For this purpose, a *kernel function* is defined which determines the relative contribution of particles within the neighbouring region. The smoothing procedure helps to avoid numerical instabilities and divergences, but has the drawback that large gradients of any quantity can not be properly represented.

In GADGET-2, the kernel function is defined as (Monaghan & Lattanzio 1985):

$$W(|\mathbf{r}|,h) = \frac{8}{\pi h^3}\begin{cases} 1-6(r/h)^2+6(r/h)^3 & \text{si } 0 \le (r/h) \le 1/2 \\ 2(1-(r/h)^3 & \text{si } 1/2 < (r/h) \le 1 \\ 0 & \text{(r/h)} > 1 \end{cases}$$

Here, $|\mathbf{r}| = |\mathbf{r}_i - \mathbf{r}_j|$ is relative separation of particles $i$ and $j$, and and $h$ is known as the *smoothing length*, which sets the smoothing spatial extension. Note that $W$ is symmetric in $i-j$ and, by definition, is normalized to unity.

In general, individual smoothing lengths $h_i$ for each particle are calculated so that the mass enclosed in their kernel volume remains constant for the estimated density, or equivalently, to enclose a fixed number of neighbours. In this way, particles in high density regions will have smaller smoothing lengths than particles in low density environments. In our work, we choose to assume a fixed enclosed mass, then, the smoothing lengths and densities obey the (implicit) equations:

$$\frac{4\pi}{3h_i^3\rho_i} = N_{\rm ngb} < m > \tag{A.2}$$

where $N_{\rm ngb}$ is the typical number of SPH neighbours (generally $\approx 32$) and $< m >$ the average (gas) particle mass.

Of particular interest in galaxy formation is the estimation of the density field. This is because the hydrodynamical evolution of the gas is affected by the density estimation. For example, the transformation of gas into stars is based on a density criterium, and the radiative cooling rates also depend on density. Hence, if densities are not properly estimated, artificial effects could be introduced. In SPH, the density of a given $i$ particle is calculated as:

$$\rho_i = \sum_j^N m_j W(|\mathbf{r}_i - \mathbf{r}_j|, h) \tag{A.3}$$

where $j$ runs through the $N$ neighbours of $i$ particle and $m_j$ denotes mass. The smoothing of SPH, in this respect, usually leads to an overestimation of the densities.

This happens when cold gas clumps form within hot regions, in which case the density of low density particles is overestimated by including dense particles in the sum defined by eq. A.3. In general, different approaches are invoked to avoid this odd behaviour (see Chapter 4).

In the *entropy conservation* formulation of SPH in GADGET-2, the equations of motion for the SPH particles are given by (Springel & Hernquist 2002):

$$\frac{dv_i}{dt} = -\sum_{j=1}^{N} m_j \Big[ f_i \frac{P_i}{\rho_i^2} \nabla_i W_{ij}(h_i) + f_j \frac{P_j}{\rho_j^2} \nabla_i W_{ij}(h_j) \Big] \tag{A.4}$$

where $P_i = A_i \rho_i^\gamma$ is the pressure of particle $i$, $f_i$ are defined as:

$$f_i = \Big[ 1 + \frac{h_i}{3\rho_i} \frac{\partial \rho_i}{\partial h_i} \Big]^{-1} \tag{A.5}$$

and the notation $W_{ij} \equiv W(|\mathbf{r}_i - \mathbf{r}_j|, h)$ has been used. Provided there are no external sources or heat of shocks, $A_i$ remains constant and these equations correspond to the dynamics of a reversible fluid in SPH.

However, real gases can easily develop shocks where kinetic energy is irreversibly transformed into heat, increasing the entropy of the system. Within the SPH formalism, the effects of such shocks are introduced as an *artificial viscosity*. Different approaches to model the viscosity have been used in simulations of galaxy formation, and several times improved to handle with new shortcomings (see Springel 2005 and references therein). Taking into account previous results, GADGET-2 models the viscous force in the following form:

$$\frac{dv_i}{dt}\Big|_{visc} = -\sum_{j=1}^{N} m_j \Pi_{ij} \nabla_i \bar{W}_{ij} \tag{A.6}$$

where $\bar{W}_{ij}$ is the arithmetic mean average of $W_{ij}(h_i)$ and $W_{ij}(h_j)$, and $\Pi_{ij} \geq 0$ is defined as:

$$\Pi_{ij} = -\frac{\alpha}{2} \frac{[c_i + c_j - 3w_{ij}] w_{ij}}{\rho_{ij}} \tag{A.7}$$

In this equation, $\alpha$ is a parameter used to regulate the strength of the viscosity, and $w_{ij} = \mathbf{v}_{ij} \cdot \mathbf{r}_{ij} / |\mathbf{r}_{ij}|$ is the relative velocity of particles $i$ and $j$ projected onto their separation vector and, by definition, is non-zero only when particles approach each other (i.e. if $\mathbf{v}_{ij} \cdot \mathbf{r}_{ij} < 0$ ). In order to avoid spurious angular momentum transport in shear flows, GADGET-2 uses an additional limit to the viscosity, which follows the approach of Balsara (1995) and Steinmetz (1996). This is introduced by multipying $\Pi_{ij}$ in equation A.7 by a factor $f_i + f_j$ where

$$f_i = \frac{|\nabla \times v|_i}{|\nabla \cdot v|_i + |\nabla \times v|_i} \tag{A.8}$$

measures the relative amount of shear around particle $i$, based on standard SPH estimates for divergence and curl (Monaghan 1992).

## A.3 COSMOLOGICAL EVOLUTION AND TIME INTEGRATION

Each particle in the system is evolved taking into account the net acceleration acting over it, including gravity for all particles plus the contribution of the hydrodynamical acceleration in the case of gas particles. In cosmological simulations, the time integration should also consider the assumed cosmological model. According to the standard cosmological paradigm, this corresponds to an expanding universe. Hence, each particles $i$ is governed by the following equation:

$$\ddot{\mathbf{x}}_i + 2H\dot{\mathbf{x}}_i = -\frac{1}{a^3}\nabla\Phi_i \tag{A.9}$$

In this expression, $\mathbf{x}_i$ is the comoving position of the $i$ particle, $a$ the expansion factor of the universe and $\Phi_i$ the gravitational potential at the $i$ particle's position. The Hubble parameter $H$ carries the information of the expansion rate of the universe, being defined as $H \equiv \dot{a}/a$. GADGET-2 uses comoving the coordinates ($\mathbf{x}$) and velocities ($\dot{\mathbf{x}}$) for the time integration, which are related to the physical coordinates ($\mathbf{r}$) and velocities ($\dot{\mathbf{r}}$) by: $\mathbf{r} = a\mathbf{x}$ and $\dot{\mathbf{r}} = \dot{a}\mathbf{x} + a\mathbf{v}$.

For the time integration itself, GADGET-2 uses the *leap-frog* scheme. In this scheme, particles and velocities are advanced according to:

$$\mathbf{x}^{m+1/2} = \mathbf{x}^{m-1/2} + \mathbf{v}^m \Delta t + O(\Delta t^3) \tag{A.10}$$

$$\mathbf{v}^{m+1} = \mathbf{v}^m + \frac{d\mathbf{v}}{dt}^{m+1/2} \Delta t + O(\Delta t^3) \tag{A.11}$$

where $m$ indicates the code step and $\Delta t$ is the integration timestep. In GADGET-2, each particle owns a different timestep. These individual timesteps for each particle are calculated taking into account the net force exerted on the particle and the ability of the integration scheme to *predict* the near evolution. In practice, in order to avoid looses of computational time, particles are advanced in bunches.

A large number of additional numerical issues, such as details of the integration scheme, paralellization, implementation of the tree algorithm and SPH, which are out of the scope of this summary, can be found in Springel & Hernquist 2002 and Springel 2005.

# Appendix B

# The Navarro, Frenk & White Dark Matter Profile

The dark matter potential wells of galaxies of a wide range of masses and of rich galaxy clusters are found to be well represented by a universal profile. Navarro, Frenk & White (1996) used numerical simulations of galactic systems in the mass range $M_{\rm vir} \sim [10^{11} - 10^{15}]$ $M_{\odot}$, finding that dark matter halo profiles are approximately isothermal over a large range in radii, but they are significantly shallower than $r^{-2}$ near the centre and steeper than $r^{-2}$ near the virial radius. Taking into account their results, they derived a law which best fits their simulated dark matter haloes. This fitting, known as the Navarro, Frenk and White profile, relates the spherically average density with radius as:

$$\frac{\rho}{\rho_{\rm crit}} = \frac{\delta_c}{(r/r_s)(1+r/r_s)^2} \tag{B.1}$$

where $r_s = r_{\rm vir}/c_{\rm NFW}$ (the 'scale radius') is a characteristic radius and $\rho_{\rm crit}$ is the critical density of the universe. The parameter $c_{\rm NFW}$ is the 'concentration' of the profile and is linked to $\delta_c$, the 'characteristic overdensity' of the halo, by the requirment that the mean density within the virial radius $r_{\rm vir}$ should be $200 \times \rho_{\rm crit}$.

# Appendix C

# The Angular Momentum of Galaxies

The angular momentum content of a galaxy plays a fundamental role on the determination of several important galactic properties such as morphology and dynamics. In the case of spiral galaxies, as the gas cools down and condenses within the dark matter haloes, the evolution of the angular momentum is thought to determine the resulting structural properties of the disks. Observationally, it is found that the specific angular momentum (i.e. angular momentum per mass unit) of spiral galaxies is $\sim 6$ times larger than the corresponding ones for ellipticals (Fall 1983). Furthermore, the spin parameter of spirals is found to be related to morphology. The spin parameter of a galaxy is defined as

$$\lambda \equiv \frac{J\ E^{1/2}}{G\ M^{5/2}} \tag{C.1}$$

where $J$ is the angular momentum of the galaxy, $E$ its binding energy and $M$ its mass ($G$ is the gravitational constant). Observations show that spiral galaxies have $\lambda \sim 0.5$, while ellipticals have $\lambda$ values one order of magnitude lower.

According to the standard model for gravitational instability, the angular momentum of galaxies is not primordial but results from tidal torques exerted between neighbouring protogalaxies during the early universe (Peebles 1969). The magnitude of these torques can be estimated both from theoretical calculations in the linear regime and through N-body simulations (Peebles 1980; Efstathiou & Jones 1979; White 1984; Barnes & Efstathiou 1987). These estimations have shown that a typical protogalaxy would have spin parameters in the range $\lambda \sim 0.05 - 0.07$. In order to understand the higher values of $\lambda$ obtained from observations in the local universe, some physical process which can increase the spin parameter value by an order of magnitude needs to be invoked.

Nowadays, the formation of disk-like configurations is understood in the context of the disk formation theory developed by Fall & Efstathiou (1980). This theory is based on the conservation of the specific angular momentum of the dark matter (DM) and baryonic components along the evolutionary process. If the specific angular

momentum is conserved for the dark matter and baryonic (disk-like) components, then:

$$\frac{J_{\rm DM}}{M_{\rm DM}} = \frac{J_{\rm disk}}{M_{\rm disk}} \tag{C.2}$$

where $J$ denotes angular momentum and $M$ mass. This result is valid provided the halo does not suffer important deviations from axisymmetry. Assuming that the mass of a galaxy remains more or less constant, and that Eq. C.2 is valid, spirals could increase their spin parameter to match the observed $\lambda$ value at redshift $z = 0$ only if their binding energy increases. The dissipative nature of baryons provides an easy explanation for this phenomenon, since they can dissipate energy and collapse further within the dark matter haloes, increasing the binding energy of the systems. For a typical galaxy with 10% of gaseous mass and 90% of dark matter, an increase in $\lambda$ of an order of magnitude can be obtained if the gas collapses by a factor of 10. In this way, the observational results can be reproduced.

In this context, the formation of spiral galaxies is thought to occur in a series of stages. During a first period, dark matter and baryons experience (the same) tidal torques from neighbouring protogalaxies, and collapse together into overdense regions. In this period, baryons can not dissipate energy because of the low background density. After some time the dark matter component virializes, while the increase in density allows now the baryons to cool down. As a result, the baryonic component collapses further within the dark matter haloes. Finally, the dark matter condenses again as a result of the concentration of baryons into the central regions.

Fall & Efstathiou's theory has been successful in reproducing an important number of properties of disk galaxies in analytic and semi-analytic modelling (e.g. Mo, Mao & White 1998; Somerville, Primack & Faber 2001). However, numerical simulations have found that the angular momentum of the baryons can be easily transported to the dark matter haloes during violent events (e.g. Mihos & Hernquist 1996). As a result, baryons collapse rapidly and concentrate in the centre of the dark matter haloes. This effect produces disks that are too small and with lower angular momentum content than that expected (Navarro & Steinmetz 1997). This effect is known as the *catastrophic angular momentum loss*. Note that if the baryons managed to avoid the rapid collapse into the centre of the haloes and experienced a smoother dissipative collapse, they might form rotationally supported disk-like structures. Recently, numerical simulations have shown promising advances in this field (Domínguez-Tenreiro et al. 1998; Abadi et al 2003; Robertson et al. 2004). These works have shown that, if disk-like structures can develop, the formation of important spheroidal, slowly rotating components could help to stabilize the disk configurations along the evolutionary process. These works have also agreed in the need of including Supernova feedback effects as a crucial mechanism to regulate star formation and to contribute to the formation of extended, well-defined disks.

The catastrophic angular momentum loss is an even more severe problem in the

framework of hierarchical clustering, since centrifugally supported disks are unstable to rapid fluctuations in the gravitational potential such as those produced by mergers and accretion of satellites (Toth & Ostriker 1992; Quinn, Hernquist & Fullagar 1993; Velazquez & White 1999). Hence, the survival of extended disks observed in present galaxies points to a mass accretion history in which major mergers did not play a fundamental role, at least in the recent past history. This is difficult to reconcile with a hierarchical universe unless angular momentum loss is prevented under certain circumstances.

# Appendix D

# Bulge-disk Decompositions

In order to quantify the properties of the baryonic mass distributions of galaxies, the so-called *bulge-disk decompositions* are usually performed both in observational data (in this case luminosity distributions are considered) and in simulated galaxies. These bulge-disk decompositions can be applied to systems formed by a spheroidal, bulge-like component plus a disk-like configuration. The mass distribution of such a galaxy is first projected onto the plane of the disk, defined by the angular momentum of the system. The vertical structure of the galaxy can also be tested performing a similar fit to the distribution projected onto a plane parallel to the angular momentum of the system (i.e. perpendicular to the disk plane).

According to theoretical considerations, the projected mass surface density of a disk-like configuration follows an exponential law with the projected distance $r$:

$$\Sigma_{\rm d} = \Sigma_{\rm d}^{\rm o} \exp[-(r/r_{\rm d})] \tag{D.1}$$

where $r_{\rm d}$ is the disk scalelength and $\Sigma_{\rm d}^{\rm o}$ the disk central mass surface density. Conversely, the surface mass density for the bulge component is generally assumed to follow the Sérsic law:

$$\Sigma_{\rm b} = \Sigma_{\rm b}^{\rm o} \exp[-(r/r_{\rm b})^{1/n}] \tag{D.2}$$

where $r_{\rm b}$ is the bulge scalelength, $\Sigma_{\rm b}^{\rm o}$ the corresponding central mass surface density and $n$ the bulge shape parameter. Elliptical galaxies are found to follow this law with a bulge parameter of $n = 4$, this is known as the 'de Vaucouleurs' law. If $n = 1$, an exponential profile is recovered. In spiral galaxies, it is found that bulges have bulge parameters in the range $n = 0.5 - 4$, being $n$ sometimes used as a morphology indicator.

From Eqs. D.1 and D.2 we can estimate the mass profiles for the disk and bulge components:

$$M_{\rm d}(r) = \int_0^r \Sigma_d \; 2\pi r dr = 2\pi\Sigma_d^o r_d^2 \Big[1 - \Big(1 + \frac{r}{r_d}\Big)\exp\Big(\frac{-r}{r_d}\Big)\Big] \tag{D.3}$$

$$M_{\rm b}(r) = \int_0^r \Sigma_b \; 2\pi r dr = 2\pi \Sigma_b^o r_b^2 n \gamma\Big(2n, \big(\frac{r}{r_b}\big)^{1/n}\Big) \tag{D.4}$$

where $\gamma$ is the incomplete gamma function. Recall that in order to confront simulations with observations, mass-luminosity ratios should be considered. Here, we neglect them in order to avoid the inclusion of extra parameters which are poorly known.

Assuming that disks and bulges extend to infinity, the formulae in Eqs. D.3 and D.4 can be used to estimate the total mass of each of these components:

$$M_{\rm d} = 2\pi \Sigma_{\rm d}^{\rm o} r_{\rm d}^2 \tag{D.5}$$

$$M_{\rm b} = 2\pi \Sigma_{\rm b}^{\rm o} r_{\rm b}^2 n \Gamma(2n) \tag{D.6}$$

where $\Gamma$ is the complete gamma function. On the other hand, assuming that there are no extra mass components, the total baryonic mass of the galaxy, $M_{\rm bar}$, can be calculated as:

$$M_{\rm bar} = M_{\rm d} + M_{\rm b} \tag{D.7}$$

Since $M_{\rm bar}$ is known in simulations, the surface density profiles can be fitted to determine the four free parameters: $r_{\rm d}$, $r_{\rm b}$, $\Sigma_{\rm b}^{\rm o}$ (or $\Sigma_{\rm d}^{\rm o}$) and $n$. These parameters can be used to test the structural properties of a galaxy. We will apply this method in order to analyse the results of our simulated galaxies.

Observational results are usually described by means of the *effective radius* for the bulge instead of using the bulge scalelength. The effective radius is defined as the one that encloses half of the bulge surface luminosity. The effective radius is analytically related to the bulge scalelength easily (e.g. MacArthur et al. 2003). We will use this effective radius when comparison with observations is done.

# Appendix E

## Frequently used symbols and abbreviations

| | |
|---|---|
| $c$ | Star formation efficiency |
| $c_{\rm NFW}$ | Navarro, Frenk & White concentration parameter |
| $H_0 = 100\ h$ km s$^{-1}$ Mpc$^{-1}$ | Hubble constant |
| $\lambda$ | Spin parameter |
| $M_{\rm vir}$ | Virial mass |
| $M_{\rm bar}$ | Baryonic mass |
| $r_{\rm vir}$ | Virial radius |
| $\tau_{\rm dyn}$ | Dynamical time |
| $\tau_{\rm cool}$ | Cooling time |
| $\Omega_{\rm b}$ | Baryonic mass density in units of critical density |
| $\Omega_{\rm m}$ | Matter density in units of critical density |
| $\Omega_\Lambda$ | Cosmological constant density in units of critical density |
| $r_{\rm opt}$ | Optical radius |
| $z$ | Redshift |

| | |
|---|---|
| CDM | Cold Dark Matter |
| IGM | Intergalactic Medium |
| IMF | Initial Mass Function |
| IRA | Instantaneous Recycling Approximation |
| ISM | Interstellar Medium |
| PM | Particle-Mesh |
| SFR | Star Formation Rate |
| SN | Supernova |
| SNIa | Type Ia Supernova |
| SNII | Type II Supernova |
| SPH | Smoothed Particle Hydrodynamics |

# Bibliography


[1] Abadi M.G., Navarro J.F., Steinmetz M., Eke V.R., 2003, ApJ, 591, 499

[2] Adelberger K.L., Steidel C.C., Shapley A.E., Pettini M., 2003, ApJ, 584, 45

[3] Balsara D.S., 1995, J.Comp.Phys., 121, 357

[4] Barnes J.E., Efstathiou G., 1987, ApJ, 319, 575

[5] Barnes J.E., Hut P., 1986, Nature, 324, 446

[6] Brodie J.P., Huchra J.P., 1991, ApJ, 379, 157

[7] Burkert A., Hensler G., 1988, A&A, 199, 131

[8] Boisser S., Prantzos N., 2000, MNRAS, 312, 398

[9] Burkert A., Truran J.W., Hensler G., 1992, ApJ, 391, 651

[10] Cen R., Ostriker J.P., 1992, ApJ, 399, L113

[11] Cen R., Ostriker J.P., 1999, ApJ, 519, L109

[12] Chiappini C., Matteucci F., Gratton R., 1997, ApJ, 477, 765

[13] Chiba M., Beers T., 2000, AJ, 199, 2843

[14] Croton D.J., et al., 2006, MNRAS, 365, 11

[15] Dahlem M., Weaver K.A., Heckman T.M., 1998, ApJS, 118, 401

[16] De Lucia G., Kauffmann G., White S.D.M., 2004, MNRAS, 349, 1101

[17] Dekel A., Silk J., 1986, ApJ, 303, 39

[18] Di Matteo T., Springel V., Hernquist L., 2005, Nature, 433, 604

[19] Domínguez-Tenreiro R., Tissera P.B. & Sáiz A. 1998, ApJ, 508, L123

[20] Efstathiou G., 2000, MNRAS, 317, 697

[21] Efstathiou G., Davis M., Frenk C.S., White S.D.M., 1985, ApJS, 57, 241

[22] Efstathiou G., Jones B.J.T., 1979, MNRAS, 186, 133

[23] Ettori S., Fabian A.C., Allen S.W., Johnstone M.N., 2002, MNRAS, 331, 635

[24] Fall S.M., 1983, *Internal kinematics and dynamics of galaxies*, Dordrecht, D. Reidel Publishing Co., p. 391

[25] Fall S.M., Efstathiou, G., 1980, MNRAS, 193, 189

[26] Ferrini F., Matteucci F., Pardi C., Peuco U., 1992, ApJ, 387, 138

[27] Freeman K., 1987, ARA&A, 25, 603

[28] Freeman K., Bland-Hawthorn J., 2002, ARA&A, 40, 487

[29] Frye B., Broadhurst T., Benítez N., 2002, ApJ, 568, 558

[30] Garnett D.R., Shields G.A., 1987, ApJ, 317, 82

[31] Gerritsen J.P.E., Icke V., 1997, A&A, 325, 972

[32] Gilmore G., Reid N., 1993, MNRAS, 202, 1025

[33] Gilmore G., Wyse R.F.G., 1998, AJ, 116, 748

[34] Gingold R.A., Monaghan J.J., 1977, MNRAS, 181, 375

[35] Greggio L., 1996, in Kunth D., Guiderdoni B., Heydari-Malayeri M., Thuan T., eds, The Interplay Between Massive Star Formatin, the ISM and Galaxy Evolution. Editions Frontières, Gif-sur-Ivette, p.89

[36] Greggio L., Renzini A., 1983, A&A, 118, 217

[37] Harfst S., Theis Ch., Hensler G., 2006, A&A, 449, 509

[38] Hockney R.W., Eastwood J.W., 1981, *Computer Simulations Using Particles*, New York: McGraw-Hill

[39] Hultman J., Pharasyn A., 1999, A&A, 347, 769

[40] Jernigan J.G., Porter D.H., 1989, ApJS, 71, 871

[41] Källander D., Hultman J., 1998, A&A, 333, 399

[42] Katz N., 1992, ApJ, 391, 502

[43] Katz N., Gunn J.E., 1991, ApJ, 377, 365

[44] Kauffmann G., 1996, MNRAS, 281, 475

[45] Kauffmann G., Charlot S., 1998, MNRAS, 294, 705

[46] Kauffmann G., Guiderdoni B, White S.D.M., 1994, MNRAS, 267, 981

[47] Kauffmann G., et al., 2003, MNRAS, 341, 54

[48] Kawata D., Gibson B.K., 2003, MNRAS, 340, 908

[49] Kay S.T., Pearce F.R., Frenk C.S., Jenkins A., 2002, MNRAS, 330, 113

[50] Kay S.T., Pearce F.R., Jenkins A., Frenk C.S., White S.D.M., Thomas P.A., Couchman H.M.P., 2000, MNRAS, 316, 374

[51] Kennicutt R.C., 1998, ApJ, 498, 541

[52] Kobayashi C., 2004, MNRAS, 347, 740

[53] Kobulnicky H.A. et al., 2003, ApJ, 599, 1006

[54] Lamareille F., Mouhcine M., Contini T., Lewis I., Maddox S., 2004, MNRAS, 350, 396

[55] Larson R.B., 1974, MNRAS, 169, 229

[56] Larson R.B., 1976, MNRAS, 176, 31

[57] Lehnert M.D., Heckman T.M., 1995, ApJS, 97, 89L

[58] Lehnert M.D., Heckman T.M., 1996, ApJ, 472, 546

[59] Lia C., Portinari L., Carraro G., 2002, MNRAS, 330, 821

[60] Lilly S.J., Carollo C.M., Stockton A.N., 2003, ApJ, 597, 730

[61] Liu W., Chaboyer B., 2000, ApJ, 544, 818

[62] Lucy L.B., 1977, ApJ, 82, 1013

[63] MacArthur L.A., Courteau S., Holtzman J.A., 2003, ApJ, 582, 689

[64] Marri S., White S.D.M., 2003, MNRAS, 345, 561

[65] Martin C.L., 1999, ApJ, 513, 156

[66] Martin C.L., 2004, AAS, 205, 8901

[67] McKee C.F., Ostriker J.P., 1977, ApJ, 218, 148

[68] McWilliam A., Rich R.M., 1994, ApJS, 91, 749

[69] Metzler C., Evrard A., 1994, ApJ, 437, 564

[70] Mihos J.C., Hernquist, L., 1996, ApJ, 464, 641

[71] Mo H.J., Mao S., White S.D.M., 1998, MNRAS, 295, 319

[72] Monaghan J.J., 1992, ARA&A, 30, 543

[73] Mori M., Yoshii Y., Tsujimoto T., Nomoto K., 1997, ApJ, 478, L21

[74] Morrison H.L., 1993, AJ, 106, 578

[75] Mosconi M.B., Tissera P.B., Lambas D.G., Cora S.A., 2001, MNRAS, 325, 34

[76] Mushotzky R.F., Loewenstein M., Arnaud K., Tamura T., Fukazawa Y., Matsushita K., Kikuchi K., Hatsukade I., 1996, ApJ, 466, 686

[77] Nagashima M., Lacey C.G., Baugh C.M., Frenk C.S., Cole S., 2005, MNRAS, 358, 1247

[78] Navarro J.F., Benz W., 1991, ApJ, 380, 320

[79] Navarro J.F., Frenk C.S., White S.D.M., 1996, ApJ, 462, 563

[80] Navarro J.F., Frenk C.S., White S.D.M., 1997, ApJ, 490, 493

[81] Navarro, J.F., Steinmetz, M., 1997, ApJ, 478, 13

[82] Navarro J.F., White S.D.M., 1993, MNRAS, 265, 271

[83] Navarro J.F., White S.D.M., 1994, MNRAS, 267, 401

[84] Nordström B., et al., 2004, A&A, 418, 989

[85] Okamoto T., Jenkins A., Eke V.R., Quilis V., Frenk C.S., 2003, MNRAS, 345, 429

[86] Okamoto T., Eke V.R., Frenk C.S., Jenkins A., 2005, MNRAS, 363, 1299

[87] Pagel B.E.J., 1997, Nucleosynthesis and Chemical Evolution of Galaxies. Cambridge University Press, Cambridge, chap. 8

[88] Pearce F.R. et al. 1999, ApJ, 521, 99

[89] Pearce F.R., Jenkins A., Frenk C.S., White S.D.M., Thomas P.A., Couchman H.M.P., Peacock J.A., Efstathiou G., 2001, MNRAS, 326, 649

[90] Peebles, P.J.E., 1969, ApJ, 155, 393

[91] Pérez M.J., Tissera P.B., Lambas D.G., Scannapieco C., 2006a, A&A, 449, 23

[92] Pérez M.J., Tissera P.B., Scannapieco C., Lambas D.G., De Rossi M.E., 2006b, A&A, in press

[93] Pfenniger D., Norman C., 1990, ApJ, 363, 391

[94] Prochaska J.X., Wolfe A.M., 2002, ApJ, 566, 68

[95] Quinn P.J., Hernquist L., Fullagar D.P., 1993, ApJ, 403, 74

[96] Raiteri C.M., Villata M., Navarro J.F., 1996, A&A, 315, 105

[97] Rich R.M., 2001, in *Astrophysical Ages and Time Scales*, T. von Hippel, C. Simpson, N. Manset, eds., ASP Conf. Series, 245, 216

[98] Robsertson B., Yoshida N., Springel V., Hernquist L., 2004, ApJ, 606, 32

[99] Rupke D.S., Veilleux S., Sanders D.B., 2002, ApJ, 570, 588

[100] Ryan S.G., Norris J.E., 1991, AJ, 101, 1865

[101] Scannapieco C., Tissera P.B., White S.D.M., Springel V., 2005, MNRAS, 364, 552

[102] Scannapieco C., Tissera P.B., White S.D.M., Springel V., 2006, MNRAS, submitted

[103] Searle L., Zinn R., 1978, ApJ, 225, 357

[104] Semelin B., Combes F., 2002, A&A, 388, 826

[105] Shapley A.E., Steidel C.C., Adelberger K.L., Dickinson M., Giavalisco M., Pettini M., 2001, ApJ, 562, 95

[106] Shapley A.E., Erb D.K., Pettini M., Steidel C.C., Adelberger K.L., 2004, ApJ, 612, 122

[107] Skillman E.D., Kennicutt R.C., Hodge P.W., 1989, ApJ, 347, 875

[108] Sommer-Larsen J., Gelato S., Vedel H., 1999, ApJ, 519, 501

[109] Somerville R.S., Primack J.R., Faber S.M., 2001, MNRAS, 320, 504

[110] Springel V., Di Matteo T., Hernquist L., 2005, MNRAS, 361, 776

[111] Springel V., Hernquist L., 2002, MNRAS, 333, 649

[112] Springel V., Hernquist L., 2003, MNRAS, 339, 289

[113] Springel V., 2005, MNRAS, 364, 1105

[114] Springel V., Yoshida N., White S.D.M., 2001, New Astronomy, 6, 79

[115] Steinmetz M., 1996, MNRAS, 278, 1005

[116] Steinmetz M., Müller E., 1994, A&A, 281, L97

[117] Stoehr F., White S.D.M., Tormen G., Springel V., 2002, MNRAS, 335, 84L

[118] Sutherland R.S., Dopita M.A., 1993, ApJS, 88, 253

[119] Thacker R.J., Couchman H.M.P., 2000, ApJ, 545, 728

[120] Thacker R.J., Couchman H.M.P., 2001, ApJ, 555, L17

[121] Thacker R.J., Tittley E.R., Pearce F.R., Couchman H.M.P., Thomas, P.A., 2000, MNRAS, 319, 619

[122] Theis C., Burkert A., Hensler G., 1992, A&A, 265, 465

[123] Thielemann F.K., Nomoto K., Hashimoto M., 1993, in Prantzos N., Vangoni-Flam E., Cassé N., eds, Origin and Evolution of the Elements. Cambridge University Press, Cambridge, p.299.

[124] Timmes F.X., Woosley S.E., Weaver T.A., 1995, ApJS, 98, 617

[125] Tinsley B.M., Larson R.B., 1979, MNRAS, 186, 503

[126] Tissera P.B., De Rossi M.E., Scannapieco C., 2005, MNRAS, 364, 38L

[127] Tissera P.B., Smith Castelli A.V., Scannapieco C., 2006, A&A, in press

[128] Tolstoy E., Venn K.A., Shetrone M., Primas F., Hill V., Kaufer A., Szeifert T., 2003, ApJ, 125, 707

[129] Tornatore L., Borgani S., Matteucci F.,Recchi S., Tozzi P., 2004, MNRAS, 349, 19L

[130] Toth T., Ostriker J.P., 1992, ApJ, 389, 5

[131] Tremonti C.A., Heckman T.M., Kauffmann G., Brinchmann J., Charlot S., et al., 2004, ApJ, 613, 898

[132] Trentham N., Tully R.B., 2002, MNRAS, 335, 712

[133] Valdarnini R., 2003, MNRAS, 339 , 1117

[134] Van den Bergh S., 1991, ApJ, 369, 1

[135] Velázquez H., White S.D.M., 1999, MNRAS, 304, 254

[136] White S.D.M., 1996, in *Cosmology and large scale structure*, Proceedings of the "Les Houches Ecole d'Ete de Physique Theorique", Richard Schaeffer, Joseph Silk, Michel Spiro and Jean Zinn-Justin, eds. Elsevier Scientific Publishing Company, Amsterdam, p.349

[137] White S.D.M., Efstathiou G., Frenk C.S., 1993, MNRAS, 262, 1023

[138] White S.D.M., Frenk C.S., 1991, ApJ, 379, 52

[139] White S.D.M., Rees M.J., 1978, MNRAS, 183, 341

[140] Woosley S.E., Weaver T.A., 1995, ApJS, 101, 181

[141] Yepes G., Kates R., Khokhlov A., Klypin A., 1997, MNRAS, 284, 235

[142] Zaritsky D., Kennicutt R.C.Jr., Huchra J.P., 1994, ApJ, 420, 87

[143] Zoccali M., et al., 2003, A&A, 399, 931